Order Number 9121903

A theory of field-aligned current generation from the plasma sheet and the poleward expansion of aurora substorms

Yamauchi, Masatoshi, Ph.D.

University of Alaska Fairbanks, 1990

U·M·I
300 N. Zeeb Rd.
Ann Arbor, MI 48106

A THEORY OF FIELD-ALIGNED CURRENT GENERATION FROM THE PLASMA SHEET AND THE POLEWARD EXPANSION OF AURORA SUBSTORMS

By

Masatoshi Yamauchi

RECOMMENDED:

Chairman, Advisory Committee

Head, Physics Department

APPROVED:

Dean, College of Natural Science

Dean of the Graduate School

5/1/90

Date

A THEORY OF FIELD-ALIGNED CURRENT GENERATION FROM THE PLASMA SHEET AND THE POLEWARD EXPANSION OF AURORA SUBSTORMS

A

THESIS

Presented to the Faculty

of the University of Alaska Fairbanks

in Partial Fulfillment of the Requirements

for the Degree of

DOCTOR OF PHILOSOPHY

By

Masatoshi Yamauchi, M.S.

Fairbanks, Alaska

May 1990

ABSTRACT

This dissertation reports a study of the generation of field-aligned currents in the plasma sheet in terms of magnetosphere-ionosphere coupling. For the study, the plasma sheet and the ionosphere are treated as two-dimensional layers by height integration. In the magnetosphere between them, the Alfvén wave transition time through this region is assumed to be zero. The ionospheric momentum is allowed to be transferred to the plasma sheet. Both linear analyses and numerical simulation are performed to study the field-aligned current generation. In the linear analysis, evolution from initial perturbations is studied. Zero order configurations are steady state without field-aligned currents. The field-aligned currents are treated as a perturbed quantity and linearly related with the other perturbed quantities. One result for the linear waves is that the magnetohydrodynamics (MHD) fast mode and the Alfvén mode are coupled through the ionospheric Hall current. The Hall current causes the dawn-dusk asymmetry: a westward-travelling wave is amplified on the region 1 current system, while an eastward-travelling wave is amplified elsewhere.

The expansion phase of the magnetospheric substorm after the onset is numerically simulated on the near-earth plasma sheet. The inner

edge of the plasma sheet is taken as the outflow boundary. As the initial condition, an enhanced earthward magnetospheric convection is assumed to cause a finite pressure increase at the inner edge of the plasma sheet. The numerical results are as follows. An MHD fast-mode wave is generated. It propagates tailward accompanied by the field-aligned currents. The wave propagation and the field-aligned currents account for the poleward expansion of the aurora and the region 1 field-aligned current during the expansion phase of the substorm. The region 1 field-aligned currents are linked with the dusk to dawn current on this wave, which is driven by the dynamo mechanism of the wave. The ionospheric Hall current causes asymmetry of the wave, and hence, of the field-aligned current distribution. This asymmetry accounts for the stronger field-aligned current in the premidnight sector.

Table of Contents

Abstract 3

Table of Contents 5

List of Figures 8

List of Tables 10

Acknowledgments 11

1. Introduction 13

2. Two Layer Model for M–I Coupling System 20

   2–1. Height-Integrated Equations for the Plasma Sheet 23

   2–2. Ionospheric Loading Effect 41

   2–3. Mapping Between the Ionosphere and the Plasma Sheet 43

   2–4. A Simplified Mapping Model 46

   2–5. Summary of the Basic Equations 50

3. Steady-State Solutions 52

   3–1. Static Equilibrium Without Flow 54

   3–2. Incompressible Parallel Flow 55

   3–3. Compressional 1–D Parallel Flow 58

   3–4. Incompressible Circular Flow 60

4. Linear Analysis of the Field-aligned Current: 1 63

4–1. Steady-State Perturbation from Static Equilibrium 72

4–2. Evolution of Linear Perturbations 75

4–2–1. Relaxation of the Shear Flow 79

4–2–2. Plasma Compression by an Enhanced Flow 84

4–2–3. Field-Aligned Currents by $\nabla P \times \nabla B$ 88

4–3. Enhancement of the Magnetospheric $\mathbf{J} \times \mathbf{B}$ Force 92

4–4. Wave Modes 95

5. Linear Analysis of the Field-aligned Current: 2 103

5–1. Perturbation from 1–D Flow 105

5–2. Perturbation from Parallel Uniform Flow 107

5–3. Inclusion of the Second Dimension 112

5–4. Amplitude Modulation of Waves 117

5–5. Perturbation from a Circular Flow 121

5–5–1. Pure Circular Flow 123

5–5–2. Cyclone-Type Flow 125

6. Numerical Study 127

6–1. Dimensionless Equations 128

6-2. Enhancement of Plasma Sheet Convection 130

6-3. Numerical Results 134

6-3-1. Wave Formation 135

6-3-2. Effect of Convection Velocity 146

6-3-3. Effect of Background Magnetic Field 153

6-3-4. Effect of Adiabatic Compression 163

6-3-5. Effect of Ionospheric Conductivity 166

6-3-6. Effect of Geomagnetic Field Configuration 176

6-4. Region 1 Field-Aligned Current Generation 184

7. Conclusion 186

References Cited 194

List of Figures

Figure 2–1. Two-Layer model for M-I coupling system 21

Figure 2–2. Schematic diagram of the plasma sheet 25

Figure 2–3. Transfer of the $\mathbf{I} \times \mathbf{B}$ force 32

Figure 2–4. Closure of the magnetospheric current 39

Figure 2–5. Mapping relations 48

Figure 3–1. Simple flow patterns without field-aligned currents 57

Figure 4–1. Evolution of a shear flow 80

Figure 4–2. Evolution of a shear flow in ∇B_Z 85

Figure 4–3. A compressible flow 86

Figure 4–4. Effect of $\nabla P \times \nabla B$ 90

Figure 5–1. Electric current in a finite amplitute wave 113

Figure 6–1. Numerical results for basic parameters 137

Figure 6–2. Numerical results when $M_A^2 = 0.4$ instead of 0.2 147

Figure 6–3. Numerical results when $M_A^2 = 0.1$ 150

Figure 6–4. Numerical results when $M_A^2 = 0.4$ and $\beta = 1.6$ 154

Figure 6–5. Numerical results when $M_A^2 = 0.1$ and $\beta = 0.4$ 158

Figure 6–6. Numerical results when $M_S^2 = 0.25$ and $\beta = 1.6$ 161

Figure 6–7. Numerical results when $\gamma = 2.0$ instead of unity 164

Figure 6–8. Numerical results when $\eta = 0.2$ instead of unity 167

Figure 6–9. Numerical results when $\eta = 5.0$ 170

Figure 6–10. Numerical results when $\Sigma_H^* = 0$ 174

Figure 6–11. Numerical results when $\xi_x/\xi_y = 2.0$ instead of unity ... 178

Figure 6–12. Numerical results when $\xi_x/\xi_y = 0.5$ 181

Figure 6–13. Field-aligned current generation from the plasma sheet 185

Figure 7–1. Summary of the numerical results 190

List of Tables

Table 6–1. Parameters of Numerical Models 136

Table 7–1. Numerical Results 189

ACKNOWLEDGMENT

It is my great pleasure to acknowledge some of the people who made this work possible. First, I wish to express my deepest respect and appreciation to Professor S.-I. Akasofu, my thesis advisor, for his academic, spiritual, and financial support. His enthusiasm, inexhaustible patience, and extraordinary physical insight made my studies a meaningful and rewarding experience. I also wish to express my sincere thanks to Professor J. R. Kan for his advice and encouragement. He gave me the direction. His patience and support are gratefully acknowledged.

I am grateful to Professor D. W. Swift and Professor L. C. Lee, for their helpful suggestions and encouragement. Professor D. W. Swift guided me in the formulation of chapter 2 and the numerical code in chapter 6. Professor L. C. Lee also gave me important suggestions concerning the main assumptions in chapters 2 and 4. Sincere thanks are also extended to Professor D. Fritts and Professor W. Harrison, members of my graduate committee, for their helpful suggestions and encouragement.

I must take this opportunity to thank all of the faculty and staff of the Geophysical Institute who discussed my work with me and gave me encouragement. Among them, special thanks are due to my colleagues, Mr. F. Cao, Ms. L. Lyu, Mr. L. Zhu, Dr. M. Mandt, Dr. Y. Shi, Mr. D. Ding, Dr. T. Nakamura, and Mr. D. Hampton for their invaluable help.

This work has been supported in part by the National Science Foundation Grant ATM-03133 and the United State Air Force Contract F19628-86-K-0300 to the University of Alaska Fairbanks through a research assistantship from the Geophysical Institute, University of Alaska. The numerical calculations were made possible by the computer facilities of Academic Computing, University of Alaska Fairbanks.

Chapter 1. Introduction

Large-scale field-aligned currents play an important role in polar auroral phenomena such as substorms. There are two field-aligned currents in the night side polar ionosphere. The region 1 field-aligned current flows into the ionosphere in the morning side and flows out of the ionosphere in the evening side. The region 2 field-aligned current is located equatorward of the region 1 field-aligned current, and its direction is opposite to that of the region 1 field-aligned current. Both the region 1 and the region 2 field-aligned currents have been observed above the ionosphere [*Zmuda and Armstrong*, 1974; *Iijima and Potemra*, 1976; *Sugiura and Potemra*, 1976; *Kamide et al.*, 1986] and in the magnetosphere [*Fairfield*, 1973; *Coleman and McPherron*, 1976; *Frank et al.*, 1981; *Elphic et al.*, 1985; *Nagai*, 1987; *Ohtani et al.*, 1988]. During substorms, the field-aligned currents are enhanced, especially near local midnight, and their distribution is never steady [*Kamide et al.*, 1986]. In fact, the poleward expansion after the substorm onset [*Akasofu*, 1962; 1964; 1974; 1976; 1977] suggests that the region 1 current system moves either poleward or tailward in the magnetosphere. The westward travelling surge [*Akasofu et al.*, 1965; *Akasofu*, 1974, 1977; *Kamide and Akasofu*, 1975; *Opgenoorth et al.*, 1983] also suggests that a large-scale wave is excited where the region 1 current exists. Thus, the field-aligned currents are related to the large-scale dynamics of the substorm.

The generation of the field-aligned current in the magnetosphere is not as well understood as the closure of it in the ionosphere. Theoretical studies of the field-aligned current generation in the magnetosphere have been conducted by a number of authors [*Vasyliunas*, 1972, 1984; *Jaggi and Wolf*, 1973; *Bostrom*, 1975; *Rostoker and Bostrom*, 1976; *Sato and Iijima*, 1979; *Wolf and Spiro*, 1985; *Ogino*, 1986; *Watanabe and Sato*, 1988; *Kan*, 1987; *Walker and Ogino*, 1987]. Most of these models explain the field-aligned current generation in terms of either the pressure gradient force or the inertia force (especially in terms of the vorticity). The particle drift caused by these forces generates the magnetospheric current, and its divergence is linked with the field-aligned current. If the current is associated with the pressure gradient force, the field-aligned current is proportional to $\nabla P \times \nabla B$ where P is the pressure and B is the strength of the magnetic field. If the current is associated with the inertia force in the incompressible flow, the field-aligned current is proportional to the temporal change of the vorticity.

The understanding to date is that the region 2 field-aligned current is generated predominantly by the pressure gradient force in the plasma sheet [*Vasyliunas*, 1970; *Harel et al.*, 1981; *Wolf and Spiro*, 1985]. Generation of the region 1 field-aligned current is still an open issue, though the vorticity is believed to play an important role in either the boundary layer or the plasma sheet [*Sato and Iijima*, 1979; *Hasegawa and Sato*, 1980; *Sonnerup*, 1980; *Ogino*, 1986; *Kan*, 1987]. Many

different types of flow generate the field-aligned current by this "inertia" force. For example, the field-aligned current generations from a circular flow and from a simple shear flow are both explained merely by that "vorticity." We have to specify the types of flows as well as the types of forces in the study of the field-aligned current generation from the magnetosphere. Most of the above models are based on the quasi-steady state approximation; i.e., they consider the instantaneous flow. In this case, for example, the field-aligned current generation from the waves is excluded. However, the dynamics of the flow might play important roles in the field-aligned current generation also, and should be taken into account. Since the field-aligned current is stronger during the substorm, we specifically have to consider the plasma sheet dynamics during that time.

Since the magnetosphere and the ionosphere are coupled through the field-aligned currents, the large-scale plasma sheet dynamics is strongly regulated by the ionosphere. It is necessary to develop a self-consistent quantitative model that includes the current system in the ionosphere and the magnetosphere; say, the magnetosphere-ionosphere (M-I) coupling model [e.g., *Kan and Sun*, 1985; *Watanabe and Sato*, 1988]. We also retain the dynamical features of the field-aligned current. Thus, the model has to explain not only the field-aligned current generation, but also the other large-scale phenomena, during substorms. For example, the poleward expansion and the westward travelling surge can be considered

among those large-scale phenomena, and hence, they have to be explained in terms of this model. Some of the substorm-related phenomena that can be considered small scale may not be explained by this model.

Ideally, we want to simulate both the magnetosphere and the ionosphere at the same time and also include the wave propagation between them. However, the M-I coupling system is too complicated to be treated without assumptions. There have been many simplified large-scale models. *Kan et al.* [1988] focused on the ionospheric dynamics in their substorm model. In this model, the coupling with the magnetosphere is taken into account in terms of the Alfvén wave and its reflection in the magnetosphere. They succeeded in demonstrating the westward travelling surge as well as the enhancement of the field-aligned currents during substorms. By neglecting either the pressure gradient force or the inertia force, some authors were able to treat both the ionosphere and the magnetosphere simultaneously. *Wolf and Spiro* [1985] employed a "convection model" in which they numerically simulated the plasma sheet convection. The convection is calculated as a summation of particle drifts for many species. They neglected the inertia force of the magnetospheric plasma; i.e., the plasma is essentially massless. As the boundary condition, the region 1 field-aligned current is previously given in this model. *Watanabe and Sato* [1988] numerically simulated the evolution of the field-aligned current caused by the incompressible magnetospheric convection.

They showed the development of the multiple auroral arcs that are dominant in the premidnight side. The pressure gradient is neglected because of the incompressibility assumption. However, the boundary condition is such that they do not consider the situation during substorms. This approach is opposite to that of *Wolf and Spiro.*

Another approach is to focus on the magnetospheric dynamics. The ionospheric effect is taken into account in terms of mapping, or simply as the boundary conditions. Magnetospheric dynamics itself has been studied by many authors, even though the ionosphere is included simply as the boundary conditions [e.g. *Birn and Schindler*, 1983]. On the other hand, *Lotko et al.* [1987] mapped the ionospheric quantities to the magnetospheric boundary layer in the steady state. They also assumed an incompressible plasma in the magnetosphere. In the work presented here, we take the last approach and also include the full dynamics of the magnetosphere; i.e., the inertia force, the pressure gradient force, and the $\mathbf{J} \times \mathbf{B}$ force.

Let us consider the interconnection between the ionosphere and the magnetosphere. The magnetic field lines are not perfect conductors as idealized in magnetohydrodynamics (MHD), that is, the interconnection is not simple. We assume zero transition time for the Alfvén wave to travel through the geomagnetic field lines. Since the field-aligned currents and the other electromagnetic quantities are

carried by waves, there is a time lag between the ionospheric phenomena and the magnetospheric phenomena. This time lag is characterized by the Alfvén wave transition time, which is considered to be a few minutes in the other M–I coupling models by *Miura and Sato* [1980] and *Kan and Kamide* [1985]. *Miura and Sato* showed that the finite transition time causes thinning of the aurora arcs through the coupling with the ionospheric density wave [*Sato*, 1978]. *Kan and Kamide* [1985] showed this effect also causes Pi 2 pulsation [*Rostoker*, 1967; *Southwood and Stuart*, 1980] during substorms. The parallel electric field causes the field-aligned potential drop between the ionosphere and the magnetosphere. It is included in the models by *Lotko et al.* [1987] and *Harel et al.* [1981]. According to the analytical study by *Lotko et al.*, this effect brings dispersion into the M–I coupling equations in their boundary layer model. The upward current limit proposed by *Knight* [1973] and *Fridman and Lemaire* [1980] is employed by *Kan and Sun* [1985] and *Watanabe et al.* [1986]. In the present work, for simplicity, none of these three effects is considered. Instead, the present model includes both the plasma inertia and the pressure in the magnetosphere. Thus, we may study the full dynamics of the plasma sheet. The mapping relation between the ionosphere and the magnetosphere is still an open issue. For example, we do not even know where the region 1 field-aligned current originates in the magnetosphere; suggestions include the magnetopause boundary layer [e.g., *Sonnerup*, 1980], the plasma sheet boundary

layer [e.g., *Frank*, 1985], or the central plasma sheet [e.g., *Sato and Iijima*, 1979]. In the present self-consistent model, the night side region 1 field-aligned currents map to the height integrated plasma sheet which contains both the central plasma sheet and the plasma sheet boundary layer. Thus, the dynamics of the height integrated plasma sheet should explain not only the generation of the region 1 field-aligned current, but also the poleward expansion in the near-earth plasma sheet.

There are many models that describe the dynamics of the magnetosphere during the substorm. The plasmoid model [*Hones et al.*, 1974], the boundary layer model [e.g., *Rostoker and Eastman*, 1987], and the convection model [*Harel et al.*, 1981] are of most interest. All of these models have an enhanced earthward convection. We assume this enhanced convection at the substorm onset, which is the same initial condition as used in the M–I coupling model by *Kan et al.* [1988]. We formulate the basic equations in chapter 2. Under further simplified assumptions, we perform analytical studies for some basic flow patterns in chapters 3 to 5. The linear perturbation method is applied to static equilibrium in chapter 4, and to the steady state flows in chapter 5. In chapter 6, we specifically study the situation right after the substorm onset by a numerical simulation.

Chapter 2. Two Layer Model for M-I Coupling System

In this chapter, we formulate the magnetosphere-ionosphere (M-I) coupling system to obtain macroscopic basic equations viewed from the plasma sheet side. Figure 2–1 shows the three regions composing the M-I coupling system. They have different scale lengths along the magnetic field: the thickness of the ionosphere is several 100 km, the thickness of the plasma sheet is a few Re (earth radii), and the distance between the ionosphere and the plasma sheet is 10 to 15 Re along the geomagnetic field. Since field-aligned scale lengths are much smaller in the plasma sheet and in the ionosphere compared to those in the magnetosphere between them, we simplify this situation into two layers plus an interface region. The two layer interface model involves a height-integrated ionosphere, a height-integrated plasma sheet, and the magnetosphere between them which merely connects the two height-integrated layers through the magnetic field lines. There are some cautions we have to consider before the two-layer interface model is formulated.

In many studies of the M-I coupling, the ionospheric quantities are height integrated [e.g., *Kan et al.*, 1988; *Harel et al.*, 1981; *Jaggi and Wolf*, 1973; *Hasegawa and Sato*, 1980]. The formulation for the height integration can be found, for example, in *Brekke et al.* [1974]. The height integration of the plasma sheet is not as simple as that for the ionosphere because we have to include the magnetic tension

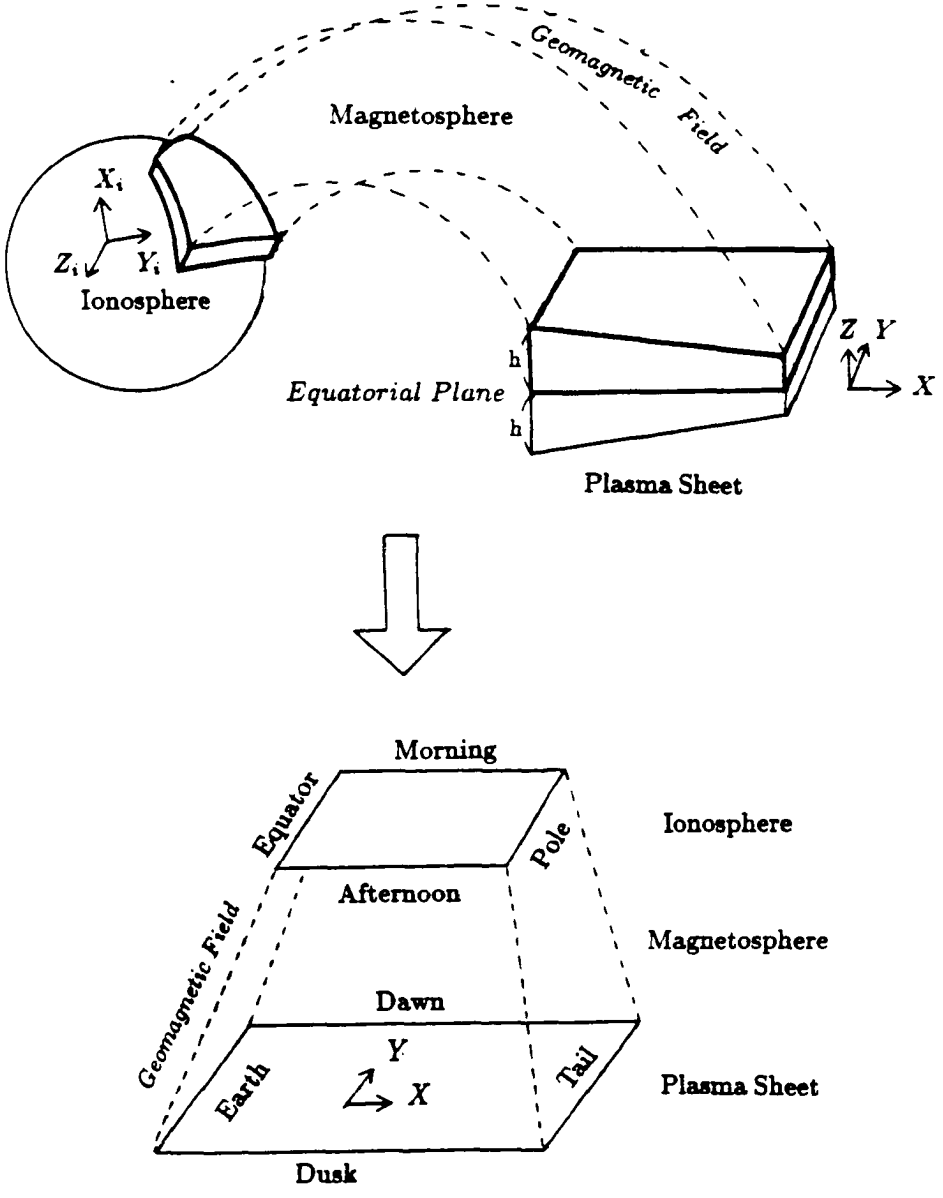

Figure 2–1. Two-layer model for the M-I coupling system. The magnetosphere and the ionosphere are treated as 2–D layers after height integration. The geometry that connects these layers is also simplified.

force caused by the bending of the geomagnetic field. We have another problem in selecting the basic equations. In the M-I coupling, the ionospheric Ohm's law provides a relation between the electric current and the convection electric field. Therefore, if we employ the normal MHD Ohm's law in the magnetosphere, that over-determines the current density. If we do not employ the normal MHD Ohm's law, we may not employ the x, y components of the induction equation, and hence, the z component of convection (u_z). Since u_z is not determined in the height-integrated equations, this omission is rational as long as we can assume $u_z \ll u_{x,y}$ as is observed [*Parks et al.*, 1984] where $\mathbf{u}_{x,y}$ is the convection parallel to the equatorial plane. Note that this dilemma of over-determination arises because we use a height-integrated equation for the plasma sheet.

We treat the magnetosphere in between as the inertia-free interface. That means we assume zero density there, and hence, zero transition time through this layer. In fact, the density of this layer is much less than that in the plasma sheet [*Parks et al.*, 1979]. In this sense, this region exists just to connect the plasma sheet and the ionosphere instantaneously. However, this region still acts as an active region when plasma sheet thinning or poleward expansion is concerned. Even though the plasma density in this region is much lower than that in the plasma sheet so that we may neglect its plasma motion in the x, y plane, it still works as the source or sink of plasma because the area across which the thinning plasma flows is very large. In this way, we may not neglect its finite density effect if and only if we

consider the mass transfer across the top boundary of the plasma sheet. Therefore, we leave the plasma density unknown (but very small) and this effect is treated by specifying the mass transfer across the top boundary of the plasma sheet as a given parameter. In all other places, the plasma density outside of the plasma sheet is neglected.

The same approximation can be applied to the plasma pressure. However, since it is multiplied by temperature which is lower in the lobe than in the plasma sheet, we sometimes assume the pressure transfer equal to zero while there is finite mass transfer.

2–1. Height-Integrated Equations for the Plasma Sheet

Let us start with the plasma sheet. In order to height-integrate the plasma sheet where the magnetic field is not straight, we assume:

(a) $\rho(z=h) \ll \rho(z=0)$

(b) $P(z=h) \ll P(z=0)$

(c) $|\frac{\partial \mathbf{u}_{x,y}}{\partial z}| \ll |\frac{\langle \mathbf{u}_{x,y} \rangle}{h}|$

(d) $u_z \ll \langle u_{x,y} \rangle$

(e) $|\frac{\partial B_z}{\partial z}| \ll |\frac{\langle B_z \rangle}{h}|$

(f) $\mathbf{B}_{x,y}(z) = -\mathbf{B}_{x,y}(-z)$

(g) $$\langle J_z \mathbf{B}_{x,y} \rangle = \zeta J_z(z=h)\mathbf{B}_{x,y}(z=h)$$

(h) $$\frac{|\nabla_{x,y} B_z|}{B_z/h} \ll \frac{J_{x,y}}{J_z}$$

where h is that height of the plasma sheet outside which the plasma density is negligibly small, L is the characteristic length in the (x, y) direction, the quantities with the bracket are the height averaged values, e.g., $\langle u_{x,y} \rangle = \int u_{x,y} dz/h$, etc., and a factor $\zeta < 1$ is assumed to be constant. These assumptions come from the plasma sheet property observed by satellite [e.g., *Parks et al.*, 1979; *Huang*, 1987]

Figure 2–2 illustrates some of the plasma sheet properties. The density and the pressure are much higher in the plasma sheet than outside of it, and that guarantees the rationale of assumptions (a) and (b). Since the geometry and quantities are essentially symmetric with respect to the equatorial plane, we may have the assumption (f). The north-south component of the convection is much slower than the earthward convection on the plasma sheet, which provides the assumption (d).

The rest of the assumptions comes from the fact that the geomagnetic field is essentially the dipole field. The assumption (e) merely states that B_z is nearly constant in the z direction. This is true for the dipole field if we consider it near the equatorial plane. Since $J_z \propto B_z$, the assumption (g) is rather general if we take $B_z(z)$ as a simple function of z. This is also true for the dipole field. The assumption (h) is not intuitive. Unless $J_{x,y}$ is much larger than J_z (that is the

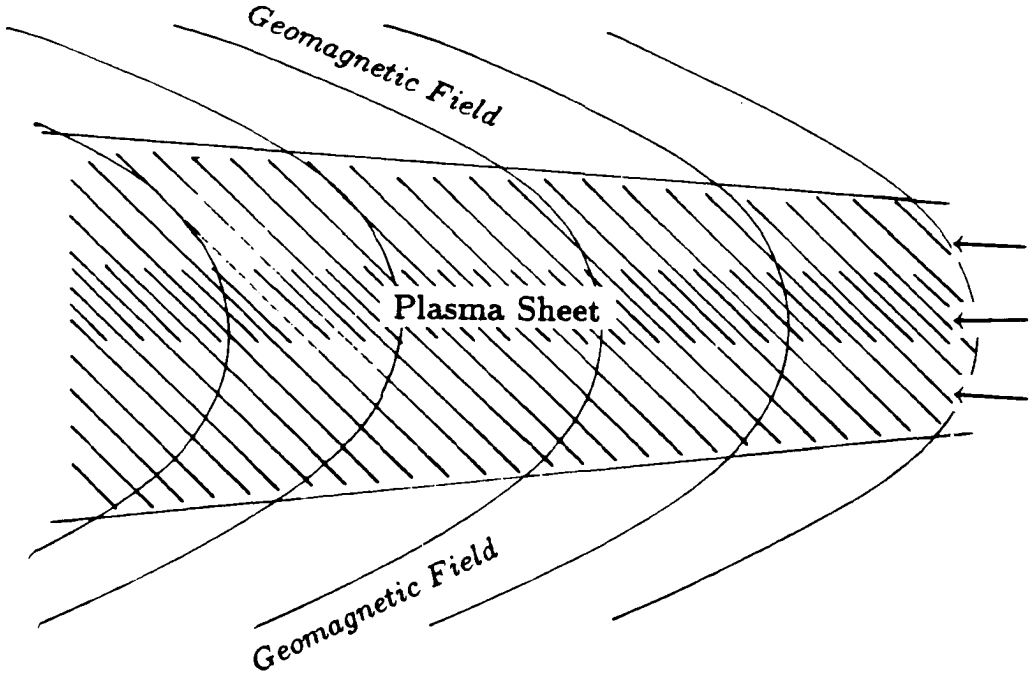

Figure 2–2. Schematic diagram of the plasma sheet. The configuration is symmetric with respect to the equatorial plane (center of the figure). The pressure and the density are much greater near the equatorial plane than at the boundaries. The convection is assumed to be two dimensional as indicated by the arrows.

cause of the change of B_z in the (x, y) plane), we can assume that B_z is nearly uniform. Since the geomagnetic field without any $J_{x,y}$ is dipole, this assumption is also reasonable.

The assumption (c) could be invalid when the flow speed in the plasma sheet boundary layer is much faster than that in the central plasma sheet. The positive velocity shear in the z direction might be an important cause for the field-aligned current generation. According to observation [*Parks et al.*, 1984], the assumption (c) is not a bad one even though there is a velocity shear in the z direction. We do not study the effect of this velocity shear, and hence we exclude it from the present model as shown in Figure 2–2.

Since the external force is the ultimate source of the plasma convection and the field-aligned current, we first consider the force balance equation in the plasma sheet; i.e., the momentum equation. The x, y components are

$$\rho\frac{\partial}{\partial t}\mathbf{u}_{x,y} + \rho(\mathbf{u}\cdot\nabla)\mathbf{u}_{x,y} + \nabla_{x,y}P = \mathbf{J}_{x,y}\times\mathbf{B}_z + \mathbf{J}_z\times\mathbf{B}_{x,y} \qquad (2\cdot 1)$$

With the help of the continuity equation:

$$\frac{\partial}{\partial t}\rho + \nabla\cdot(\rho\mathbf{u}) = 0 \qquad (2\cdot 2)$$

the above equation can be rewritten as

$$\frac{\partial}{\partial t}(\rho\mathbf{u}_{x,y}) + \sum_{i}^{x,y,z}\frac{\partial}{\partial x_i}(\rho u_i\mathbf{u}_{x,y}) + \nabla_{x,y}P = \mathbf{J}_{x,y}\times\mathbf{B}_z + \mathbf{J}_z\times\mathbf{B}_{x,y}$$

Let us height-integrate this equation in the z direction. Taking into consideration the north-south symmetry, the integral has to be only for half of the plasma sheet,

i.e., from the equatorial plane ($(z=0)$) to the top of the plasma sheet ($(z=h)$). In general, h depends on x, y and t. In other words, the height-integrated equation still keeps all 3-D effects.

$$\int_0^{h(x,y,t)} \frac{\partial}{\partial t}(\rho \mathbf{u}_{x,y})dz + \sum_i^{x,y} \int_0^{h(x,y,t)} \frac{\partial}{\partial x_i}(\rho u_i \mathbf{u}_{x,y})dz + \int_0^{h(x,y,t)} \frac{\partial}{\partial z}(\rho u_z \mathbf{u}_{x,y})dz + \int_0^{h(x,y,t)} \nabla_{x,y} P dz = \int_0^{h(x,y,t)} \mathbf{J}_{x,y} \times \mathbf{B}_z dz + \int_0^{h(x,y,t)} \mathbf{J}_z \times \mathbf{B}_{x,y} dz$$

Since

$$\begin{aligned}
&\frac{\partial}{\partial t} \int_0^{h(x,y,t)} \rho \mathbf{u}_{x,y} dz \\
&= \lim_{\delta t \to 0} \frac{1}{\delta t} [\int_0^{h(x,y,t+\delta t)} \rho(t+\delta t)\mathbf{u}_{x,y}(t+\delta t)dz - \int_0^{h(x,y,t)} \rho(t)\mathbf{u}_{x,y}(t)dz] \\
&= \lim_{\delta t \to 0} \frac{1}{\delta t} \int_{h(x,y,t)}^{h(x,y,t+\delta t)} \rho(t+\delta t)\mathbf{u}_{x,y}(t+\delta t)dz \\
&\quad + \lim_{\delta t \to 0} \frac{1}{\delta t} \int_0^{h(x,y,t)} [\rho(t+\delta t)\mathbf{u}_{x,y}(t+\delta t) - \rho(t)\mathbf{u}_{x,y}(t)]dz \\
&= \lim_{\delta t \to 0} \frac{1}{\delta t} [h(x,y,t+\delta t) - h(x,y,t)]\rho(t)\mathbf{u}_{x,y}(t) \\
&\quad + \int_0^{h(x,y,t)} \lim_{\delta t \to 0} \frac{1}{\delta t} [\rho(t+\delta t)\mathbf{u}_{x,y}(t+\delta t) - \rho(t)\mathbf{u}_{x,y}(t)]dz \\
&= \frac{\partial h}{\partial t} \rho \mathbf{u}_{x,y} + \int_0^{h(x,y,t)} \frac{\partial}{\partial t}(\rho \mathbf{u}_{x,y})dz
\end{aligned}$$

and similarly

$$\sum_i^{x,y} \frac{\partial}{\partial x_i} \int_0^{h(x,y,t)} \rho u_i \mathbf{u}_{x,y} dz = \sum_i^{x,y} \frac{\partial h}{\partial x_i} \rho u_i \mathbf{u}_{x,y} + \int_0^{h(x,y,t)} \sum_i^{x,y} \frac{\partial}{\partial x_i}(\rho u_i \mathbf{u}_{x,y})dz$$

etc., the height-integrated momentum equation can be rewritten as

$$\frac{\partial}{\partial t}\int \rho \mathbf{u}_{x,y}dz + \sum_{i}^{x,y}\frac{\partial}{\partial x_i}\int \rho u_i \mathbf{u}_{x,y}dz - [\rho \mathbf{u}_{x,y}(\frac{\partial}{\partial t}h + \mathbf{u}_{x,y}\cdot\nabla_{x,y}h - u_z)]_{z=h}$$
$$+ \nabla_{x,y}\int Pdz - P(z=h)\nabla_{x,y}h$$
$$= \int \mathbf{J}_{x,y}\times\mathbf{B}_z dz + \int \mathbf{J}_z \times \mathbf{B}_{x,y}dz$$

Now, we have to employ assumptions (a) – (h) in order to perform the integration. For example, a factor ζ appears through the integration of the last two terms because of assumption (g). We obtain

$$\mathbf{V}_{x,y}[\frac{\partial}{\partial t}m + \nabla_{x,y}(m\mathbf{V}_{x,y})] + m\frac{\partial}{\partial t}\mathbf{V}_{x,y} + m(\mathbf{V}_{x,y}\cdot\nabla_{x,y})\mathbf{V}_{x,y} + \nabla_{x,y}\pi$$
$$= [T_z\rho\mathbf{u}_{x,y} + P\nabla_{x,y}h + h\zeta\mathbf{J}_z\times\mathbf{B}_{x,y}]_{z=h} + \mathbf{I}_{x,y}\times\mathbf{B}_z$$

where $m = \int \rho dz$, $\pi = \int Pdz$, $\mathbf{V}_{x,y} = \int \rho\mathbf{u}_{x,y}dz/\int \rho dz \sim \mathbf{u}_{x,y}$, $\mathbf{I}_{x,y} = \int \mathbf{J}_{x,y}dz$, and

$$T_z \equiv [\frac{\partial}{\partial t}h + \mathbf{u}_{x,y}\cdot\nabla_{x,y}h - u_z]_{z=h} \qquad (2\cdot 3)$$

is the unit mass transfer across the $z=h$ boundary; e.g., $\partial h/\partial t > 0$ or $u_z < 0$ corresponds to the mass transfer from the tail lobe to the plasma sheet, and vice versa. Though T_z is multiplied by $\rho(z=h)$, which is negligibly small (we assume no inertia outside the plasma sheet), this term still remains because the area of that boundary is large enough, as is previously discussed. One can consider this is just an external source term of the kinetic energy.

The first term of the left-hand side has an integral form of the continuity equation:

$$\int_0^{h(x,y,t)} \frac{\partial \rho}{\partial t} dz + \int_0^{h(x,y,t)} \nabla \cdot (\rho \mathbf{u}) dz = 0$$

or

$$\frac{\partial}{\partial t} m + \nabla_{x,y}(m \mathbf{V}_{x,y}) = T_z \rho(z=h) \qquad (2 \cdot 4)$$

where the unit mass transfer across the $z=h$ boundary (T_z) again appears on the right-hand side. With the help of this relation, the first term of the momentum equation can be rewritten as $\rho_{z=h} \mathbf{V}_{x,y} T_z$ and that cancels with the first term of the right-hand side. The second term of the right-hand side of the momentum equation is the pressure transfer term across the $z = h$ boundary. This term is not important unless $h(x, y, t)$ varies severely and $P(h)$ is not much smaller than $P(0)$. Therefore, we neglect this term hereafter. The momentum equation becomes

$$m \frac{\partial}{\partial t} \mathbf{V}_{x,y} + m(\mathbf{V}_{x,y} \cdot \nabla_{x,y}) \mathbf{V}_{x,y} + \nabla_{x,y} \pi = h \zeta \mathbf{J}_z \times \mathbf{B}_{x,y}(z=h) + \mathbf{I}_{x,y} \times \mathbf{B}_z \, (2 \cdot 5)$$

Let us consider $\mathbf{I}_{x,y}$ and $\mathbf{B}_{x,y}$ terms; they are related to each other through Ampere's law:

$$\begin{aligned} \mathbf{I}_{x,y} &= \int_0^{h(x,y,t)} \mathbf{J}_{x,y} dz \\ &= \frac{1}{\mu_0} \hat{z} \times \int_0^{h(x,y,t)} (\frac{\partial}{\partial z} \mathbf{B}_{x,y} - \nabla_{x,y} B_z) dz \\ &= \frac{1}{\mu_0} \hat{z} \times [\mathbf{B}_{x,y}(z=h) - h \nabla_{x,y} B_z] \end{aligned} \qquad (2 \cdot 6)$$

With this relation, we have

$$m\frac{\partial}{\partial t}\mathbf{V}_{x,y} + m(\mathbf{V}_{x,y}\cdot\nabla_{x,y})\mathbf{V}_{x,y} + \nabla_{x,y}\pi$$
$$= \mathbf{I}_{x,y}\times\mathbf{B}_z + h\zeta J_z(\mu_0\mathbf{I}_{x,y} + h\hat{z}\times\nabla_{x,y}B_z)$$
$$\sim \mathbf{I}_{x,y}\times\mathbf{B}_z + h\zeta\mu_0 J_z\mathbf{I}_{x,y} \qquad (2\cdot 5')$$

where we used the assumption (h) for the last part. The second term on the right-hand side is still smaller than the first term according to assumption (h).

Since we may not neglect a drag force on the $z=h$ boundary caused by the ionospheric current, which has to be included in the $\mathbf{I}_{x,y}\times\mathbf{B}_z$ term, we examine it from the ionospheric view point. For simplicity, let us consider uniform parallel flow in the x direction as shown in Figure 2–3. The flow's energy is dissipated because of the ionosphere (ionospheric $i-n$ collision) which is expressed in terms of the viscous force. The total drag force at the ionosphere is given as

$$-\mathbf{F}_v(i)dx_idy_i = -\mathbf{I}_i\times\mathbf{B}_idx_idy_i$$
$$= -\mathbf{I}_i\times\mathbf{B}_idxdy\frac{B_z(z=h)}{B_i}$$
$$= \frac{I_i}{I_{x,y}}\mathbf{I}_{x,y}\times\mathbf{B}_zdxdy$$

where dx_idy_i is the area element in the ionosphere which corresponds to the area element $dxdy$ in the plasma sheet through the magnetic flux tube, $\mathbf{I}_i$ is the ionospheric height-integrated current, and $\mathbf{B}_i$ is the ionospheric magnetic field. If this force were conserved along the magnetic flux, the drag force should be stronger

than the $\mathbf{I}_{x,y} \times \mathbf{B}$ force by a factor of the geometric difference ($\sim \sqrt{B_i/B}$). However, we have to take the energy, not the force, as the conserved quantity on the same magnetic flux tube when we consider the effective drag force by the ionosphere. Equating the work in the plasma sheet and Joule heating in the ionosphere,

$$\begin{aligned} -\mathbf{F}_v \cdot \mathbf{V}_{x,y} dx dy &= (\mathbf{I}_i dx_i) \cdot \mathbf{E}_i dy_i \\ &= (\mathbf{I}_{x,y} dx) \cdot \mathbf{E}_{x,y} dy \\ &= (\mathbf{I}_{x,y} \times \mathbf{B}_z) \cdot \mathbf{V}_{x,y} dx dy \end{aligned}$$

or

$$-\mathbf{F}_v = \mathbf{I}_{x,y} \times \mathbf{B}_z \qquad (2 \cdot 7)$$

This is consistent with the height-integrated momentum equation (2·6). The minus sign for $\mathbf{F}_v$ is comes from the fact that the ionospheric neutrals receive this force from the M–I coupling current system. As is obvious from the expression of (2·7), the idea of the ionospheric 'drag' force allows to have the counter part of the ionospheric current in the magnetosphere [*Akasofu et al.*, 1981]. This assumption is exactly right for the Pedersen current if we consider the energy budget.

In terms of the height-integrated equation, we may extract the magnetic tension force as well as the magnetic pressure force from the $J \times B$ force. These forces are not included in the normal 2-D equation or even in the height-integrated ionospheric 2–D equation. The main contribution of the magnetic tension force comes from $B_z \mathbf{B}_{x,y} \propto \mathbf{I}_{x,y} \times \mathbf{B}_z$.

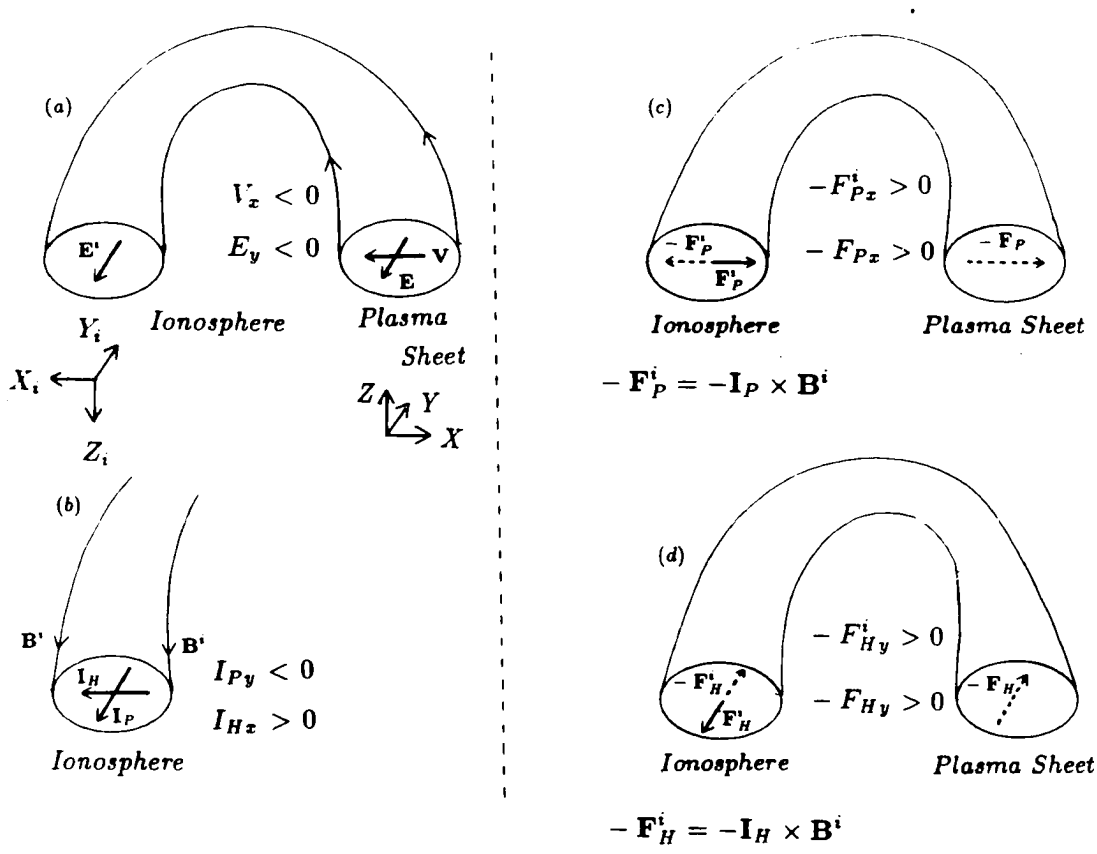

Figure 2–3. Transfer of the $\mathbf{I} \times \mathbf{B}$ force. magnetospheric convection causes the ionospheric electric field ($\mathbf{E}^i$) and currents ($\mathbf{I}_P$ and $\mathbf{I}_H$). The $\mathbf{I} \times \mathbf{B}$ force ($= \mathbf{F}^i$) acts on the ionospheric neutrals, and its reaction forces ($-\mathbf{F}^i_P$ and $-\mathbf{F}^i_H$) are transmitted to the magnetosphere.

We have to examine the z component momentum equation which still is effective after we assumed $u_z \ll u_{x,y}$:

$$\begin{aligned}\frac{\partial}{\partial t}(\rho u_z) + \nabla_{x,y}(\rho u_z \mathbf{u}_{x,y}) + \frac{\partial}{\partial z}P + \frac{\partial}{\partial z}(\rho u_z^2) \\ = (\mathbf{J}_{x,y} \times \mathbf{B}_{x,y})_z \\ = -\frac{1}{\mu_0}[\frac{\partial}{\partial z}\mathbf{B}_{x,y} - \nabla_{x,y}B_z] \cdot \mathbf{B}_{x,y} \qquad (2 \cdot 8)\end{aligned}$$

or integrating over z,

$$\begin{aligned}\frac{\partial}{\partial t}\int \rho u_z dz + \nabla_{x,y}\int \rho u_z \mathbf{u}_{x,y} dz - T_z \rho u_z(z=h) + [P + \frac{B_{x,y}^2}{2\mu_0}]_0^h \\ = \frac{1}{\mu_0}\int \nabla_{x,y}B_z \cdot \mathbf{B}_{x,y} dz\end{aligned}$$

With the help of assumptions (d), (e), and (g), this equation is reduced to

$$-P(z=0) + \frac{B_{x,y}^2(z=h)}{2\mu_0} = \frac{2\zeta}{1+\zeta}\frac{h}{\mu_0}\nabla_{x,y}B_z \cdot \mathbf{B}_{x,y}(z=h)$$

This equation is a condition for h, but not included in the governing equation in the present algorithm because this constraint is not very restrictive. In the plasma sheet where the plasma is confined in a thin (small h compared to the extent in the x, y direction) layer, the above relation is further reduced to:

$$\frac{\pi}{B_{x,y}^2(z=h)/2\mu_0} = O(h) \qquad (2 \cdot 9)$$

The z component velocity (u_z) can be calculated after h is determined provided that unit mass transfer across z=h boundary is given. In this sense, u_z is rather an assumed quantity.

As we already have the equations for the conservation of the mass and the momentum, we need an equation for the energy conservation. The MHD energy equation is given as:

$$\frac{\partial}{\partial t}[\rho(\frac{u^2}{2}+U_I)]+\nabla_{x,y}[\rho\mathbf{u}_{x,y}(\frac{u^2}{2}+U_I+\frac{P}{\rho})]+\frac{\partial}{\partial z}[\rho u_z(\frac{u^2}{2}+U_I+\frac{P}{\rho})]$$
$$=\mathbf{J}_{x,y}\cdot\mathbf{E}_{x,y}+J_zE_z-\nabla\cdot\mathbf{q} \qquad (2\cdot 10)$$

where U_I is the internal energy and $\mathbf{q}$ is the heat flow [e.g., *Nicholson*, 1983]. Note that both $\mathbf{J}_{x,y}$ and J_z are determined as the consequence of the ionospheric conductivity which is formulated later. The height integration over z can be performed in the same manner as shown above:

$$\frac{\partial}{\partial t}\int\rho(\frac{u^2}{2}+U_I)dz+\nabla_{x,y}\int\rho\mathbf{u}_{x,y}(\frac{u^2}{2}+U_I)dz+\nabla_{x,y}\int P\mathbf{u}_{x,y}dz$$
$$-[T_z\rho(\frac{u^2}{2}+U_I)]_{z=h}-[P(\mathbf{u}_{x,y}\cdot\nabla_{x,y}h-u_z)]_{z=h}$$
$$=\int\mathbf{J}_{x,y}\cdot\mathbf{E}_{x,y}dz+\int E_zJ_zdz-\nabla_{x,y}\int\mathbf{q}_{x,y}dz-[(\mathbf{q}_{x,y}\cdot\nabla_{x,y}h-q_z)]_{z=h}$$

Under the assumptions (a) – (h) we have

$$\frac{\partial}{\partial t}(\frac{mV_{x,y}^2}{2})+\nabla_{x,y}(\mathbf{V}_{x,y}\frac{mV_{x,y}^2}{2})+\nabla_{x,y}(\mathbf{V}_{x,y}\pi)$$
$$+\frac{\partial}{\partial t}\int\rho U_Idz+\nabla_{x,y}(\mathbf{V}_{x,y}\int\rho U_Idz)$$
$$=[T_z\rho(\frac{V_{x,y}^2}{2}+U_I)]_{z=h}+[P(\mathbf{V}_{x,y}\cdot\nabla_{x,y}h-u_z)]_{z=h}-\mathbf{I}_{x,y}\cdot(\mathbf{V}_{x,y}\times\mathbf{B}_z)$$
$$-\int\mathbf{J}_{x,y}\cdot(\mathbf{u}_z\times\mathbf{B}_{x,y})dz+\int E_zJ_zdz-\nabla_{x,y}\mathbf{Q}_{x,y}-Q_z$$

where $\mathbf{Q}_{x,y}=\int\mathbf{q}_{x,y}dz$ is the height-integrated heat flow, $Q_z=[\mathbf{q}_{x,y}\cdot\nabla_{x,y}h-q_z]_{z=h}$ is the heat flow across the z=h boundary, and we used $\mathbf{E}=-\mathbf{U}\times\mathbf{B}$.

Let us subtract the kinetic energy from this equation. By multiplying $\mathbf{V}_{x,y}$ to the momentum equation (2·5), we have the equation for the kinetic energy

$$\begin{aligned}
&\frac{\partial}{\partial t}(\frac{mV_{x,y}^2}{2}) + \nabla_{x,y}(\mathbf{V}_{x,y}\frac{mV_{x,y}^2}{2}) + \mathbf{V}_{x,y}\cdot\nabla_{x,y}\pi \\
= \;& [T_z\rho V_{x,y}^2 + P\mathbf{V}_{x,y}\cdot\nabla_{x,y}h - h\zeta\mathbf{J}_z\cdot(\mathbf{V}_{x,y}\times\mathbf{B}_{x,y})]_{z=h} - \mathbf{F}_v\cdot\mathbf{V}_{x,y}
\end{aligned}$$

where we again used equation (2·4). Subtracting the above equation from the height-integrated energy equation, we obtain the equation for the non-kinetic energy conservation. Under the assumptions (a) - (h), it is

$$\begin{aligned}
&\pi\nabla_{x,y}\cdot\mathbf{V}_{x,y} + \frac{\partial}{\partial t}\int\rho U_I dz + \nabla_{x,y}(\mathbf{V}_{x,y}\int\rho U_I dz) \\
= \;& [T_z\rho(-\frac{V_{x,y}^2}{2} + U_I) - Pu_z]_{z=h} - \nabla_{x,y}\mathbf{Q}_{x,y} - Q_z \\
& - \mathbf{F}_v\cdot\mathbf{V}_{x,y} - \mathbf{V}_{x,y}\cdot(\mathbf{I}_{x,y}\times\mathbf{B}_z) + h\zeta[\mathbf{J}_z\cdot(\mathbf{V}_{x,y}\times\mathbf{B}_{x,y})]_{z=h} \\
& + \int(\mathbf{J}_{x,y}\times\mathbf{B}_{x,y})_z u_z dz - \int\mathbf{J}_z\cdot(\mathbf{u}_{x,y}\times\mathbf{B}_{x,y})dz \\
= \;& [T_z\rho(-\frac{V_{x,y}^2}{2} + U_I) - Pu_z]_{z=h} - \nabla_{x,y}\mathbf{Q}_{x,y} - Q_z \\
& + \int[\rho(\frac{\partial}{\partial t} + \mathbf{u}\cdot\nabla)\frac{u_z^2}{2} + u_z\frac{\partial}{\partial z}P]dz \\
= \;& [T_z\rho(-\frac{V_{x,y}^2 + u_z^2}{2} + U_I)]_{z=h} - \nabla_{x,y}\mathbf{Q}_{x,y} - Q_z \\
& + \frac{\partial}{\partial t}\int\frac{\rho u_z^2}{2}dz + \nabla_{x,y}\int\frac{\rho u_z^2}{2}\mathbf{u}_{x,y}dz - \int P\frac{\partial}{\partial z}u_z dz
\end{aligned}$$

Since $U_I = (f/2)P/\rho \gg u_z^2$ where f is the degree of the freedom of a particle, this equation becomes

$$\pi\nabla_{x,y}\cdot\mathbf{V}_{x,y} + \frac{f}{2}\frac{\partial}{\partial t}\int Pdz + \frac{f}{2}\nabla_{x,y}(\mathbf{V}_{x,y}\int Pdz) + \nabla_{x,y}\mathbf{Q}_{x,y} + Q_z$$

$$= [T_z\rho(-\frac{u^2}{2}+\frac{f}{2}\frac{P}{\rho})]_{z=h} - \pi(\frac{\partial u_z}{\partial z})_{z=h}$$

or we have an equation for the height-integrated pressure (π):

$$\begin{aligned}
&\frac{f}{2}\frac{\partial}{\partial t}\pi + \frac{f}{2}\mathbf{V}_{x,y}\cdot\nabla_{x,y}\pi + \frac{f+2}{2}\pi\nabla_{x,y}\cdot\mathbf{V}_{x,y} - \frac{f}{2}T_zP(z=h) \\
= \;& -T_z(\frac{\rho u^2}{2})_{z=h} - \pi(\frac{\partial u_z}{\partial z})_{z=h} - \nabla_{x,y}\cdot\mathbf{Q}_{x,y} - Q_z \\
= \;& -\nabla_{x,y}\cdot\mathbf{Q}_{x,y} - Q_z \qquad (2\cdot 11)
\end{aligned}$$

For the adiabatic case, we may neglect the right-hand side.

Instead of the above procedure for the energy equation, we may start with the equation of state. Let us suppose the system obeys a polytropic relation; i.e.,

$$\begin{aligned}
\frac{d}{dt}(P\rho^{-\gamma}) &= P\rho^{-\gamma}(\frac{1}{P}\frac{dP}{dt} - \frac{\gamma}{\rho}\frac{d\rho}{dt}) \\
&= 0
\end{aligned}$$

where the adiabatic assumption and isothermal assumption correspond to $\gamma=\infty$ and $\gamma=1$, respectively. With the help of the continuity equation, this equation becomes

$$\begin{aligned}
\frac{dP}{dt} + \gamma P\nabla\cdot\mathbf{u} &= \frac{\partial}{\partial t}P + \nabla_{x,y}\cdot(P\mathbf{u}_{x,y}) + (\gamma-1)P\nabla_{x,y}\cdot\mathbf{u}_{x,y} \\
&= 0
\end{aligned}$$

After integration over z under the assumptions (b), (c) and (d), we obtain

$$\begin{aligned}
\frac{\partial}{\partial t}\pi + \nabla_{x,y}\cdot(\pi\mathbf{V}_{x,y}) &= T_zP(z=h) - (\gamma-1)(\pi\nabla_{x,y}\cdot\mathbf{V}_{x,y} + \int P\frac{\partial}{\partial z}u_z dz) \\
&= T_zP(z=h) - (\gamma-1)\pi\nabla_{x,y}\cdot\mathbf{V}_{x,y} \qquad (2\cdot 11')
\end{aligned}$$

This is identical to the height-integrated energy equation (2·11), if we take $\gamma = (f+2)/f$ and we neglect the right-hand side of (2·11).

Next, we obtain the equations for B_z, $\mathbf{B}_{x,y}$, $\mathbf{I}_{x,y}$, and J_z. The plasma sheet current can be divided into two:

$$\mathbf{I}_{x,y} = \mathbf{I}^m_{x,y} + \mathbf{I}^i_{x,y} \tag{2 · 12}$$

where $\mathbf{I}^i_{x,y}$ is the part which gives the ionospheric current into the magnetospheric equations through the $\mathbf{J} \times \mathbf{B}$ drag force, and $\mathbf{I}^m_{x,y}$ is the rest of it. The first part (we call it the 'ionospheric part') is defined as follows: we divide the magnetic flux into small tubes (see Figure 2–4) and consider the force that the closed current within the small tube contributes to the plasma sheet dynamics; in this way, we can identify the part of the plasma sheet current that is related to the ionospheric drag force on each flux tube. Therefore, the ionospheric part of the plasma sheet current [*Akasofu et al.*, 1981] is defined as

$$\mathbf{I}^i_{x,y} \cdot d\mathbf{s} = -\mathbf{I}_i \cdot d\mathbf{s}_i \tag{2 · 13}$$

where $d\mathbf{s}_i$ is the mapping image of $d\mathbf{s}$ through the geomagnetic field. The rest of the plasma sheet current ($\mathbf{I}^m_{x,y}$) is referred to as the 'magnetospheric part' of the plasma sheet current. Since all divergence of $\mathbf{I}_{x,y}$ has to be related to the ionospheric current through the field-aligned current, the magnetospheric part of the plasma sheet current has to be divergence free:

$$\nabla_{x,y} \cdot \mathbf{I}^m_{x,y} = 0$$

Now, we further divide the magnetospheric part into a closed one and an open one. The open system is given as the boundary condition, and the closed one is

the system that develops inside the magnetosphere; e.g., it is a toroidal current system that closes inside the plasma sheet.

$$\mathbf{I}^m_{x,y} = \mathbf{I}^o_{x,y} + \mathbf{I}^c_{x,y} \qquad (2 \cdot 12')$$

This notation is useful if the outside of the region which we consider is kept steady (or we consider the region where the time dependence is more important than elsewhere). In this case, $\mathbf{I}^o$ is constant, the boundary value of $\mathbf{I}^i$ is given in terms of $\mathbf{I}_i$ and is constant too, and only $\mathbf{I}^c$ is difficult to specify. If $\mathbf{I}^c$ is given externally, we may calculate $\mathbf{I}_{x,y}$.

Once we can specify $\mathbf{I}_{x,y}$, we can use the expression (2·5') instead of (2·5) for the momentum equation. Therefore, we do not have to obtain $\mathbf{B}_{x,y}$. Otherwise, we have to go through the following procedure to obtain $\mathbf{B}_{x,y}$ first. According to Ampere's law (e.g., equation (2·6)), $\mathbf{B}_{x,y}$ is mainly determined by $\mathbf{J}_{x,y}$

$$\frac{\partial}{\partial z}(\hat{z} \times \mathbf{B}_{x,y}) - \hat{z} \times \nabla_{x,y} B_z = \mu_0 \mathbf{J}_{x,y}$$

However, its variation in the x, y direction is caused by J_z because of the current continuity under the quasi-neutrality. The value of $\mathbf{B}_{x,y}$ itself is a consequence of the x, y variation added to the x or y boundary value which represents the current system outside of that boundary. Thus, we just have to specify the x, y variation

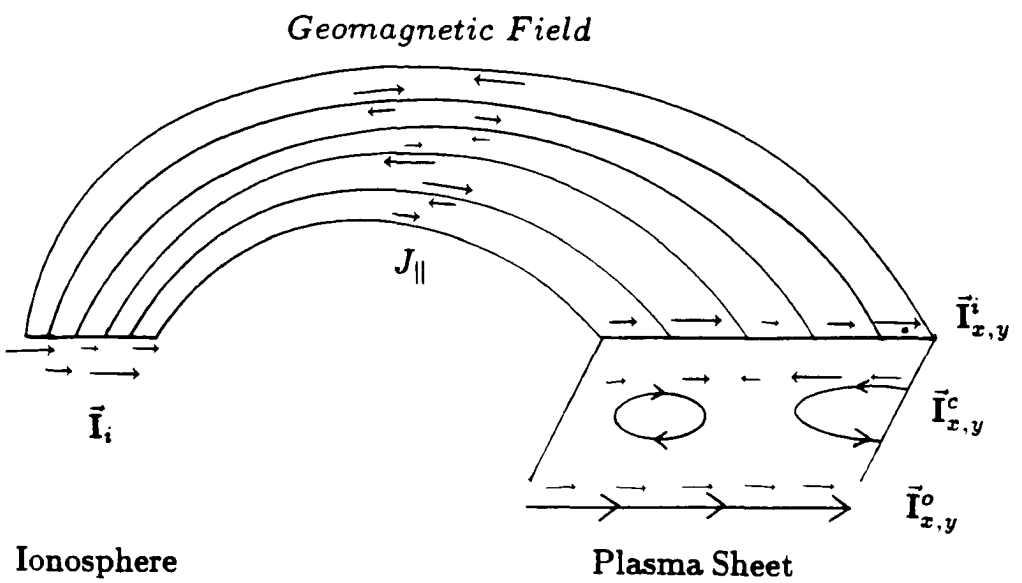

Figure 2–4. Closure of the magnetospheric current. The magnetospheric part of the plasma sheet current ($\mathbf{I}^m$) is defined as $\mathbf{I} - \mathbf{I}^i$, where $\mathbf{I}^i \times \mathbf{B}$ is exactly the same as $-\mathbf{F}^i$ which is shown in Figure 2–3. $\mathbf{I}^m$ is further divided into a closed part ($\mathbf{I}^c$) and an open part ($\mathbf{I}^o$).

completely; i.e., the divergence and the rotation of $\mathbf{B}_{x,y}$:

$$\nabla_{x,y}\cdot\mathbf{B}_{x,y}(z=h) = -\frac{\partial}{\partial z}B_z(z=h) \qquad (2\cdot 14a)$$

$$\frac{\partial}{\partial z}\nabla_{x,y}(\hat{z}\times\mathbf{B}_{x,y}) = \mu_0\nabla_{x,y}\cdot\mathbf{J}_{x,y} + \nabla_{x,y}(\hat{z}\times\nabla_{x,y}B_z)$$

$$= -\frac{\partial}{\partial z}(\mu_0 J_z)$$

$$or \qquad \nabla_{x,y}(\hat{z}\times\mathbf{B}_{x,y})_{z=h} = -\mu_0 J_z(z=h) \qquad (2\cdot 14b)$$

where we used the current continuity equation $\partial J_z/\partial z = -\nabla_{x,y}\cdot\mathbf{J}_{x,y}$. From these equations, $\mathbf{B}_{x,y}$ can be expressed as

$$\nabla^2_{x,y}\mathbf{B}_{x,y}(z=h) = \hat{z}\times\nabla_{x,y}[\nabla_{x,y}(\hat{z}\times\mathbf{B}_{x,y})]_{z=h} + \nabla_{x,y}[\nabla_{x,y}\cdot\mathbf{B}_{x,y}]_{z=h}$$

$$= \mu_0\hat{z}\times\nabla_{x,y}J_z(z=h) - \nabla_{x,y}\frac{\partial}{\partial z}B_z(z=h)$$

$$= \mu_0\hat{z}\times\nabla_{x,y}J_z(z=h) + \nabla_{x,y}(\nabla_{x,y}\cdot\mathbf{B}_{x,y})_{z=h} \qquad (2\cdot 15)$$

This method is very clumsy. Furthermore, we still have the problem of specifying the boundary conditions. Therefore, we use $\mathbf{I}_{x,y}$ instead of $\mathbf{B}_{x,y}$.

Let us obtain the equations for B_z. The induction equation is used to determine B_z.

$$\frac{\partial}{\partial t}B_z = \nabla_{x,y}\times(\mathbf{u}\times\mathbf{B})_{x,y}$$

$$= -\nabla_{x,y}\cdot(B_z\mathbf{u}_{x,y}) + \nabla_{x,y}\cdot(u_z\mathbf{B}_{x,y})$$

$$= -\nabla_{x,y}\cdot(B_z\mathbf{V}_{x,y}) \qquad (2\cdot 16)$$

where we used $u_z \ll u_{x,y}$. The x, y components of the induction equation are not used because they are strongly related to u_z (for the motion of the flux). The

small quantity u_z is not determined self-consistently, and should not affect the result. It is a quantity to be assumed in the height-integrated equations, instead. Thus, B_x and B_y are to be solved (through J_z as was previously shown) by the current continuity equation of the M-I coupling system, i.e., in the ionosphere.

So far we have a set of the equations (2·4), (2·5'), (2·11), (2·12), and (2·16) in the plasma sheet. In order to complete these equations, we have to relate J_z or $\mathbf{I}_i$ to $\mathbf{E}_{x,y} = -\mathbf{V}_{x,y}B_z \times \hat{z}$ by taking the ionosphere into account. Note that if the plasma sheet is treated fully three dimensionally, the constraint associated with the z component quantities, e.g., (2·8), becomes one of the boundary conditions at $z = h$.

2–2. Ionospheric Loading Effect

As previously discussed, we employ the ionospheric Ohm's law in order to provide current-electric relation. The height-integrated ionospheric current $\mathbf{I}_i$ is expressed as [*Brekke et al.*, 1974]

$$\mathbf{I}_i = \Sigma'_P \mathbf{E}_i^{(eff)} - \Sigma'_H \mathbf{E}_i^{(eff)} \times \frac{\mathbf{B}_i}{B_i}$$

where Σ'_P and Σ'_H are the height-integrated Pedersen conductivity and the Hall conductivity in the ionosphere, $\mathbf{E}_i^{(eff)} = -\nabla_i \Phi_i + \mathbf{V}_n \times \mathbf{B}_i$ is the ionospheric electric field, and Φ_i is the ionospheric electric potential. The electric field is measured on a reference frame co-moving with the ionospheric neutral wind (velocity

$\mathbf{V}_n$) which is driven mainly by the i-n collisions [*Sonnerup*, 1980]. Although the response time of $\mathbf{V}_n$ is comparable to the scale time of the magnetospheric convection, we simply assume $\mathbf{V}_n = (1-\eta^*)(-\nabla_i\Phi_i) \times \mathbf{B}_i/B_i^2$ where $0 \leq \eta^* \leq 1$ is a constant factor. With this assumption, the above equation is rewritten as

$$\mathbf{I}_i = -\Sigma_P \nabla_i \Phi_i + \Sigma_H \nabla_i \Phi_i \times \frac{\mathbf{B}_i}{B_i} \qquad (2 \cdot 17)$$

where $\Sigma_P \equiv \eta^* \Sigma'_P$ and $\Sigma_H \equiv \eta^* \Sigma'_H$ are the effective conductivities.

Divergence of this ionospheric current becomes the field-aligned current. Let us assume no leakage of the field-aligned currents between the magnetosphere and the ionosphere [e.g., *Lotko et al.*, 1987; *Harel et al.*, 1981]. The current continuity condition requires $(J_z/B_z)_{z=h} = (J_\parallel/B)_{z=h} = -(J_\parallel/B)_i = -(J_z/B)_i$ and

$$\begin{aligned} J_z(z=h)dxdy &= -(J_z)_i dx_i dy_i \\ &= +\nabla_i \cdot \mathbf{I}_i dx_i dy_i \end{aligned}$$

where $B_z(z=h)dxdy = B_i dx_i dy_i$, subscript '$i$' denotes the quantities in the ionosphere, and both $(\hat{x}, \hat{y}, \mathbf{B}_z/B_z)$ and $(\hat{x}_i, \hat{y}_i, \mathbf{B}_i/B_i)$ are determined as the right-hand coordinate systems. Using the Jacobian:

$$\frac{\partial(x_i, y_i)}{\partial(x, y)} = \frac{B_z(z=h)}{B_i} \qquad (2 \cdot 18)$$

the above relation is expressed as

$$J_z(z=h) = \frac{\partial(x_i, y_i)}{\partial(x, y)} \nabla_i \cdot \mathbf{I}_i \qquad (2 \cdot 19)$$

With the help of equation (2·13), we can specify all components of the current in the plasma sheet in terms of the ionospheric current.

Substituting (2·17) into (2·19), we have

$$J_z(z=h) = -\frac{\partial(x_i, y_i)}{\partial(x, y)} \nabla_i \cdot (\Sigma_P \nabla_i \Phi_i) + \frac{\partial(x_i, y_i)}{\partial(x, y)} \frac{\mathbf{B}_i}{B_i} \cdot (\nabla_i \Sigma_H \times \nabla_i \Phi_i)] \qquad (2 \cdot 20)$$

Meanwhile, equations (2·13) and (2·17) give a relation between $\mathbf{I}^i_{x,y}$ and Φ_i.

If the mapping between the ionosphere and the plasma sheet is conformal (preserving angles) as is exactly the case when the geomagnetic field is the dipole field, equation (2·13) becomes

$$I^i_x = -\frac{\partial(y_i)}{\partial(y)} I_{ix} \qquad (2 \cdot 21x)$$

$$I^i_y = -\frac{\partial(x_i)}{\partial(x)} I_{iy} \qquad (2 \cdot 21y)$$

when combined with (2·17),

$$\mathbf{I}^i_{x,y} = \frac{\partial y_i}{\partial y} \Sigma_P \hat{x}_i \frac{\partial \Phi_i}{\partial x_i} - \frac{\partial y_i}{\partial y} \Sigma_H (\hat{y}_i \frac{\partial \Phi_i}{\partial y_i}) \times \frac{\mathbf{B}_i}{B_i} + \frac{\partial x_i}{\partial x} \Sigma_P \hat{y}_i \frac{\partial \Phi_i}{\partial y_i} - \frac{\partial x_i}{\partial x} \Sigma_H (\hat{x}_i \frac{\partial \Phi_i}{\partial x_i}) \times \frac{\mathbf{B}_i}{B_i} \qquad (2 \cdot 22)$$

where both (x, y) and (x_i, y_i) are assumed to be orthogonal systems.

2–3. Mapping between the Ionosphere and the Plasma Sheet

Along the magnetic field, provided that the mapping is specified, we may relate Φ_i and Φ_m, where Φ_m is obtained as:

$$\begin{aligned} \nabla^2_{x,y}\Phi_m &= -\nabla_{x,y}\cdot\mathbf{E}_{x,y} \\ &= \nabla_{x,y}\cdot(\mathbf{V}_{x,y}B_z\times\hat{z}) \end{aligned} \qquad (2\cdot 23)$$

Though some authors assume $\Phi_i - \Phi_m \propto J_\parallel$ [*Lotko et al.*, 1987; *Watanabe et al.*, 1986; *Harel et al.*, 1981], we assume $\Phi_i = \Phi_m$ for simplicity because our viewpoint is more on the plasma sheet. We have another expression for the potential electric field; i.e., the potential field is given as the total field minus the solenoidal field $\mathbf{E}_t = \nabla_{x,y}\Psi\times\hat{z}$. Once Ψ is solved as:

$$\begin{aligned} \nabla^2_{x,y}\Psi &= \nabla_{x,y}\cdot(\hat{z}\times\mathbf{E}_t) \\ &= \nabla_{x,y}\cdot(\hat{z}\times\mathbf{E}_{x,y}) \\ &= -\nabla_{x,y}\cdot(\mathbf{V}_{x,y}B_z) \end{aligned} \qquad (2\cdot 24)$$

this Ψ can determine the potential electric field as:

$$\begin{aligned} -\nabla_{x,y}\Phi &= \mathbf{E}_{x,y}(z=h) - \mathbf{E}_t \\ &= \hat{z}\times(\mathbf{V}_{x,y}B_z + \nabla_{x,y}\Psi) \end{aligned} \qquad (2\cdot 25)$$

This expression is useful especially when B_z is time independent as equation (2·16) guarantees $\Psi = 0$ in this case.

Now, we have to specify the mapping of the electric potential through the magnetic field. The potential field does not change the mapping points; hence, we have only to consider the temporal change of the magnetic field configuration by $\mathbf{E}_t$ through $\partial\mathbf{B}/\partial t$. Since the solenoidal field is usually smaller than the potential field (think about a steady state when the mapping points do not change at all), we usually neglect this effect in the analytical study later.

The motion of the foot point is described by the drift velocity related only to the solenoidal electric field [*Wolf and Spiro*, 1985]. Let $(x,y)_{z=h}$ be the mapping point of (x_i, y_i) at time t. At $t+\delta t$, the mapping point moves as:

$$\begin{aligned} x(t+\delta t)_{z=h} &= x(t)_{z=h} + U_x \delta t \\ y(t+\delta t)_{z=h} &= y(t)_{z=h} + U_y \delta t \\ dx(t+\delta t)_{z=h} &= (1 + \frac{\partial U_x}{\partial x}\delta t) dx(t)_{z=h} \\ dy(t+\delta t)_{z=h} &= (1 + \frac{\partial U_y}{\partial y}\delta t) dy(t)_{z=h} \end{aligned} \qquad (2 \cdot 26)$$

where $\mathbf{U}_{x,y}$ is the drift velocity related to the solenoidal electric field:

$$\begin{aligned} \mathbf{U}_{x,y} &= \frac{\mathbf{E}_t \times \mathbf{B}}{B^2} \\ &= \mathbf{V}_{x,y} + \frac{\nabla_{x,y}\Phi \times \mathbf{B}_z}{B^2} \\ &= -\frac{B_z}{B^2}\nabla_{x,y}\Psi \end{aligned} \qquad (2 \cdot 27)$$

Note that $\mathbf{U}_{x,y} = 0$ in the steady state.

Inclusion of (2·26) enables us to study the field-aligned current generation that is cause by the temporal change of the geomagnetic field. Otherwise, however, we may neglect this effect and we assume the mapping relation is time independent.

2–4. A Simplified Mapping Model

In the above (rather strict) formulation, $J_z(z=h)$ is obtained by solving the current continuity equation in the ionosphere. This procedure is inevitable if a global model is considered by using rather realistic model magnetic fields for mapping between the ionosphere and the magnetosphere. However, we may remove this geometrical complication if we are to extract some essential physical processes of the M-I coupling system. For example, when the mapping is conformal (preserves angles), we may 'map' the ionospheric Ohm's law to the magnetosphere as a whole equation if we use "mapped" ionospheric conductivity to the magnetosphere.

Figure 2–5 shows area elements in the ionosphere and corresponding area elements in the magnetosphere. Figure 2–5*a* (left) shows a general case, and 2–5*b* (right) shows a simplified conformal case. Unless we consider the cases when the complicated mapping geometry is important in generating the field-aligned currents, we simplify the mapping to be conformal as is given as (2·21); i.e., $\partial x_i/\partial y = 0$, $\partial y_i/\partial x = 0$, and

$$dx_i = \xi_x(x, y, t)dx$$

$$dy_i = \xi_y(x, y.t)dy \qquad (2 \cdot 28)$$

where the mapping factors ξ_x, ξ_y are assumed to be uniform for the same reason.

These factors are subject to change as time proceeds because of the plasma convection in the magnetosphere. Thus, we finally have

$$\begin{aligned}\frac{\partial}{\partial t}(\xi_x, \xi_y) &= (-\frac{\partial U_x}{\partial x}\xi_x, -\frac{\partial U_y}{\partial y}\xi_y) \\ &= (\xi_x \frac{\partial}{\partial x}[\frac{B_z}{B^2}\frac{\partial \Psi}{\partial x}], \xi_y \frac{\partial}{\partial y}[\frac{B_z}{B^2}\frac{\partial \Psi}{\partial y}])\end{aligned} \qquad (2 \cdot 29)$$

As discussed above, we do not use this equation in the most of the study and set ξ constant unless we specifically study the effect of the geometrical change on the generation of the field-aligned current. With these factors, we have $\partial/\partial x_i = (dx/dx_i)\partial/\partial x = (1/\xi_x)\partial/\partial x$, etc., and the Jacobian (2·18) is expressed also as

$$\frac{\partial(x_i, y_i)}{\partial(x, y)} = \xi_x \xi_y$$

Under this simple mapping relation, the ionospheric current and the magnetospheric convection have more direct relationship as shown below.

Let us restrict consideration to the Φ_i=Φ_m case. The current continuity equation (2·20) becomes

$$\begin{aligned}J_z(z=h) &= -\xi_x\xi_y[\frac{\partial}{\partial x_i}(\Sigma_P \frac{\partial \Phi}{\partial x_i}) + \frac{\partial}{\partial y_i}(\Sigma_P \frac{\partial \Phi}{\partial y_i})] + \xi_x\xi_y[\frac{\partial \Sigma_H}{\partial x_i}\frac{\partial \Phi}{\partial y_i} - \frac{\partial \Sigma_H}{\partial y_i}\frac{\partial \Phi}{\partial x_i}] \\ &= -\frac{\xi_y}{\xi_x}\frac{\partial}{\partial x}(\Sigma_P^{(m)}\frac{\partial \Phi}{\partial x}) - \frac{\xi_x}{\xi_y}\frac{\partial}{\partial y}(\Sigma_P^{(m)}\frac{\partial \Phi}{\partial y}) + [\frac{\partial \Sigma_H^{(m)}}{\partial x}\frac{\partial \Phi}{\partial y} - \frac{\partial \Sigma_H^{(m)}}{\partial y}\frac{\partial \Phi}{\partial x}]\end{aligned}$$

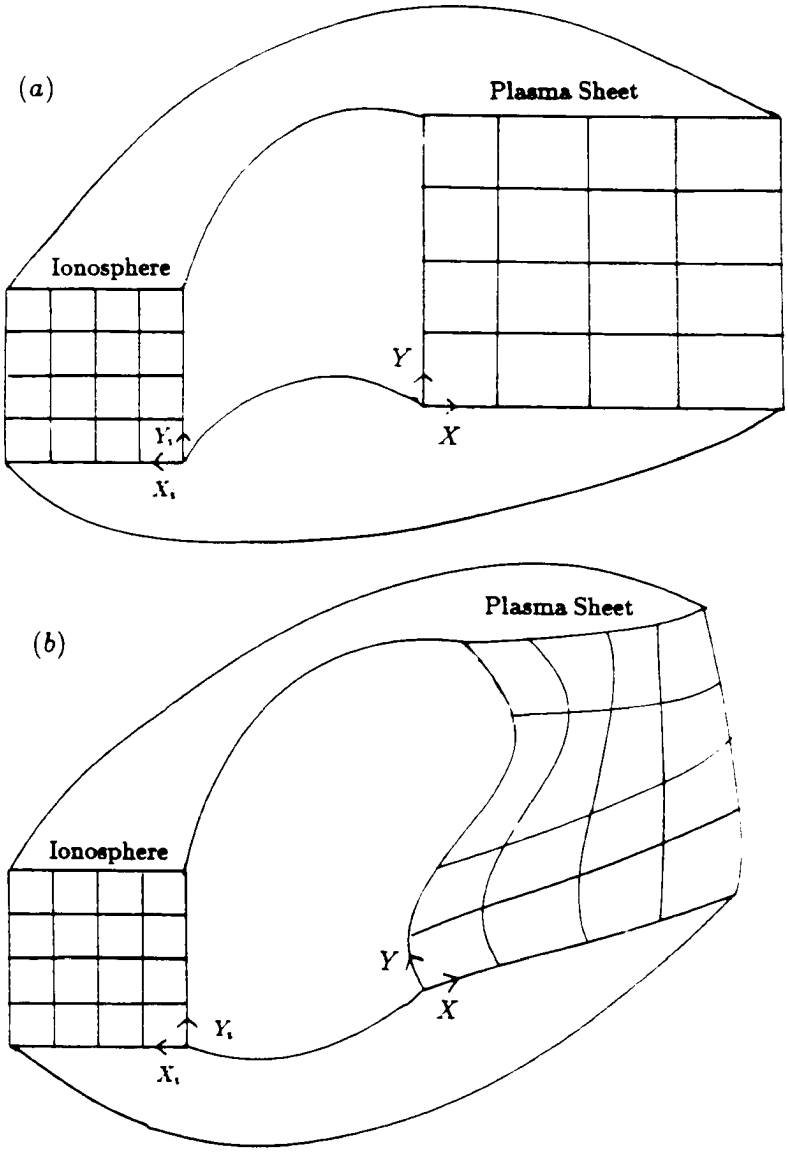

Figure 2–5. Mapping relations. Between the ionosphere and the magnetosphere, (a) a conformal mapping is assumed in the present model, which is simplified from (b) the complicated real mapping.

$$= -\frac{\xi_y}{\xi_x}\frac{\partial}{\partial x}[\Sigma_P^{(m)}(\frac{\partial \Psi}{\partial y} + V_y B_z)] + \frac{\xi_x}{\xi_y}\frac{\partial}{\partial y}[\Sigma_P^{(m)}(\frac{\partial \Psi}{\partial x} + V_x B_z)]$$
$$- \nabla_{x,y}\Sigma_H^{(m)} \cdot (\mathbf{V}_{x,y} B_z + \nabla_{x,y}\Psi) \qquad (2 \cdot 30)$$

where $\Sigma^{(m)}$ is the ionospheric height-integrated conductivity mapped to the plasma sheet, and we used $\mathbf{B}_i/B_i = \mathbf{B}_z/B_z = \hat{z}$. The first two terms are related to the divergence of the Pedersen current, while the last term is related to the inhomogeneity of the Hall conductivity. Let us take x_i northward (take x tailward) in which direction the convection is flowing. Since ξ_x is normally smaller than ξ_y (<1), the first bracket is usually larger than the second bracket. The last term could be important in generating the field-aligned current when the flow experiences the gradient of Σ_H. Note that the time dependence of the mapping relation also reflects the mapped values of the ionospheric conductivities.

The ionospheric part of the magnetospheric current (2·22) becomes

$$\mathbf{I}^i_{x,y} = (\frac{\xi_y}{\xi_x}\Sigma_P^{(m)}\frac{\partial \Phi}{\partial x} - \Sigma_H^{(m)}\frac{\partial \Phi}{\partial y})\hat{x} + (\frac{\xi_x}{\xi_y}\Sigma_P^{(m)}\frac{\partial \Phi}{\partial y} + \Sigma_H^{(m)}\frac{\partial \Phi}{\partial x})\hat{y}$$
$$= [\frac{\xi_y}{\xi_x}\Sigma_P^{(m)}(\frac{\partial \Psi}{\partial y} + V_y B_z) + \Sigma_H^{(m)}(\frac{\partial \Psi}{\partial x} + V_x B_z)]\hat{x}$$
$$+ [-\frac{\xi_x}{\xi_y}\Sigma_P^{(m)}(\frac{\partial \Psi}{\partial x} + V_x B_z) + \Sigma_H^{(m)}(\frac{\partial \Psi}{\partial y} + V_y B_z)]\hat{y} \qquad (2 \cdot 31)$$

Even though the energy dissipation should come only from the Pedersen current, we still have the contribution from the Hall conductivity in (2·31).

In both (2·30) and (2·31), the geometrical difference between the coupled ionosphere and the magnetosphere is condensed into ξ, and all the ionospheric quantities are expressed in terms of the mapped quantities. In this way, we have a simple 2-D equation set for the M-I coupling system. One can easily see that (2·30) and (2·31) satisfies

$$J_z(z=h) = -\nabla_{x,y}\cdot\mathbf{I}^{\mathrm{i}}_{x,y} \qquad (2\cdot 32)$$

and hence it is consistent with $\nabla_{x,y}\cdot\mathbf{I}^{m}_{x,y} = 0$ too.

2–5. Summary of the Basic Equations

As shown above, we have obtained basic equations for the height-integrated plasma sheet which is coupled with the ionosphere.

$$m\frac{\partial}{\partial t}\mathbf{V}_{x,y} = -m(\mathbf{V}_{x,y}\cdot\nabla_{x,y})\mathbf{V}_{x,y} - \nabla_{x,y}\pi + \mathbf{I}_{x,y}\times\mathbf{B}_z + h\zeta\mu_0 J_z\mathbf{I}_{x,y} \qquad (2\cdot 5')$$

$$\mathbf{I}_{x,y} = \mathbf{I}^{\mathrm{i}}_{x,y} + \mathbf{I}^{m}_{x,y} \qquad (2\cdot 12)$$

$$\frac{\partial}{\partial t}m = -\nabla_{x,y}\cdot(m\mathbf{V}_{x,y}) + T_z\rho(z=h) \qquad (2\cdot 4)$$

$$\frac{\partial}{\partial t}\pi = -\nabla_{x,y}\cdot(\pi\mathbf{V}_{x,y}) + T_zP(z=h) - (\gamma-1)\pi\nabla_{x,y}\cdot\mathbf{V}_{x,y} \qquad (2\cdot 11')$$

$$\frac{\partial}{\partial t}B_z = -\nabla_{x,y}\cdot(B_z\mathbf{V}_{x,y}) \qquad (2\cdot 16)$$

$$\mathbf{I}^{\mathrm{i}}_{x,y} = \left(\frac{\xi_y}{\xi_x}\Sigma_P^{(m)}\frac{\partial\Phi}{\partial x} - \Sigma_H^{(m)}\frac{\partial\Phi}{\partial y}\right)\hat{x} + \left(\frac{\xi_x}{\xi_y}\Sigma_P^{(m)}\frac{\partial\Phi}{\partial y} + \Sigma_H^{(m)}\frac{\partial\Phi}{\partial x}\right)\hat{y}$$

or

$$= \left[\frac{\xi_y}{\xi_x}\Sigma_P^{(m)}\left(\frac{\partial\Psi}{\partial y} + V_yB_z\right) + \Sigma_H^{(m)}\left(\frac{\partial\Psi}{\partial x} + V_xB_z\right)\right]\hat{x}$$

$$+[-\frac{\xi_x}{\xi_y}\Sigma_P^{(m)}(\frac{\partial\Psi}{\partial x}+V_xB_z)+\Sigma_H^{(m)}(\frac{\partial\Psi}{\partial y}+V_yB_z)]\hat{y} \qquad (2\cdot 31)$$

$$\nabla_{x,y}^2\Phi=[\nabla_{x,y}\times(\mathbf{V}_{x,y}B_z)]_z \qquad (2\cdot 23)$$

or $$\nabla_{x,y}^2\Psi=-\nabla_{x,y}(\mathbf{V}_{x,y}B_z) \qquad (2\cdot 24)$$

$$J_z(z=h)=-\nabla_{x,y}\mathbf{I}_{x,y}^i \qquad (2\cdot 32)$$

$$=-\frac{\xi_y}{\xi_x}\frac{\partial}{\partial x}(\Sigma_P^{(m)}\frac{\partial\Phi}{\partial x})-\frac{\xi_x}{\xi_y}\frac{\partial}{\partial y}(\Sigma_P^{(m)}\frac{\partial\Phi}{\partial y})+[\nabla\Sigma_H^{(m)}\times\nabla\Phi_m]_z$$

or $$=-\frac{\xi_y}{\xi_x}\frac{\partial}{\partial x}[\Sigma_P^{(m)}(\frac{\partial\Psi}{\partial y}+V_yB_z)]+\frac{\xi_x}{\xi_y}\frac{\partial}{\partial y}[\Sigma_P^{(m)}(\frac{\partial\Psi}{\partial x}+V_xB_z)]$$

$$-\nabla_{x,y}\Sigma_H^{(m)}\cdot(\mathbf{V}_{x,y}B_z+\nabla_{x,y}\Psi) \qquad (2\cdot 30)$$

$$\nabla_{x,y}\mathbf{I}_{x,y}^m=0$$

where Σ_H is positive, and T_z (unit mass transfer across $z=h$ boundary as defined in (2·3)) is to be given externally so that the plasma sheet thinning or expansion near the plasmapause can be included as well as the compression by the equatorial convection. The magnetospheric part of current $\mathbf{I}_{x,y}^m$ is given as the initial conditions. The height of the plasma sheet h has to satisfy

$$\frac{\pi}{B_{x,y}^2(z=h)/2\mu_0}=O(h) \qquad (2\cdot 9)$$

after the end of the calculation. Unless we stress the effect of the geometrical change on the field-aligned current generation, we assume ξ constant, and we do not employ equation (2·29), which is

$$\frac{\partial}{\partial t}(\xi_x,\xi_y)=(\xi_x\frac{\partial}{\partial x}[\frac{B_z}{B^2}\frac{\partial\Psi}{\partial x}],\xi_y\frac{\partial}{\partial y}[\frac{B_z}{B^2}\frac{\partial\Psi}{\partial y}]) \qquad (2\cdot 29)$$

Note that $\Psi=0$ for the steady state.

Chapter 3. Steady-State Solutions

Based on the two layer model summarized in section 2–5, we obtain steady-state analytical solutions under simplified assumptions. These solutions can be used as the initial configurations for the simulation as well as the 0'th order configuration for the linear perturbation analysis. Since more complicated (e.g., time dependent, etc.) solutions will be studied in terms of the linear analysis or the numerical simulation, we concentrate on simple situations.

Four types of flows are presented in this chapter. They are: *1.* static equilibrium ($\mathbf{V}_{x,y} = 0$); *2.* incompressible parallel flow in the x direction; *3.* compressible parallel 1-D ($\partial/\partial y = 0$) flow in the x direction; *4.* incompressible circular flow ($V_r = 0$, and $\partial/\partial\phi = 0$). We do not add any complicated x, y dependence on these flows. The common assumptions for these flows are: *1.* $\partial/\partial t = 0$ (steady-state flow) ; *2.* $T_z = 0$ (no thinning nor expansion of the plasma sheet); *3.* $\Sigma_H \propto \Sigma_P = uniform$ (uniform conductivities); *4.* $\xi_x/\xi_y = uniform$ (uniform mapping); and *5.* $J_z = 0$ (no field-aligned current). As a direct consequence of the steady-state assumption, we have $\Psi = 0$ according to equations (2·16) and (2·24) of chapter 2.

To begin with, let us express the electric currents in terms of the convection velocity and the pressure. The momentum equation provides an expression for total plasma sheet current ($\mathbf{I}_{x,y}$) in terms of the height averaged velocity ($\mathbf{V}_{x,y}$), the height integrated density (m), and the height integrated pressure (π). The

ionospheric part ($\mathbf{I}^i_{x,y}$) is also expressed directly in terms of $\mathbf{V}_{x,y}$ and π (we now have $\Psi = 0$) through the ionospheric Ohm's law. Therefore, we may also determine the magnetospheric part ($\mathbf{I}^m_{x,y}$) by subtracting these two.

$$\mathbf{I}_{x,y} = \frac{\mathbf{B}_z}{B_z^2} \times [m(\mathbf{V}_{x,y}\cdot\nabla_{x,y})\mathbf{V}_{x,y} + \nabla_{x,y}\pi] \tag{3·1}$$

$$I^i_x = \frac{\xi_y}{\xi_x}\Sigma_P V_y B_z + \Sigma_H V_x B_z \tag{3·2}$$

$$I^i_y = -\frac{\xi_x}{\xi_y}\Sigma_P V_x B_z + \Sigma_H V_y B_z \tag{3·3}$$

$$\mathbf{I}^m_{x,y} = \mathbf{I}_{x,y} - \mathbf{I}^i_{x,y} \tag{3·4}$$

Thus, we can obtain the driving force $\mathbf{I}^m_{x,y} \times \mathbf{B}_z$ from the assumed values of $\mathbf{V}_{x,y}$ and π, even though $\mathbf{I}^m_{x,y}$ is a quantity that is given externally. This force maintains the convention flowing against the ionospheric drag force.

The other basic equations of section 2–5 provide the conditions that the convection has to obey.

$$\nabla_{x,y}(m\mathbf{V}_{x,y}) = 0 \tag{3·5}$$

$$\nabla_{x,y}(\pi\mathbf{V}_{x,y}) = -(\gamma-1)\pi\nabla_{x,y}\cdot\mathbf{V}_{x,y} \tag{3·6}$$

$$\nabla_{x,y}(B_z\mathbf{V}_{x,y}) = 0 \tag{3·7}$$

$$\begin{aligned} J_z(z=h) &= \Sigma_P[-\frac{\xi_y}{\xi_x}\frac{\partial}{\partial x}(V_y B_z) + \frac{\xi_x}{\xi_y}\frac{\partial}{\partial y}(V_x B_z)] \\ &= 0 \end{aligned} \tag{3·8}$$

$$\nabla_{x,y}\mathbf{I}^m_{x,y} = \frac{\partial}{\partial y}[\frac{m\mathbf{V}_{x,y}\cdot\nabla_{x,y}V_x}{B_z}] - \frac{\partial}{\partial x}[\frac{m\mathbf{V}_{x,y}\cdot\nabla_{x,y}V_y}{B_z}]$$

$$+\frac{\partial\pi}{\partial x}\frac{\partial}{\partial y}\left(\frac{1}{B_z}\right)-\frac{\partial\pi}{\partial y}\frac{\partial}{\partial x}\left(\frac{1}{B_z}\right)$$

$$=0 \qquad (3\cdot 9)$$

Once the convection velocity satisfies these equations, all the forces are cancelled, so that the $\partial/\partial t$ term becomes zero even if we did not assume the steady-state.

3–1. Static Equilibrium without Flow

We first assume $\mathbf{V}_{x,y}=0$. The ionospheric part of the basic equations provides $J_z=0$, which is consistent with this assumption. The basic equations and a condition of z component momentum balance become:

$$\mathbf{I}^m_{x,y}=\mathbf{I}_{x,y}$$

$$=\frac{\mathbf{B}_z}{B_z^2}\times\nabla_{x,y}\pi \qquad (3\cdot 10)$$

$$\nabla_{x,y}B_z\times\nabla_{x,y}\pi=0 \qquad (3\cdot 11)$$

$$-P(z=0)+\frac{1}{2\mu_0}B^2_{x,y}(z=h)=\frac{2\zeta}{1+\zeta}\frac{h}{\mu_0}\nabla_{x,y}B_z\cdot\mathbf{B}_{x,y}(z=h) \qquad (3\cdot 12)$$

The pressure distribution in the z direction is, in general, not uniform. This fact reflects the bending of the geomagnetic field. The degree of the non-uniformity in the z direction is condensed into the factor ζ in equation (2·5') of the previous chapter. For example, the least bending case of a dipole field is achieved when $\partial P/\partial z=0$, which is represented by $\zeta=1$ as shown below. Let us take the origin

of the Cartesian coordinate at the center of a dipole moment $\vec{a} = a\hat{z}$. The magnetic field is expressed as

$$\mathbf{B}_{x,y} = \frac{3az}{r^5}(x, y) \qquad (3 \cdot 13)$$

$$B_z = \frac{-a}{r^3}(1 - 3\frac{z^2}{r^2}) \qquad (3 \cdot 14)$$

$$or \qquad \nabla_{x,y} B_z = \frac{1}{z}(1 - 5\frac{z^2}{r^2})\mathbf{B}_{x,y}$$

where r is the distance from the origin. As the expression (3·13) shows, ζ has to be unity. If we neglect $z^2/r^2 \ll 1$, which is good approximation near the plasma sheet, we have

$$\mathbf{B}_{x,y} = z\nabla_{x,y} B_z$$

$$or \qquad \frac{{B_{x,y}}^2(z=h)}{2\mu_0} = \frac{h}{2\mu_0}\nabla_{x,y} B_z \cdot \mathbf{B}_{x,y}(z=h) \qquad (\mathbf{3} \cdot 15)$$

This equation is identical to (3·12). On the other hand, since there is no pressure gradient and there is no current in the dipole field, equations (3·10) and (3·11) are automatically satisfied. Thus, the two layer interface model includes the case of the dipole magnetic field if we neglect $h^2/r^2 \ll 1$. This is the degree of the approximation for the basic equations.

3–2. Incompressible Parallel Flow

Suppose there is an uniform flow which satisfies $V_y = 0$ and $V_x = V(y)$ as shown in Figure 3-1*a*. In this incompressible situation, equations (3·5) – (3·7) require that m, π, and B_z ($\neq 0$) are also constant along the stream line (in the x direction). Therefore, condition (3·9) is automatically satisfied.

The equations for the electric current (3·1) – (3·4) are simplified to

$$\mathbf{I}_{x,y} = -\hat{x}\frac{1}{B_z}\frac{\partial \pi}{\partial y} \tag{3·16}$$

$$I_x^i = \Sigma_H V B_z \tag{3·17}$$

$$I_y^i = -\frac{\xi_x}{\xi_y}\Sigma_P V B_z \tag{3·18}$$

$$\mathbf{I}_{x,y}^m = \mathbf{I}_{x,y} - \mathbf{I}_{x,y}^i \tag{3·19}$$

and the condition for the self-consistency (3·8) is rewritten as

$$\frac{\partial}{\partial y}(VB_z) = 0 \tag{3·20}$$

Even though there is no field-aligned current, the ionosphere still consumes the energy through Joule heating. It causes an effective drag force working on the plasma sheet, as discussed in section 2–1. The driving force maintaining the steady-state convection is the $\mathbf{J} \times \mathbf{B}$ force supported by the magnetospheric part of the plasma sheet current $\mathbf{I}_{x,y}^m$, which is externally provided. This $\mathbf{J} \times \mathbf{B}$ force is a different expression of the magnetic tension force $B_z \mathbf{B}_{x,y}$ as discussed in the previous chapter (see the explanation for equation (2·7)).

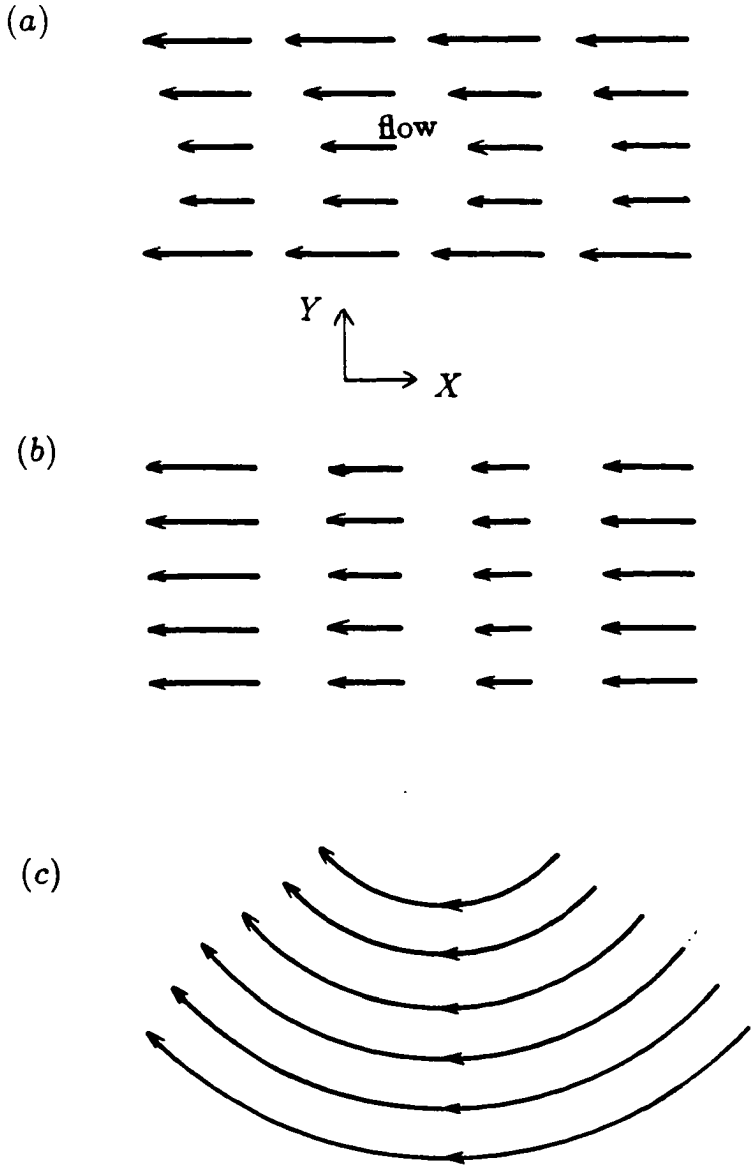

Figure 3–1. Simple flow patterns without field-aligned currents. (a) A shear flow where $B_z V_x$ is constant in the y direction; (b) A 1–D compressible flow; and (c) A circular flow where $rB_z V_\phi$ is constant in the r direction.

The present situation is achieved if the $\mathbf{J} \times \mathbf{B}$ force drives the flow in the x direction, while the plasma pressure adjusts its direction so that the ionospheric Hall current does not alter the flow direction. The field-aligned current generation by the shear flow can be studied in terms of the perturbation method from the uniform convection of the 0'th order. In this case, B_z is also uniform, and hence, the ionospheric drag force is uniform too.

3–3. Compressional 1-D Parallel Flow

For simplicity, the compressional flow is considered to be one dimensional as shown in Figure 3–1*b*. We assume $V_y = 0$, $V_x = V(x)$ and $\pi = \pi(x)$, and the rest of the 1–D conditions ($B_z = B_z(x)$ and $m = m(x)$) are obtained from the above assumptions through the conditions (3·8) and (3·9). This situation is also applicable to finite amplitude 1–D waves. The equations for the electric current (3·1) – (3·4) are simplified to

$$\mathbf{I}_{x,y} = \hat{y}\frac{1}{B_z}\frac{\partial}{\partial x}(mV^2 + \pi) \tag{3·21}$$

$$I_x^m = -I_x^i$$

$$= -\Sigma_H V B_z \tag{3·22}$$

$$I_y^i = -\frac{\xi_x}{\xi_y}\Sigma_P V B_z \tag{3·23}$$

$$I_y^m = I_y - I_y^i \tag{3·24}$$

and the conditions (3·5) – (3·7) for the self-consistency of the flow become

$$\frac{\partial}{\partial x}(mV) = 0$$

$$or \qquad V \propto \frac{1}{m} \tag{3·25}$$

$$\frac{\partial}{\partial x}(\ln\pi + \gamma \ln V) = 0$$

$$or \qquad \pi \propto m^{\gamma} \tag{3·26}$$

$$\frac{\partial}{\partial x}(B_z V) = 0$$

$$or \qquad B_z \propto m \tag{3·27}$$

With the help of (3·25) and (3·26), the gradient of the total kinetic pressure $mV^2 + \pi$ is expressed in terms of the density gradient:

$$\frac{\partial}{\partial x}(mV^2 + \pi) = m^2 V^2 \frac{\partial}{\partial x}(\frac{1}{m}) + \frac{\gamma\pi}{m}\frac{\partial m}{\partial x}$$

$$= (-V^2 + C_S^2)\frac{\partial m}{\partial x}$$

$$where \qquad C_S^2 \equiv \frac{\gamma\pi}{m} \tag{3·28}$$

Therefore, (3·21) is rewritten as

$$I_y = \frac{1}{B_z}(C_S^2 - V^2)\frac{\partial m}{\partial x} \tag{3·29}$$

This equation indicates that the total current direction in the plasma sheet depends on the direction of the density gradient as long as the convection is subsonic. Thus, the plasma sheet current can flow in both the $+y$ and $-y$ directions.

Equations (3·21) – (3·27) represent several situations. If the pressure gradient is the primary force that drives the flow in the x direction, the other quantities are determined from it according to (3·21) – (3·27). In this case, the ionospheric Hall current drags the plasma in the y direction. This drag force has to be cancelled by $\mathbf{I}_x^m \times \mathbf{B}_z$ so that straight flow is maintained. Thus, the external quantity I_x^m is determined from the assumed pressure. If the pressure is rather determined self consistently (e.g., waves), we may still calculate the other quantities from the pressure and vice versa.

Conditions (3·26) and (3·27) are sometimes extended to more general situations when we use the analytical method. We assume these extensions for the 0'th order quantities when we perform the linear analysis.

3–4. Incompressible Circular Flow

In this section, we show a solution of the flow with curvature and with no field-aligned current. The flow does not have to be a circular one. We study the portion in which the flow speed is constant along the curving stream line as shown in Figure 3–1*c*. Let us assume that $V_r = 0$ and V_ϕ $(= V)$ are constant along the stream line. This situation is essentially the same as parallel flow except centripetal force is added. We keep the $\partial\pi/\partial\phi$ term so that it can represent viscous-like stress force.

We again have constant m, π, and B_z along the stream line according to (3·5) - (3·7). With the help of the general relations

$$\frac{\partial}{\partial\phi}\hat{r} = \hat{\phi}$$
$$\frac{\partial}{\partial\phi}\hat{\phi} = -\hat{r}$$

the equations for the electric currents are rewritten as

$$I_r = -\frac{1}{rB_z}\frac{\partial\pi}{\partial\phi} \tag{3·30}$$
$$I_\phi = -\frac{mV^2}{rB_z} + \frac{1}{B_z}\frac{\partial\pi}{\partial r} \tag{3·31}$$
$$I_r^i = \frac{\xi_\phi}{\xi_r}\Sigma_P V B_z \tag{3·32}$$
$$I_\phi^i = \Sigma_H V B_z \tag{3·33}$$
$$(I_r^m, I_\phi^m) = (I_r, I_\phi) - (I_r^i, I_\phi^i)$$

where the centripetal force in (3·31) comes from the convection term:

$$(\mathbf{V}_{x,y}\cdot\nabla_{x,y})\mathbf{V}_{x,y} = -\hat{r}\frac{V^2}{r}$$

The conditions for the self-consistency (3·8) and (3·9) are rewritten as

$$\frac{\partial}{\partial r}(rVB_z) = 0 \tag{3·34}$$
$$\frac{\partial B_z}{\partial r}\frac{\partial\pi}{\partial\phi} = 0 \tag{3·35}$$

If there exists Kelvin-Helmholtz type drag force [*Axford and Hines*, 1961] represented by $\partial\pi/\partial\phi$, the last condition requires that B_z should be uniform. Otherwise, the last condition is automatically satisfied. Nonzero V causes nonzero

$J_r = J_r(r)$ through nonzero B_ϕ. In this case, we need a driven force different from the viscous-like stress force ($\partial\pi/\partial\phi$ term). There is a singular point of J_z at the center of the circular flow, if the convection flows in a closed circle. As we take $V(r \to 0) \to 0$, no flow can satisfy condition (3·34); i.e., there should be the field-aligned current at the center of the vortex. A further study is given later in terms of the linear analysis and the numerical simulation.

Chapter 4. Linear Analysis of the Field-Aligned Current: 1

— Perturbation from Static Equilibrium —

Once we have the zero-order configuration, we may apply the linear perturbation method. This method is commonly used to study the waves [e.g., *Southwood and Stuart* 1980], but not for the plasma sheet dynamics. All variables are divided into the zero-order quantities and the 1st order quantities; e.g., $m + \delta m$, $\mathbf{V} + \delta\mathbf{V}$, etc.. The second order terms are neglected from the equations. Since zero-order J_z is set as zero, the field-aligned current is the perturbed quantity ($=\delta J_z$). We express the field-aligned current in terms of the the other perturbed quantities. We also study the temporal development (or relaxation) of a given initial perturbation to a steady state, its relaxation time, and the field-aligned current generation during these processes. Even though the basic equations are nonlinear, the linear analysis is still useful because it diagnoses the behavior of the nonlinear solutions that are to be obtained in terms of the numerical simulation.

The zero-order configurations are taken from the previous section. There are several assumptions for these steady state configurations. Here, we further simplify the zero-order configuration. Those assumptions are: *1.* $\partial/\partial t = 0$; *2.* $T_z = 0$; *3.* $\Sigma_H \propto \Sigma_P$; *4.* $J_z = 0$; *5.* $\xi_x = \xi_y$; *6.* $\pi \propto m^\gamma$; and *7.* $B_z \propto m$. The first four assumptions are the same as in the previous chapter. The last two assumptions have been explained in section 3–3: they replace the equation of the state and the

z component induction equation self-consistently. Both assumptions are not valid if the T_z terms are not zero. The assumption for ξ is a special case of $\xi_x \propto \xi_y$. That assumption provides $\xi = \sqrt{B_z/B_i}$.

The zero-order steady-state equations without the field-aligned currents are even more simple than in the previous chapter:

$$\mathbf{I}_{x,y} = \frac{\mathbf{B}_z}{B_z^2} \times [m(\mathbf{V}_{x,y}\cdot\nabla_{x,y})\mathbf{V}_{x,y} + \nabla_{x,y}\pi] \qquad (4\cdot 1)$$

$$I_x^i = \Sigma_P B_z V_y + \Sigma_H B_z V_x \qquad (4\cdot 2)$$

$$I_y^i = -\Sigma_P B_z V_x + \Sigma_H B_z V_y \qquad (4\cdot 3)$$

$$\mathbf{I}_{x,y}^m = \mathbf{I}_{x,y} - \mathbf{I}_{x,y}^i + \qquad (4\cdot 4)$$

$$\nabla_{x,y}(m\mathbf{V}_{x,y}) = 0 \qquad (4\cdot 5)$$

$$\nabla_{x,y}\cdot\mathbf{I}_{x,y}^i = \nabla_{x,y}\cdot\mathbf{I}_{x,y}$$

$$= 0 \qquad (4\cdot 6)$$

Equation (4·3) provides a relation

$$\nabla_{x,y}(A\mathbf{V}_{x,y}) = m\mathbf{V}_{x,y}\cdot\nabla_{x,y}(\frac{A}{m}) \qquad (4\cdot 3')$$

for an arbitrary function A. The function A can be either the zero-order quantity (e.g., π, m) or the first order quantity (e.g., $\delta\pi$, δm, or δB_z).

To derive the first order equations, it is necessary to make some assumptions for the first order quantities too. We totally neglect T_z terms for simplicity. That

guarantees the consistency of the assumptions of $\pi \propto m^{\gamma}$ and $B_z \propto m$. We also neglect $\delta\xi$, and hence, neglect the temporal change of the mapping points (expressed by (2·29) in section 2–5). Since we concentrate on the internal dynamics of the system rather than the response of complicated external conditions, we assume that the external driving force is constant in time. Therefore, $\delta\mathbf{I}^{m}_{x,y}$ is constant.

With the help of (4·3'), the first order equations are given as

$$m\frac{\partial}{\partial t}\delta\mathbf{V}_{x,y} = -\delta m(\mathbf{V}_{x,y}\cdot\nabla_{x,y})\mathbf{V}_{x,y} - m\delta[(\mathbf{V}_{x,y}\cdot\nabla_{x,y})\mathbf{V}_{x,y}] - \nabla_{x,y}\delta\pi$$
$$+ \delta\mathbf{I}_{x,y}\times\mathbf{B}_z + \mathbf{I}_{x,y}\times\delta\mathbf{B}_z + h\zeta\mu_0\delta J_z\mathbf{I}_{x,y} \qquad (4\cdot 7)$$

$$\delta\mathbf{I}_{x,y} = \delta\mathbf{I}^{i}_{x,y} + \delta\mathbf{I}^{m}_{x,y} \qquad (4\cdot 8)$$

$$\frac{\partial}{\partial t}\delta m = -\nabla_{x,y}(\delta m\mathbf{V}_{x,y}) - \nabla_{x,y}(m\delta\mathbf{V}_{x,y})$$
$$= -m\mathbf{V}_{x,y}\cdot\nabla_{x,y}(\frac{\delta m}{m}) - \nabla_{x,y}(\frac{m}{B_z}B_z\delta\mathbf{V}_{x,y}) \qquad (4\cdot 9)$$

$$\frac{\partial}{\partial t}\delta\pi = -\mathbf{V}_{x,y}\cdot\nabla_{x,y}\delta\pi - \delta\mathbf{V}_{x,y}\cdot\nabla_{x,y}\pi - \gamma\delta\pi\nabla_{x,y}\cdot\mathbf{V}_{x,y} - \gamma\pi\nabla_{x,y}\delta\mathbf{V}_{x,y}$$
$$= -B_z^{\gamma}\mathbf{V}_{x,y}\cdot\nabla_{x,y}(\frac{\delta\pi}{B_z^{\gamma}}) - \delta\mathbf{V}_{x,y}\cdot\nabla_{x,y}\pi - \gamma\pi\nabla_{x,y}\delta\mathbf{V}_{x,y}$$
$$= -B_z^{\gamma}\mathbf{V}_{x,y}\cdot\nabla_{x,y}(\frac{\delta\pi}{B_z^{\gamma}}) - \frac{\gamma\pi}{B_z}\nabla_{x,y}(B_z\delta\mathbf{V}_{x,y}) \qquad (4\cdot 10)$$

$$\frac{\partial}{\partial t}\delta B_z = -\nabla_{x,y}(\delta B_z\mathbf{V}_{x,y}) - \nabla_{x,y}(B_z\delta\mathbf{V}_{x,y})$$
$$= -B_z\mathbf{V}_{x,y}\cdot\nabla_{x,y}(\frac{\delta B_z}{B_z}) - \nabla_{x,y}(B_z\delta\mathbf{V}_{x,y}) \qquad (4\cdot 11)$$

$$\delta\mathbf{I}^{i}_{x,y} = \Sigma_P\nabla_{x,y}\delta\Phi + \delta\Sigma_P B_z\mathbf{V}_{x,y}\times\hat{z}$$
$$+ \Sigma_H\hat{z}\times\nabla_{x,y}\delta\Phi + \delta\Sigma_H B_z\mathbf{V}_{x,y}$$

$$or \qquad = \Sigma_P \nabla_{x,y} \delta\Psi \times \hat{z} + \Sigma_H \nabla_{x,y} \delta\Psi$$

$$+ \delta(\Sigma_P B_z \mathbf{V}_{x,y}) \times \hat{z} + \delta(\Sigma_H B_z \mathbf{V}_{x,y}) \qquad (4 \cdot 12)$$

$$\delta J_z(z=h) = -\nabla_{x,y} \cdot \delta \mathbf{I}^i_{x,y}$$

$$= -\Sigma_P \nabla^2_{x,y} \delta\Phi - \nabla_{x,y}\Sigma_P \cdot \nabla_{x,y}\delta\Phi + [B_z \mathbf{V}_{x,y} \times \nabla_{x,y}\delta\Sigma_P]_z$$

$$+ [\nabla_{x,y}\Sigma_H \times \nabla_{x,y}\delta\Phi]_z - B_z \mathbf{V}_{x,y} \cdot \nabla_{x,y}\delta\Sigma_H \qquad (4 \cdot 13)$$

$$\nabla_{x,y} \cdot \delta \mathbf{I}^m_{x,y} = 0 \qquad (4 \cdot 14)$$

$$\hat{z} \times \nabla_{x,y}\delta\Phi = B_z \delta \mathbf{V}_{x,y} + \mathbf{V}_{x,y}\delta B_z + \nabla_{x,y}\delta\Psi \qquad (4 \cdot 15)$$

$$\nabla^2_{x,y}\delta\Phi = \nabla_{x,y}(B_z \delta \mathbf{V}_{x,y} \times \hat{z} + \mathbf{V}_{x,y}\delta B_z \times \hat{z}) \qquad (4 \cdot 16)$$

$$or \qquad \nabla^2_{x,y}\delta\Psi = -\nabla_{x,y}(B_z \delta \mathbf{V}_{x,y} + \mathbf{V}_{x,y}\delta B_z) \qquad (4 \cdot 17)$$

where $\Sigma_H > 0$. All of ξ_x, ξ_y, and $\delta\Psi$ disappears from the equation for J_z because of $\xi_x = \xi_y$,

The last term of (4·7) is negligible compared to the previous term if

$$\frac{\delta B_z}{\delta B_{x,y}} \gg \frac{h}{L_0}\zeta$$

is satisfied. Since $h \ll L_0$ and $\zeta \sim 10^{-1}$ ($\zeta = 1/5$ for the hyperbolic geomagnetic field in the plasma sheet), the above inequality is normally satisfied unless $\delta B_z = 0$. Therefore, we neglect the last term in (4·7) as an additional assumption.

Since (4·16) and (4·17) are related to $B_z \delta \mathbf{V}_{x,y}$ rather than $\delta \mathbf{V}_{x,y}$ itself, we rewrite (4·7) in terms of $B_z \delta \mathbf{V}_{x,y}$. With the help of the above assumption, (4·7)

becomes

$$\frac{m}{B_z}\frac{\partial}{\partial t}(B_z\delta\mathbf{V}_{x,y}) = (\frac{\delta B_z}{B_z} - \frac{\delta m}{m})m(\mathbf{V}_{x,y}\cdot\nabla_{x,y})\mathbf{V}_{x,y}$$
$$- m(\delta\mathbf{V}_{x,y}\cdot\nabla_{x,y})\mathbf{V}_{x,y} - m(\mathbf{V}_{x,y}\cdot\nabla_{x,y})\delta\mathbf{V}_{x,y}$$
$$- \nabla_{x,y}\delta\pi + \frac{\delta B_z}{B_z}\nabla_{x,y}\pi + B_z\delta\mathbf{I}_{x,y}\times\hat{z} \qquad (4\cdot 18)$$

where

$$\nabla_{x,y}\pi = \frac{\gamma\pi}{B_z}\nabla_{x,y}B_z \qquad (4\cdot 19)$$

All the above equations are used through chapters 4 and 5.

In this chapter, we take $\mathbf{V}_{x,y} = 0$ for the zero order: we study the perturbation from the static equilibrium that we studied in 3–1. The nonzero $\mathbf{V}_{x,y}$ cases are studied in chapter 5. The zero-order equations (4·1) – (4·6) are reduced to

$$\mathbf{I}^m_{x,y} = \frac{1}{B_z}\hat{z}\times\nabla_{x,y}\pi \qquad (4\cdot 20)$$

which corresponds to equation (4·10) of section 3–1. Equation (4·11) of section 3–1 is automatically satisfied because we have assumed $\pi \propto m \propto B_z$.

Before we write down the first order perturbed equations, let us introduce D and R as the divergence and the rotation of $B_z\delta\mathbf{V}_{x,y}$; i.e.,

$$D \equiv \nabla_{x,y}\cdot(B_z\delta\mathbf{V}_{x,y}) \qquad (4\cdot 21)$$

$$R \equiv \nabla_{x,y}\cdot(B_z\delta\mathbf{V}_{x,y}\times\hat{z}) \qquad (4\cdot 22)$$

These quantities are directly related to the potentials $\delta\Phi$ and $\delta\Psi$:

$$\nabla^2_{x,y}\delta\Phi = R \tag{4·23}$$

$$\nabla^2_{x,y}\delta\Psi = -D \tag{4·24}$$

Spatial derivatives of $B_z\delta\mathbf{V}_{x,y}$ can be rewritten through (4·21) and (4·22). The other $B_z\delta\mathbf{V}_{x,y}$ terms can be rewritten through (4·15): Rewriting the linearized perturbed equations (4·8) – (4·18) in terms of D, R, $\delta\Phi$, and $\delta\Psi$ when there is no zero-order convection, we find

$$\begin{aligned}\frac{m}{B_z}\frac{\partial}{\partial t}(B_z\delta\mathbf{V}_{x,y}) &= \frac{m}{B_z}\frac{\partial}{\partial t}(\hat{z}\times\nabla_{x,y}\delta\Phi - \nabla_{x,y}\delta\Psi)\\ &= -\nabla_{x,y}\delta\pi + \frac{\delta B_z}{B_z}\nabla_{x,y}\pi + B_z(\delta\mathbf{I}^i_{x,y} + \delta\mathbf{I}^m_{x,y})\times\hat{z} \qquad (4·25)\end{aligned}$$

$$\frac{\partial}{\partial t}\delta m = -\frac{m}{B_z}D \tag{4·26}$$

$$\frac{\partial}{\partial t}\delta\pi = -\frac{\gamma\pi}{B_z}D \tag{4·27}$$

$$\frac{\partial}{\partial t}\delta B_z = -D \tag{4·28}$$

$$\delta\mathbf{I}^i_{x,y} = \Sigma_P\nabla_{x,y}\delta\Phi - \Sigma_H\nabla_{x,y}\delta\Phi\times\hat{z} \tag{4·29}$$

$$\delta J_z = -\Sigma_P R - \nabla_{x,y}\Sigma_P\cdot\nabla_{x,y}\delta\Phi + [\nabla_{x,y}\Sigma_H\times\nabla_{x,y}\delta\Phi]_z \tag{4·30}$$

$$\delta\mathbf{I}^m_{x,y} = \nabla_{x,y}\delta K^m\times\hat{z} \tag{4·31}$$

where δK^m is the potential for $\delta\mathbf{I}^m_{x,y}$ and constant in time. The existence of such a potential is guaranteed by (4·14). Since δm and δJ_z do not appear in any

other equations, equations (4·26) and (4·30) can be separated from the rest of the equations. By substituting (4·29) and (4·31) into $\delta \mathbf{I}_{x,y}$ in equation (4·25), we have

$$\frac{m}{B_z}\hat{z} \times \frac{\partial}{\partial t}\nabla_{x,y}\delta\Phi + \Sigma_P B_z \hat{z} \times \nabla_{x,y}\delta\Phi - \Sigma_H B_z \nabla_{x,y}\delta\Phi - \frac{m}{B_z}\frac{\partial}{\partial t}\nabla_{x,y}\delta\Psi$$
$$= -\nabla_{x,y}\delta\pi + \frac{\delta B_z}{B_z}\nabla_{x,y}\pi - B_z \nabla_{x,y}\delta\bar{K}^m \qquad (4 \cdot 32)$$

Equations (4·21) - (4·24), (4·27), (4·28), and (4·32) are the governing equations for this chapter. The field-aligned currents are related to the plasma motion through (4·30). Equation (4·32) includes the ionospheric 'drag' force as well as the magnetospheric pressure gradient force and the $\mathbf{J} \times \mathbf{B}$ force. The second term on the left-hand side (with Σ_P) of (4·32) represents the ionospheric drag force with dissipation (Joule heating). The third term represents the ionospheric nondissipative $\mathbf{J} \times \mathbf{B}$ force.

The momentum equation (4·32) can be divided into a rotation-free part and a divergence-free part. Taking the divergence and the rotation of (4·32), we have

$$\frac{m}{B_z}\frac{\partial D}{\partial t} - \Sigma_H B_z R - [\nabla_{x,y}(\Sigma_P B_z) \times \nabla_{x,y}\delta\Phi]_z - \nabla_{x,y}(\Sigma_H B_z)\cdot\nabla_{x,y}\delta\Phi$$
$$= -\nabla^2_{x,y}\delta\pi + \nabla_{x,y}\cdot(\frac{\delta B_z}{B_z}\nabla_{x,y}\pi) - \nabla_{x,y}\cdot(B_z\nabla_{x,y}\delta\bar{K}^m) \qquad (4 \cdot 33)$$
$$\frac{m}{B_z}\frac{\partial R}{\partial t} + \Sigma_P B_z R + \nabla_{x,y}(\Sigma_P B_z)\cdot\nabla_{x,y}\delta\Phi - [\nabla_{x,y}(\Sigma_H B_z) \times \nabla_{x,y}\delta\Phi]_z$$
$$= -[\nabla_{x,y}\pi \times \nabla_{x,y}(\frac{\delta B_z}{B_z})]_z - [\nabla_{x,y}B_z \times \nabla_{x,y}\delta\bar{K}^m]_z \qquad (4 \cdot 34)$$

The ionospheric effects are collected on the left-hand sides. By picking up the first two terms on the left-hand side of (4·34), one notices that the deceleration of R

is caused by the Joule dissipation. In order to delete $\delta\pi$ and δB_z from (4·33) and (4·34), we take the time derivatives of these equations:

$$\frac{\partial^2 D}{\partial t^2} - \frac{\Sigma_H}{\Sigma_P}\frac{1}{\tau_1}\frac{\partial R}{\partial t}$$
$$= \frac{1}{\tau_1}\frac{1}{\Sigma_P B_z}[\nabla_{x,y}(\Sigma_P B_z) \times \frac{\partial}{\partial t}\nabla_{x,y}\delta\Phi]_z + \frac{1}{\tau_1}\frac{1}{\Sigma_P B_z}\nabla_{x,y}(\Sigma_H B_z)\cdot\frac{\partial}{\partial t}\nabla_{x,y}\delta\Phi$$
$$+ \frac{B_z}{m}\nabla^2_{x,y}(\frac{\gamma\pi}{B_z}D) - \frac{B_z}{m}\nabla_{x,y}(\frac{D}{B_z}\nabla_{x,y}\pi) \qquad (4\cdot 35)$$

$$\frac{\partial^2 R}{\partial t^2} + \frac{1}{\tau_1}\frac{\partial R}{\partial t}$$
$$= \frac{1}{\tau_1}\frac{1}{\Sigma_P B_z}[\nabla_{x,y}(\Sigma_H B_z) \times \frac{\partial}{\partial t}\nabla_{x,y}\delta\Phi]_z - \frac{1}{\tau_1}\frac{1}{\Sigma_P B_z}\nabla_{x,y}(\Sigma_P B_z)\cdot\frac{\partial}{\partial t}\nabla_{x,y}\delta\Phi$$
$$+ \frac{B_z}{m}[\nabla_{x,y}\pi \times \nabla_{x,y}(\frac{D}{B_z})]_z \qquad (4\cdot 36)$$

where

$$\tau_1 = \frac{m}{\Sigma_P B_z^2} \qquad (4\cdot 37)$$

is $1 \sim 10$ minute in the plasma sheet.

Equations (4·23), (4·24), (4·35), and (4·36) construct a closed set for D, R, $\delta\Phi$, and $\delta\Psi$. One of the standard methods to solve these equations is Fourier analysis, which is adopted later in section 4–4. Before that, we examine special cases to extract the contribution of each term. Without solving equations (4·35) and (4·36), we may extract two essentially different phenomena: the wave propagation and exponential-type decay. Both phenomena are to be generated simultaneously. A propagating wave is generated when the steep temporal variation makes the

second order time derivative term dominant in the equation. Since the balancing term is $\nabla^2_{x,y}\delta\pi$, the wave is the magnetosonic mode. The other type of solution, the decay, achieves the redistribution of the plasma toward an asymptotic state. Combination of the wave and decay will be found later in the numerical simulation (chapter 6).

In order to make things clear, we neglect the gradient of B_z (and π) and Σ. Equation (4·35) and (4·34) become, respectively,

$$\frac{\partial^2 D}{\partial t^2} - \frac{\Sigma_H}{\Sigma_P}\frac{1}{\tau_1}\frac{\partial R}{\partial t} = \frac{\gamma\pi}{m}\nabla^2_{x,y}D \qquad (4\cdot 38)$$

$$\frac{\partial R}{\partial t} + \frac{R}{\tau_1} = 0 \qquad (4\cdot 39)$$

Without the ionospheric current, these two equations are independent of each other. Equation (4·38) obeys the wave equation if D is larger than R. At the same time, R, which is related to J_z, decays from its initial value according to (4·39). A steady-state solution is obtained by setting $\partial/\partial t = 0$ for the first order quantities. Details for the wave mode, decaying mode, and the steady-state solution are studied in the following sections.

Let us go back to (35) and (36). Equating $\partial R/\partial t$ terms, we have

$$\frac{\partial^2 D}{\partial t^2} + \frac{\Sigma_H}{\Sigma_P}\frac{\partial^2 R}{\partial t^2} - [1 + (\frac{\Sigma_H}{\Sigma_P})^2]\frac{B_z}{m}[\nabla_{x,y}(\Sigma_P B_z) \times \frac{\partial}{\partial t}\nabla_{x,y}\delta\Phi]_z$$
$$= \nabla^2_{x,y}(\frac{\gamma\pi}{m}D) - \nabla_{x,y}(\frac{D}{m}\nabla_{x,y}\pi) + \frac{\Sigma_H}{\Sigma_P}[\nabla_{x,y}\pi \times \nabla_{x,y}(\frac{D}{m})]_z \quad (4\cdot 40)$$

If $D \gg (\Sigma_H/\Sigma_P)R$, we may neglect the R term and the $\delta\Phi$ term; i.e.,

$$\frac{\partial^2 D}{\partial t^2} = \nabla^2_{x,y}(\frac{\gamma\pi}{m}D) - \nabla_{x,y}\cdot(\frac{D}{m}\nabla_{x,y}\pi) + \frac{\Sigma_H}{\Sigma_P}[\nabla_{x,y}\pi \times \nabla_{x,y}(\frac{D}{m})]_z \quad (4\cdot 41)$$

Especially when the zero-order gradient is not very steep ($|\nabla D/D| > |\nabla\pi/\pi|$), this equation is further simplified to

$$\frac{\partial^2 D}{\partial t^2} = \frac{\gamma\pi}{m}\nabla^2_{x,y}D - \frac{1}{m}\nabla_{x,y}\pi\cdot\nabla_{x,y}D + \frac{\Sigma_H}{\Sigma_P}[\frac{1}{m}\nabla_{x,y}\pi \times \nabla_{x,y}D]_z \quad (4\cdot 42)$$

The first term comes from the pressure gradient force, the second term comes from the $\mathbf{I}\times\delta\mathbf{B}$ force, and the third term comes from $\partial R/\partial t$ through the $\delta\mathbf{I}\times\mathbf{B}$ force. This nonzero R is excited by $\mathbf{I}_H \times \delta\mathbf{B}$. Since the effect of the Hall current comes into the system through R, this term is related to field-aligned current generation too.

This equation describes many situations according to which term of the right-hand side is balanced with the left-hand side. The first term causes the wave propagation that will be considered in section 4–4, the second term is considered in section 4–2–2, and the third term in section 4–2–3.

4–1. Steady-State Perturbation from Static Equilibrium

As a simplest case, we give the steady-state ($\partial/\partial t = 0$) perturbation; we study the field-aligned current generation from a maintained perturbed flow. Directly

from (4·26) - (4·28), we have $D = 0$. Equation (4·24) leads $\delta\Psi = 0$ too. Now, equations (4·27) and (4·28) are not related to each other; i.e., $\delta\pi$ and δB_z can be given independently (i.e., arbitrarily). Since δB_z can be included in B_z, we set $\delta B_z = 0$ and hence, $\delta\pi \neq 0$. The momentum equation (4·25) or (4·32) becomes:

$$\begin{aligned} \hat{z} \times \delta\mathbf{I}^i_{x,y} &= (-\Sigma_H + \Sigma_P \hat{z}\times)\nabla_{x,y}\delta\Phi \\ &= -\frac{1}{B_z}\nabla_{x,y}\delta\pi - \nabla_{x,y}\delta K^m \end{aligned} \qquad (4\cdot 43)$$

Operating with $\Sigma_H + \Sigma_P \hat{z}\times$, we have

$$(\Sigma_H^2 + \Sigma_P^2)\nabla_{x,y}\delta\Phi = (\Sigma_H + \Sigma_P \hat{z}\times)(\frac{1}{B_z}\nabla_{x,y}\delta\pi + \nabla_{x,y}\delta K^m) \qquad (4\cdot 43')$$

This equation still holds in $\delta K^m = 0$ cases too. The field-aligned current $\delta J_z = -\nabla_{x,y}\mathbf{I}^i_{x,y}$ is calculated as

$$\delta J_z = [\nabla_{x,y}(\frac{1}{B_z}) \times \nabla_{x,y}\delta\pi]_z \qquad (4\cdot 44)$$

Apparently, the steady-state field-aligned current does not depend on the ionospheric conductivities. Since zero-order velocity is zero, the field-aligned current generation is related only to $\nabla P \times \nabla B$ among many terms in the expression by *Kan* [1987]. This term originally comes from the divergence of the ∇B drift which is expressed as $\mathbf{B} \times \nabla P/B^2$. The solution presented here also satisfies the original first order equations that contain $\partial/\partial t$ terms.

Employing the above solution as the initial values for the time-dependent equations (4·27), (4·28), and (4·32). we find that the time derivatives of $\delta\pi$, δB_z, and $\delta \mathbf{V}_{x,y}$ at $t=0$ are

$$\begin{aligned}
\frac{\partial}{\partial t}\delta\pi|_{t=0} &= -\frac{\gamma\pi}{B_z}D|_{t=0} \\
&\equiv 0 \\
\frac{\partial}{\partial t}\delta B_z|_{t=0} &= -D|_{t=0} \\
&\equiv 0 \\
\frac{\partial}{\partial t}\delta \mathbf{V}_{x,y}|_{t=0} &= B_z[(\Sigma_H - \Sigma_P \hat{z}\times)\nabla_{x,y}\delta\Phi - \frac{1}{B_z}\nabla_{x,y}\delta\pi - \nabla_{x,y}\delta K^m]_{t=0} \\
&\quad + [\frac{\delta B_z}{B_z}\nabla_{x,y}\pi]_{t=0} \\
&\equiv 0
\end{aligned}$$

Therefore, the perturbation does not change for $t > 0$. In other words, once this steady-state is achieved, and if we take $\delta K^m = 0$, the field-aligned currents keep flowing without any external maintenance force.

This result is not consistent with the law of the conservation of energy. Let us consider the energy budget. Since we have $\delta J_z \propto \delta\pi$, there is the energy dissipation related to $\delta\pi$ in the ionosphere, while we have the steady-state solution. Therefore, the initial perturbation of $\delta\pi$ has to decay. This paradox comes from the linear approximation. Since the energy dissipation is the second order quantity (product

of $\delta \mathbf{V}_{x,y}$ and $\delta\pi$), the pressure does not decay. It will be more clear if we retain the second order term only in (4·27):

$$\begin{aligned}\frac{\partial}{\partial t}\delta\pi &= -\frac{\gamma\pi}{B_z}D - \delta\mathbf{V}_{x,y}\cdot\nabla_{x,y}\delta\pi - \gamma\delta\pi\nabla_{x,y}\cdot\delta\mathbf{V}_{x,y} \\ &= -\delta\mathbf{V}_{x,y}\cdot\nabla_{x,y}\delta\pi + \frac{\delta\pi}{\pi}\delta\mathbf{V}_{x,y}\cdot\nabla_{x,y}\pi \\ &= -\delta\mathbf{V}_{x,y}\pi\nabla_{x,y}(\frac{\delta\pi}{\pi}) \qquad (4\cdot 45)\end{aligned}$$

where we used the first order solutions; e.g., $D = 0$, etc.. Since $\delta\mathbf{V}_{x,y}$ is directly related to $\delta\Phi$ through (4·15), it is related to $\delta\mathbf{I}^{i}_{x,y}$ or $\delta\pi$ as (4·43) shows; i.e., the time derivative of $\delta\pi$ is proportional to $(\delta\pi)^2$. A further discussion will follow in section 5–1. In the plasma sheet, the energy dissipation can be supported by internal heating or plasma sheet thinning that maintains the pressure.

4–2. Evolution of Linear Perturbations

In this section, we give an initial perturbation to the static equilibrium and study the change of the initial configuration and the field-aligned current generation. We obtain the relaxation time for this process too. As the asymptotic solution, we may also obtain the steady-state solution caused by the initial and/or a maintained disturbance. Equations (4·33) and (4·34) are still complicated, and they are further simplified.

Since we consider the redistribution process of the initial disturbances, we neglect the external $\mathbf{J} \times \mathbf{B}$ force caused by δK^m. This term causes a different physics from the relaxation of the initial perturbation, and will be studied in section 4–3. Thus, equations (4·33) and (4·34) are simplified to

$$\frac{m}{B_z}\left(\frac{\partial D}{\partial t} - \frac{\Sigma_H}{\Sigma_P}\frac{R}{\tau_1}\right) - \nabla_{x,y}(\Sigma_H B_z)\cdot\nabla_{x,y}\delta\Phi - [\nabla_{x,y}(\Sigma_P B_z)\times\nabla_{x,y}\delta\Phi]_z$$
$$= -\nabla^2_{x,y}\delta\pi + \nabla_{x,y}\left(\frac{\delta B_z}{B_z}\nabla_{x,y}\pi\right) \qquad (4\cdot 46)$$

$$\frac{m}{B_z}\left(\frac{\partial R}{\partial t} + \frac{R}{\tau_1}\right) + \nabla_{x,y}(\Sigma_P B_z)\cdot\nabla_{x,y}\delta\Phi - [\nabla_{x,y}(\Sigma_H B_z)\times\nabla_{x,y}\delta\Phi]_z$$
$$= -[\nabla_{x,y}\pi\times\nabla_{x,y}\left(\frac{\delta B_z}{B_z}\right)]_z \qquad (4\cdot 47)$$

where

$$R = \nabla^2_{x,y}\delta\Phi \qquad (4\cdot 23)$$

$$\frac{\partial}{\partial t}\delta\pi = -\frac{\gamma\pi}{B_z}D \qquad (4\cdot 27)$$

$$\frac{\partial}{\partial t}\delta B_z = -D \qquad (4\cdot 28)$$

$$\tau_1 = \frac{m}{\Sigma_P B_z^2} \qquad (4\cdot 37)$$

We still have too many terms to extract the essential physical mechanism that takes place in the relaxation process. Since, in many works, the gradient of pressure (and hence, B_z) and the gradient of the conductivity are considered important in the field-aligned current generation [e.g., *Kan et al.*, 1988; *Vasyliunas*, 1984; *Jaggi and*

Wolf, 1973], we categorize the situation by the gradient of the zero order $(\Sigma_P B_z)$ or $\Sigma_P \pi$.

Case 1. When $\nabla_{x,y}(\Sigma_P B_z)$ is significant, we may neglect R terms in (4·46). Since (4·47) is the equation for R, we may not neglect both R terms. Here, we assume that the intrinsic scale time τ_1 is short compared to the time scale of the driven term of D. Therefore, we neglect the $\partial R/\partial t$ term instead of the R term in (4·47). Thus, equations (4·46) and (4·47) are simplified as

$$\frac{m}{B_z}\frac{\partial D}{\partial t} - \nabla_{x,y}(\Sigma_H B_z)\cdot\nabla_{x,y}\delta\Phi - [\nabla_{x,y}(\Sigma_P B_z)\times\nabla_{x,y}\delta\Phi]_z$$
$$= -\nabla^2_{x,y}\delta\pi + \nabla_{x,y}\cdot(\frac{\delta B_z}{B_z}\nabla_{x,y}\pi) \qquad (4\cdot 48)$$

$$R + \frac{1}{\Sigma_P B_z}\nabla_{x,y}(\Sigma_P B_z)\cdot\nabla_{x,y}\delta\Phi - \frac{1}{\Sigma_P B_z}[\nabla_{x,y}(\Sigma_H B_z)\times\nabla_{x,y}\delta\Phi]_z$$
$$= -\tau_1[\frac{1}{m}\nabla_{x,y}\pi\times\nabla_{x,y}\delta B_z]_z \qquad (4\cdot 49)$$

These equations can be further simplified according to whether R or D is larger.

Case 2. If $\nabla_{x,y}(\Sigma_P B_z)$ is not so significant, we may drop all the second order $\nabla_{x,y}(\Sigma_P B_z)$ terms from equations (4·46) and (4·47). Since $\delta\Phi$ is another expression of R as of (4·23), and since all $\delta\Phi$ terms in (4·47) are multiplied by $\nabla_{x,y}(\Sigma_P B_z)$, these terms provide only the second order of $\nabla_{x,y}(\Sigma_P B_z)$ in the expression of R. Therefore, we neglect $\delta\Phi$ terms in (4·47):

$$\frac{\partial R}{\partial t} + \frac{R}{\tau_1} = -[\frac{1}{m}\nabla_{x,y}\pi\times\nabla_{x,y}\delta B_z]_z \qquad (4\cdot 50)$$

Let us drop the second order $\nabla_{x,y}B_z$ terms from (4·46). Equation (4·50) states that R, and hence $\delta\Phi$, are the first order quantities in terms of "small" $\nabla_{x,y}(\Sigma_P B_z)$.

Thus, all of the $\delta\Phi$ terms are the second order $\nabla_{x,y}(\Sigma_P B_z)$ terms in (4·46) too, and we neglect them. We have

$$\frac{\partial D}{\partial t} + \frac{B_z}{m}\nabla^2_{x,y}\delta\pi - \nabla_{x,y}(\frac{\delta B_z}{m}\nabla_{x,y}\pi) = \frac{\Sigma_H}{\Sigma_P}\frac{R}{\tau_1} \qquad (4\cdot 51)$$

which corresponds to (4·41). Each equation has a coupling term.

Case 3. If the gradient of B_z is exactly zero, (4·50) and (4·51) are further simplified to

$$\tau_1\frac{\partial R}{\partial t} + R = 0 \qquad (4\cdot 52)$$

$$\frac{\partial D}{\partial t} + \frac{B_z}{m}\nabla^2_{x,y}\delta\pi = \frac{\Sigma_H}{\Sigma_P}\frac{R}{\tau_1} \qquad (4\cdot 53)$$

Equation (4·52) is homogeneous for R, while equation (4·53) has a coupling term with R.

Now, we consider the initial conditions. They are determined in terms of the set of δB_z, D, and R at $t=0$; i.e., $\delta B_{z0}(x,y)$, $D_0(x,y)$, and $R_0(x,y)$. According to equations (4·46) and (4·47), the initial condition of $D_0 = 0$, $R_0 = 0$ and $\delta B_{z0} = 0$ provide $D(t) = R(t) = 0$ for all t as we have shown in section 4–1. If we specially employ (4·52) and (4·53), the initial condition of $R_0 = 0$ provides $R(t) = 0$ for all t.

In subsection 4–2–1, we study the behavior of a shear flow in terms of the behavior of R. Since we are not considering the effect of the gradient of B_z, i.e., $\delta B_{z0} = 0$, and $\delta\pi_0 = 0$, we use (4·52) and (4·53). A pure shear flow is given as

$R_0 \neq 0$, $D_0 = 0$. A nonzero D_0 case is given in 4–2–2, where we study the plasma compression by an enhanced convection. Therefore, equations (4·48) and (4·49) are employed with the initial conditions of $R_0 = 0$ and $\delta B_{z0} = 0$. In subsection 4–2–3, we study the relaxation process of $\nabla P \times \nabla B$ by means of equations (4·50) and (4·51). This initial condition for this case is nonzero δB_{z0} and $D_0 = 0$. As shown later, these conditions require $R_0 \neq 0$ in order to obtain a meaningful solution. These initial conditions are the same as 4–2–1 except δB_{z0}. Thus, we may have different initial conditions. However, once we have equation (4·47), all the solutions for R, and hence for δJ_z, are essentially the same no matter what the initial conditions are: it always decays with the time constant $\tau_1 = m/(\Sigma_P B_z^2)$.

4–2–1. Relaxation of the Shear Flow

First, we study a shear flow and its relaxation process as shown in Figure 4–1. Since we concentrate on the effect of the shear flow, we start with a pure shear flow ($D_0 = 0$) without any perturbation of the magnetic field ($\delta B_{z0} = 0$) or pressure ($\delta \pi_0 = 0$) under uniform B_z (i.e., uniform π). In this simplified situation, the expression for field-aligned current (4·30) is simplified to $\delta J_z = -\Sigma_P R$, and we may employ (4·52) and (4·53) as the governing equations for R and D.

As is demonstrated by equation (4·52), the field-aligned current decays from its initial value to zero. The decay time $\tau_1 = m/(\Sigma_P B_z^2)$ is $1 \sim 10\,\mathrm{min}$. This is

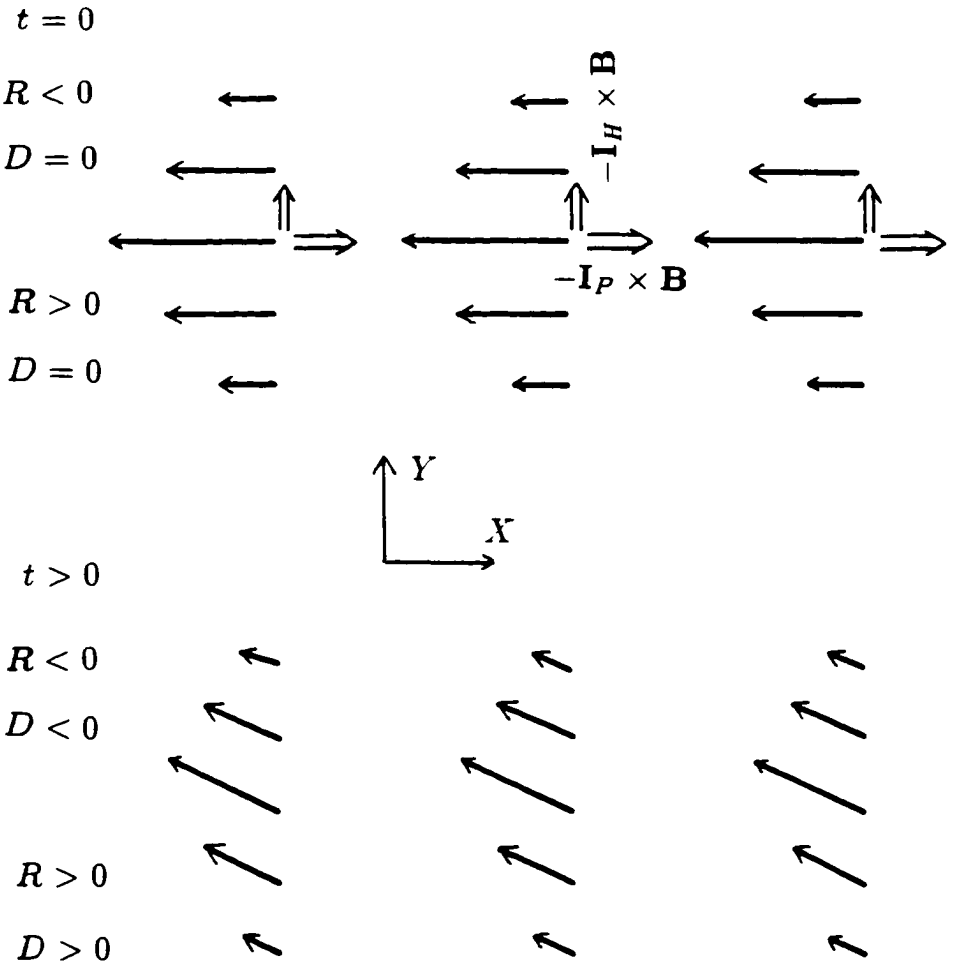

Figure 4–1. Evolution of a shear flow. The perturbed flow (solid arrow) in the x direction given at $t=0$ causes the electric field, and hence, the electric current in the ionosphere. Both the Pedersen and the Hall currents "drag" the ionospheric neutrals by the $\mathbf{I}_P \times \mathbf{B}$ and the $\mathbf{I}_H \times \mathbf{B}$ forces. Their reaction forces (open arrows) are assumed to be transmitted to the plasma sheet, and these forces decelerate and bend the original perturbed flow.

shorter than the time scale of the large-scale field-aligned currents ($\sim$ 1 hour) As one can see from the expression of τ_1 that includes Σ_P, the decay is caused by the ionospheric Joule dissipation. While the equation for R is homogeneous, the equation for D contains R according to (4·53). The governing equation for D is obtained by substituting (4·28) into the time derivative of (4·53).

$$\frac{\partial^2 D}{\partial t^2} - C_S^2 \nabla_{x,y}^2 D = \frac{\Sigma_H}{\Sigma_P} \frac{1}{\tau_1} \frac{\partial R}{\partial t}$$

$$= -\frac{\Sigma_H}{\Sigma_P} \frac{R_0}{\tau_1^2} \exp(-\frac{t}{\tau_1}) \qquad (4 \cdot 54)$$

$$where \qquad C_S^2 = \frac{\gamma \pi}{m} \qquad (4 \cdot 55)$$

Apparently, a propagating wave of D is excited by R. The initial conditions D_0 and $D_1 = \partial D/\partial t|_{t=0}$ for this equation are

$$D_0 = 0$$

$$D_1 = \frac{\Sigma_H}{\Sigma_P \tau_1} R_0$$

D_1 is directly expressed in terms of R_0.

There is no feedback from D to R. This is true as long as (4·52) is valid; i.e., as long as we may neglect the right-hand side of (4·50) compared to the second term of the left-hand side:

$$\frac{R}{\tau_1} \gg \frac{C_S^2 \delta B_z}{L_x L_y}$$

$$or \qquad \frac{R}{D} \gg \frac{C_S^2 \tau_1^2}{L_x L_y} \qquad (4 \cdot 56)$$

where L_x and L_y are the scale length in the x and y directions, respectively. However, once a wave is generated, D can be much larger than R. Let us estimate the duration of how long the $R > D$ condition holds: neglecting the Laplacian term (by giving a wide-spread initial perturbation), we can approximate (4·53) for small D that

$$D \sim \frac{\Sigma_H}{\Sigma_P \tau_1} R_0 t$$

The wave is generated more quickly if the field-aligned current (or R) is very localized. Now the condition (4·56) is rewritten as

$$\exp(-\frac{t}{\tau_1}) \gg \frac{\Sigma_H}{\Sigma_P} \frac{C_S^2 \tau_1 t}{L_x L_y}$$

Unless there is a pre-existing wave or a local and intense field-aligned current, this relation holds longer than $t = \tau_1$. After the wave amplitude grows, equation (4·52) does not hold any more. Thus, we may not obtain the asymptotic state from this equation.

Figure 4–1 illustrates the 1–D situation ($\partial/\partial x = 0$) for small t before the wave mode dominates. Initially, we have a shear flow with $R_0 < 0$ for $0 < y < y_0$ and $R_0 > 0$ for $-y_0 < y < 0$. Since D obeys (4·54) for small t, the plasma is rarefied ($D > 0$) for $y < 0$ and compressed for $y > 0$. Meanwhile, R decays; i.e., the shear is weakened. Imposing $\delta \mathbf{V}_{x,y} = 0$ at $y = \pm y_0$, the flow is determined as shown in Figure 4–1. Deceleration of flow is expressed by the change of R, and hence,

it is caused by the ionospheric Joule dissipation. Thus, we have the 'drag' force which is expressed as $\delta \mathbf{I}^i_{x,y} \times \mathbf{B}_z$ as illustrated by the empty arrow in Figure 4–1. Distortion of the flow is caused by the ionospheric Hall current through the $\mathbf{I}_H \times \mathbf{B}$ force. This force works on the ionospheric plasma, and its reaction works on the plasma sheet. The force is nondissipative; i.e., its direction is perpendicular to the flow. If we have enough $\delta \mathbf{I}^m_{x,y}$ that can cancel these 'drag' forces, the perturbation becomes steady.

If the background plasma is not uniform, e.g., $\partial m/\partial x$ is not zero, the reaction of the $\mathbf{I}_H \times \mathbf{B}$ force causes propagation of the shear. The governing equation for R is obtained from (4·47). For the present purpose, we simply neglect D compared to R for small t (the initial condition is exactly $D_0 = 0$). If the first order quantities depend only on the y, (4·47) becomes

$$\frac{m}{B_z}\left(\frac{\partial R}{\partial t} + \frac{R}{\tau_1}\right) = \frac{\partial}{\partial x}(\Sigma_H B_z)\frac{\partial}{\partial y}\delta\Phi$$

Therefore,

$$\frac{\partial^2 R}{\partial t \partial y} + \frac{1}{\tau_1}\frac{\partial R}{\partial y} = \frac{\Sigma_H}{\Sigma_P}\frac{k_B + k_\Sigma}{\tau_1}R \qquad (4\cdot 57)$$

$$where \qquad k_B = \frac{1}{B_z}\frac{\partial B_z}{\partial x}$$

$$= \frac{1}{C_S^2 m}\frac{\partial \pi}{\partial x} \qquad (4\cdot 58)$$

$$k_\Sigma = \frac{1}{\Sigma_P}\frac{\partial \Sigma_P}{\partial x} \qquad (4\cdot 59)$$

Apparently the solution has to be asymmetric between $+y$ and $-y$.

This situation is illustrated in Figure 4–2. As mentioned above, the ionospheric Hall current causes the 'drag' force in the y direction as shown in the figure. This force has a shear in the x direction because of the change of $\nabla\Sigma_H$ through the change of I_H or because of the change of B_z The convection δV_x caused by this force also has the same shear in the x direction. The sense of the shear is the same as R in the $+y$ direction and opposite in the $-y$ direction. Thus, the shape of R moves toward $\nabla m \times \mathbf{B}$ direction.

4–2–2. Plasma Compression by an Enhanced Flow

Contrary to the previous case, we consider here a compressional flow without shear. Therefore, we set $R_0 = 0$ while we have nonzero D_0. A compressional flow experiences a zero-order pressure gradient. We start with (4·48) and (4·49) under the assumption of $D \gg R$. We neglect $\delta\Phi$ terms compared to δB_z terms because $\delta\Phi$ is related to R while δB_z is related to D.

Since we do not have $\nabla_{x,y}\delta\Phi$ terms, the flow direction does not affect the equation. Therefore, we may take an arbitrary direction for $\nabla_{x,y}B_z$. Let us take the x axis in the $\nabla_{x,y}\pi$ (or $\nabla_{x,y}B_z$) direction as shown in Figure 4–3.

The governing equations for D and R are

$$\frac{\partial D}{\partial t} = -\frac{B_z}{m}\nabla^2_{x,y}\delta\pi + \frac{\partial}{\partial x}\left(\frac{1}{m}\frac{\partial \pi}{\partial x}\delta B_z\right) \qquad (4\cdot 60)$$

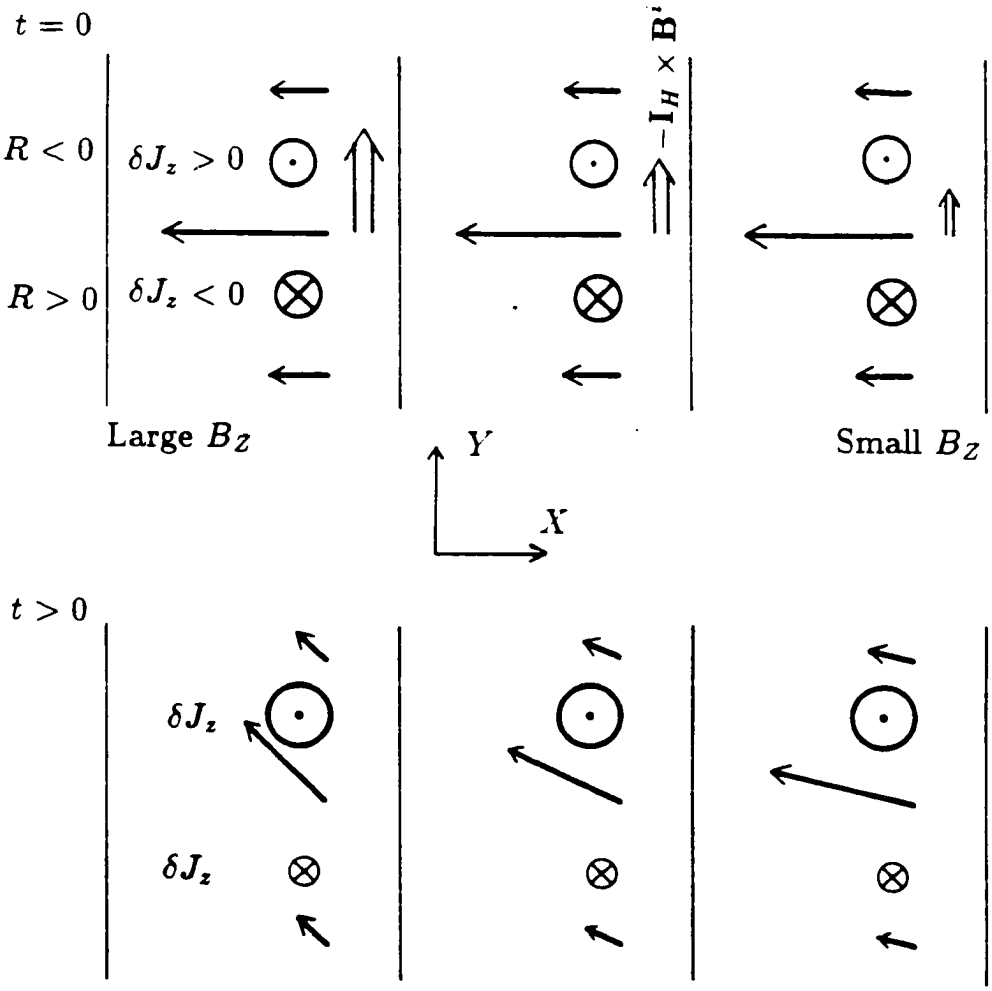

Figure 4–2. Evolution of a shear flow in ∇B_Z. The zero-order gradient of B_z exists in the x direction (same as the flow direction). As illustrated in Figure 4–1, the $-\mathbf{I}_H \times \mathbf{B}$ force bends the flow. This distortion is different in the x direction because B_z is different. Therefore, the field-aligned currents become asymmetric.

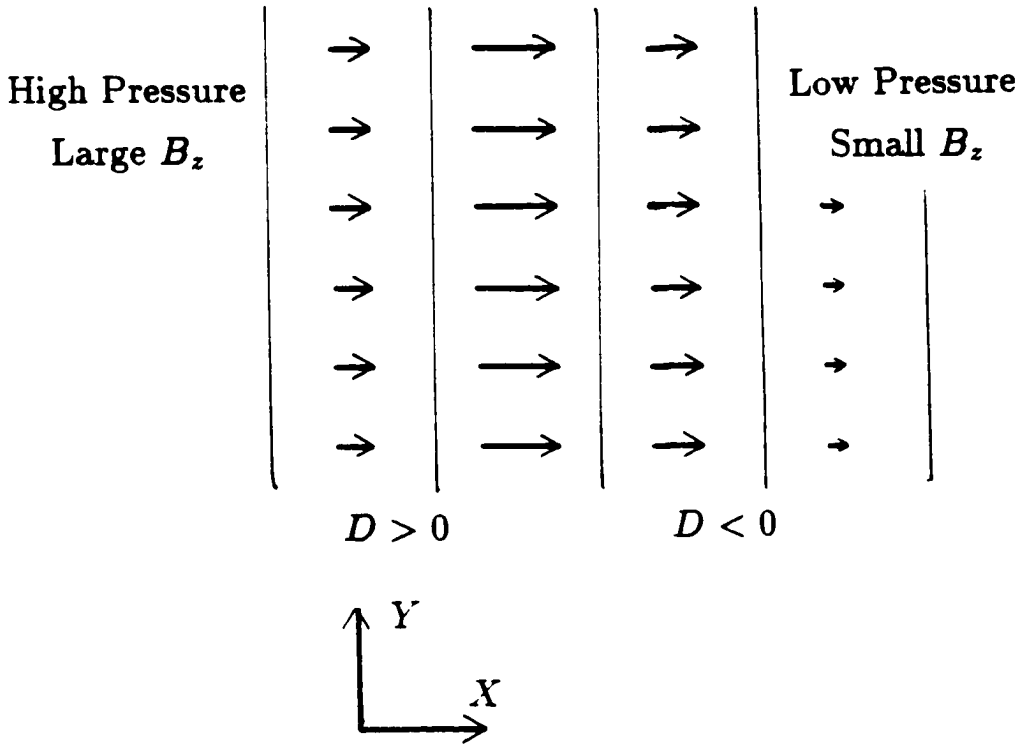

Figure 4–3. A compressible flow. The flow (solid arrow) which experiences the zero-order gradient of B_z in the x direction. If the flow is one dimensional, there is no field-aligned current.

$$\Sigma_P R = -\frac{1}{B_z^2}\frac{\partial \pi}{\partial x}\frac{\partial}{\partial y}\delta B_z \qquad (4\cdot 61)$$

With the help of (4·27) and (4·28), (4·60) determines the behavior of D whereas (4·61) indicates that R is directly determined by D. The first term of the right-hand side of (4·60) represents the pressure gradient force while the second term comes from the $\mathbf{I} \times \mathbf{B}$ force. This force varies as δB_z varies in the x direction. The right-hand side of (4·61) represents the field-aligned current generation by $\nabla P \times \nabla B$ term. This term originally comes from divergence of gradient B drift: $\mathbf{I}_d = \mathbf{B} \times \nabla P / B^2$. The initial condition of $R_0 = 0$ implies $\delta B_{z0} = 0$ through (4·61) and $\partial D/\partial t|_{t=0} = 0$ through (4·60). Note that $R_0 = 0$ means, practically, $R_0 \ll D_0$. Otherwise, we have $\partial/\partial y = 0$ and R is always zero as illustrated in the figure.

Taking the time derivative of (4·60), we have

$$\frac{1}{C_S^2}\frac{\partial^2 D}{\partial t^2} = \nabla_{x,y}^2 D - k_B \frac{\partial D}{\partial x} \qquad (4\cdot 62)$$

where k_B is given as (4·59). Initial conditions are $D_0 \neq 0$ and $D_1 = \partial D/\partial t|_{t=0} = 0$. This equation can be also obtained from (4·42) if we neglect the third term on the right-hand side of it. In order to solve (4·62), we also have to specify the boundary condition at $x = x_0$. The last term comes from the mechanism below. The wave with δV_x (or D) generates the electric field and the ionospheric Pedersen current in the y direction. There is the $\mathbf{I}_P \times \mathbf{B}_z$ force onto the ionospheric plasma. The

reaction force of the $\mathbf{I}_P \times \mathbf{B}_z$ force works in the x direction onto the magnetospheric plasma. Thus, the last term is related to the ionospheric Pedersen conductivity. The details are discussed in section 5–4.

4–2–3. Field-Aligned Currents by $\nabla P \times \nabla B$

If there is a pressure gradient that is not parallel to the gradient of the total magnetic field, the pressure gradient force drives the plasma. This process is initiated from nonzero

$$\nabla P \times \nabla B$$

We study the evolution from this initial configuration with the behavior of the plasma quantities during this process. Since $\nabla_{x,y}\pi \parallel \nabla_{x,y}B_z$ is already given, we need to give $\delta B_{z0} = \delta B_z(t=0)$ such that $\nabla_{x,y}(B_z + \delta B_{z0})$ is not parallel to $\nabla_{x,y}(\pi + \delta\pi_0)$. This condition is achieved if δB_{z0} satisfies

$$\nabla_{x,y}\pi \times \nabla_{x,y}\delta B_{z0} \neq 0$$

when $\delta\pi_0 = 0$. If δB_z is maintained somehow, the situation is exactly the same as 4–1.

We extract the most important mechanism in this process. Therefore, we do not have to take $\nabla_{x,y}\pi$ very large. We start with equations (4·50) and (4·51), rather

than (4·48) and (4·49). Let us take the same coordinate as 4–2–2; i.e., x is lying in the direction of the gradient of B_z (and $\nabla_{x,y}\pi$) as shown in Figure 4–4.

The governing equations for D is

$$\frac{\partial D}{\partial t} + \frac{B_z}{m}\nabla^2_{x,y}\delta\pi - C_S^2 k_B \frac{\partial}{\partial x}\delta B_z = \frac{\Sigma_H}{\Sigma_P}\frac{R}{\tau_1} \qquad (4\cdot 63)$$

where k_B is given as (4·58), δB_z and D are related through equation (4·28). The governing equations for R comes from (4·50). Since equation (4·50) is essentially the decay equation, we approximate it as

$$\frac{R}{\tau_1} = -\eta_r C_S^2 k_B \frac{\partial}{\partial y}\delta B_z \qquad (4\cdot 64)$$

where $0 < \eta_r < 1$. Strictly speaking, η_r is time dependent; however, we take it a constant. For slow phenomena (time scale $> \tau_1$), this is a good approximation because of $\eta_r \ll 1$. Equation (4·64) is the same as (4·61): the field-aligned current is related to $\nabla P \times \nabla B$.

The difference between (4·63) and (4·60) is the R term on the left-hand side. In order to examine the effect of this term on the wave equation, we neglect the third term because it is already studied in the previous subsection:

$$\frac{\partial D}{\partial t} + \frac{B_z}{m}\nabla^2_{x,y}\delta\pi = -C_S^2\frac{\Sigma_H}{\Sigma_P}k_B\frac{\partial}{\partial y}\delta B_z \qquad (4\cdot 65)$$

Without the R term (right-hand side), the equation is symmetric with respect to the y direction because the zero-order configuration is one dimensional. For

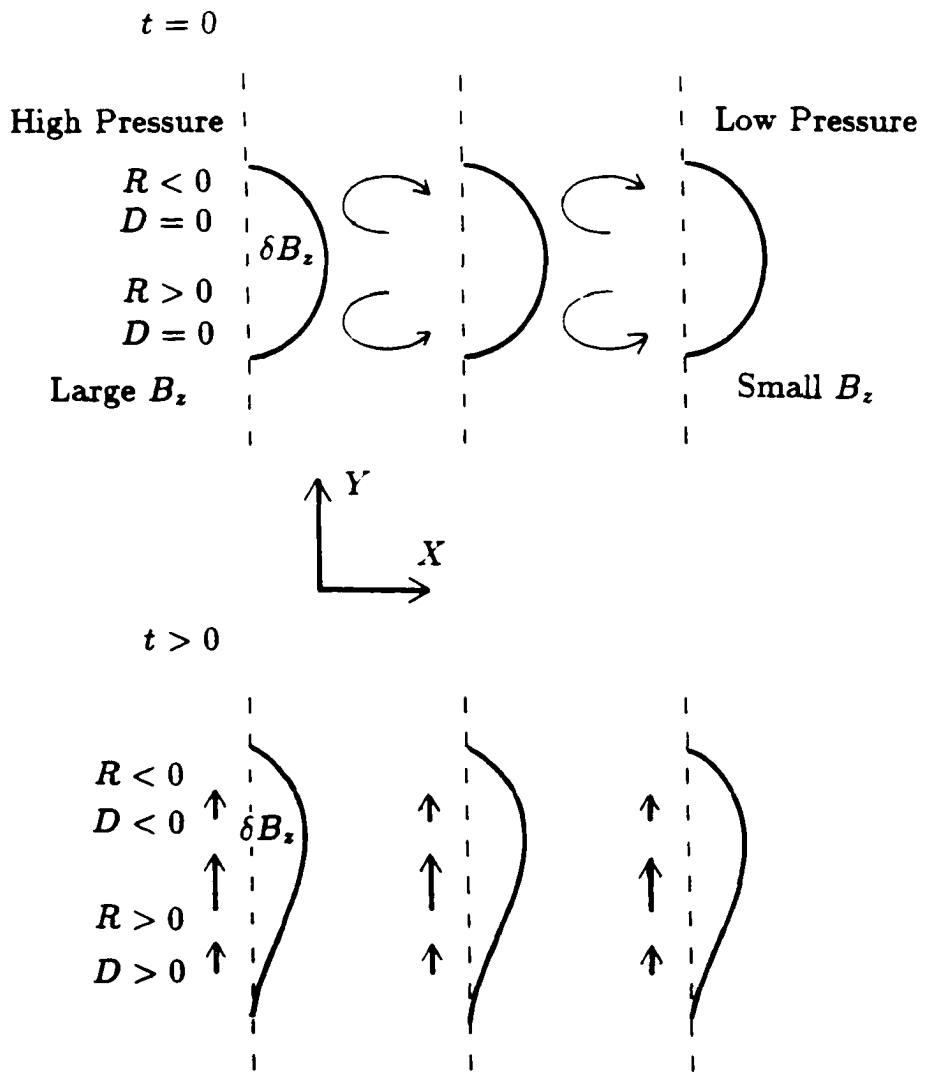

Figure 4–4. Effect of $\nabla P \times \nabla B$. A small bumping of B_z is given in the nonuniform plasma. Zero-order pressure gradient already exists in the x direction. There is the zero-order current due to the zero-order pressure gradient, and that causes $R \neq 0$ convection through $\mathbf{I} \times \delta\mathbf{B}$. We may apply the situation of Figure 4–1 to the convection. There is the $-\mathbf{I}_H \times \mathbf{B}$ force in the y direction. Thus, the distribution of δB_z becomes asymmetric.

example, let us consider a wave propagating in the y direction. The governing equation for this wave is given by taking the time derivative of (4·65):

$$\frac{1}{C_S^2}\frac{\partial^2 D}{\partial t^2} = \nabla_{x,y}^2 D + \frac{\Sigma_H}{\Sigma_P} k_B \frac{\partial D}{\partial y} \qquad (4 \cdot 66)$$

Note that this equation can be obtained from (4·42) too by neglecting the second term on the right-hand side of it. Without the R term (k_B term), the pressure gradient force, i.e., the restore force to the perturbations (e.g., plasma motion) of this wave mode, is symmetric for $\pm y$ directions. Now, we have nonzero R, which is originally driven by the $\mathbf{I} \times \delta\mathbf{B}_z$ ($I_y \delta B_z$) force in the x direction. The R term in (4·66) represents the reaction force of the $\mathbf{I}_H \times \mathbf{B}$ force on the ionospheric plasma. It works in the y direction. That means it reduces or increases the restore force accordingly to the propagation direction. This asymmetry is expressed by the y derivative, and will be further studied in 5–4. In both (4·63) and (4·64), we do not have the ionospheric Joule dissipation associated with the energy dissipation. It has the order of magnitude of δ^2 as is demonstrated in (4·45).

Let us specify the initial conditions. We only specify $\delta B_{z0} \neq 0$ as the initial condition, so that we can extract the phenomenon of the redistribution of $\nabla P \times \nabla B$. This condition provides nonzero R_0 through (4·64) and nonzero $D_1 = \partial D/\partial t|_{t=0}$ through (4·65):

$$D_1 = -C_S^2 \frac{\Sigma_H}{\Sigma_P} k_B \frac{\partial}{\partial y} \delta B_{z0}$$

The other independent initial condition, D_0, is set zero in this case. If we specify $\delta\pi_0 \neq 0$ instead of δB_{z0}, only the initial conditions are different: $D_0 = R_0 = 0$ and $D_1 = -(B_z/m)\nabla^2_{x,y}\delta\pi$. Equations (4·65) or (4·66) do not change in this case. We also need the boundary condition for D at some reference point $y = y_0$, e.g., $D(y = \pm\infty) = 0$.

Figure 4–4 illustrates the effect of the last term of (4·66). As an example, $\delta B_{z0} > 0$ is added around $y = 0$ while $D_0 = 0$. In this coordinate, k_B is negative. Equation (4·64) gives $R_0 < 0$ for $y > 0$ and $R_0 > 0$ for $y < 0$. The vortices corresponding to R_0 are indicated with the arrows. According to (4·63), D has the same sign as R_0 for small t. That means $\partial(\delta V_y)/\partial y < 0$ for $y > 0$ and $\partial(\delta V_y)/\partial y > 0$ for $y < 0$. If we set $\delta V_y(\pm y_0) = 0$ as the boundary condition, the y component convection should be like the heavy arrows in the figure. The behavior of δB_z is determined by (4·28). It increases for $y > 0$ and decreases for $y < 0$. This result is consistent with the above physical explanation in terms of the reaction force of the $\mathbf{I}_H \times \mathbf{B}$ force.

4–3. Enhancement of the Magnetospheric $\mathbf{J} \times \mathbf{B}$ Force

Contrary to the previous section, we set $\delta K^m \neq 0$, and we set the other initial perturbations to be zero. These initial conditions may provide another relaxation process. The basic equations are (4·33) for D and (4·34) for R. Since we consider

the redistribution process caused by the additional $\mathbf{I}^m_{x,y}$ (expressed by δK^m), the $\nabla_{x,y}B_z$ (or $\nabla_{x,y}\pi$) term is assumed to be small. We also neglect the $\partial R/\partial t$ term in (4·34) as this term might simply cause the delay of the response of R to the external (e.g., D or δK^m) change. In other words, we are looking at the redistribution process whose time scale is longer than $\tau_1 = m/(\Sigma_P B_z^2)$. The case with shorter scale time is studied in the next section. Under these assumptions, we may neglect all $\nabla_{x,y}\pi$ terms from (4·33) while we may not for (4·34):

$$m\frac{\partial D}{\partial t} - \Sigma_H B_z^2 R = -B_z \nabla^2_{x,y}\delta\pi - B_z^2 \nabla^2_{x,y}\delta K^m \qquad (4\cdot 67)$$

$$\Sigma_P B_z R = -\frac{1}{B_z}[\nabla_{x,y}\pi \times \nabla_{x,y}\delta B_z]_z - [\nabla_{x,y}B_z \times \nabla_{x,y}\delta K^m]_z \qquad (4\cdot 68)$$

where $\delta\pi$ and δB_z π are related to D through (4·27) and (4·28), respectively. Equation (4·67) states that the wave of D is excited by δK^m and R. We do not have to retain $\nabla_{x,y}\pi$ terms at all in this equation. Equation (4·68) states that R is essentially determined by δK^m and is modulated by δB_z. Both source terms of (4·68) are multiplied by $\nabla_{x,y}\pi$ ($\propto \nabla_{x,y}B_z$ through (4·19)). These terms originally come from the change of the magnetospheric $\mathbf{J}\times\mathbf{B}$ force (change of $\mathbf{I}^m_{x,y}$ and change of B_z). Since R is proportional to $\nabla_{x,y}\pi$, we may neglect the R term from (4·67):

$$\frac{\partial D}{\partial t} + \frac{B_z}{m}\nabla^2_{x,y}\delta\pi = -\frac{B_z^2}{m}\nabla^2_{x,y}\delta K^m \qquad (4\cdot 69)$$

Taking the time derivative, we obtain a wave equation

$$\frac{\partial^2 D}{\partial t^2} - C_S^2 \nabla^2_{x,y} D = 0 \qquad (4\cdot 70)$$

This wave equation is the same as (4·42) if we retain only the first term on the right-hand side of (4·42). The detail of the wave mode is further studied in 4–4. The initial conditions are $D_0 = 0$ and

$$D_1 = -\frac{B_z^2}{m}\nabla_{x,y}^2 \delta K^m$$

Once the solution of D is obtained in terms of δK^m, we may also express R in terms of δK^m through (4·68). Let us take x in the direction of the gradient of π. Equation (4·68) becomes

$$R = \tau_1 C_S^2 k_B \int_0^t \frac{\partial D}{\partial y} dt - \frac{1}{\Sigma_P B_z}\frac{\partial B_z}{\partial x}\frac{\partial}{\partial y}\delta K^m \qquad (4\cdot 71)$$

$$where \qquad k_B = \frac{1}{C_S^2 m}\frac{\partial \pi}{\partial x} \qquad (4\cdot 58)$$

Since D is linear in δK^m, R is also linear in δK^m. The field-aligned current is obtained from equation (4·30); i.e., $\delta J_z \sim -\Sigma_P R$. The initial value of the field-aligned current at $t=0$ is

$$\delta J_{z0} = \frac{1}{B_z}\frac{\partial B_z}{\partial x}\frac{\partial}{\partial y}\delta K^m$$

The effect of δK^m appears only as the initial conditions for D and R. If δK^m does not depend on y, D does not depend on y either. This causes $R = 0$; i.e., no field-aligned current. Since the y derivative of δK^m is δI_x^m, we may conclude that the field-aligned current is caused by $\delta \mathbf{I}^m \cdot \nabla \pi$.

The asymptotic state is given by neglecting $\partial/\partial t$ terms in (4·67) and (4·68):

$$\nabla_{x,y}\delta\pi = -B_z\nabla_{x,y}\delta K^m$$

$$D = 0$$

$$\frac{m}{B_z}C_S^2\delta B_z - \delta\pi = \frac{m}{B_z}C_S^2\delta B_{z0} - \delta\pi_0$$

$$= 0$$

$$\Sigma_P B_z^2 R = -[\nabla_{x,y}B_z \times \nabla_{x,y}\delta\pi]_z - B_z[\nabla_{x,y}B_z \times \nabla_{x,y}\delta K^m]_z$$

$$= 0$$

The pressure is redistributed such that there is no field-aligned current.

4–4. Wave Modes

As we have mentioned in the previous subsections, there are two (forward and backward) propagating waves associated with the change of D as shown in 4–2–4, and 4–3. The characteristic propagation velocity of this mode is C_S. This mode is obtained by setting $R = 0$ under uniform zero-order configuration. Even though this wave mode is not directly associated with the field-aligned current generation, it still affects the field-aligned current through the coupling between D and R through the ionospheric $\mathbf{J} \times \mathbf{B}$ force. There is another mode; namely the $R \neq 0$ mode, that is directly related to the field-aligned current generation. As is shown in 4–2–1, this mode does not propagate but decays with the time constant

of τ_1 because of the ionospheric Joule dissipation. Both $R = 0$ and $R \neq 0$ modes were already mentioned in the previous sections.

In this section, these wave modes are compared with the ordinary MHD waves in $(\omega, \mathbf{k})$ space. For this purpose, we start with a uniform zero-order configuration which is described by equations (4·38) and (4·39). In the plane wave approximation, i.e., $D, R \propto \exp[i\mathbf{k}\cdot\mathbf{x} - i\omega t]$, these equations are rewritten as

$$-\omega^2 D + i\frac{\Sigma_H}{\Sigma_P}\frac{1}{\tau_1}\omega R = -C_S^2 k^2 D \qquad (4 \cdot 72)$$

$$(-i\omega + \frac{1}{\tau_1})R = 0 \qquad (4 \cdot 73)$$

There are three solutions for ω. One corresponds to the $R \neq 0$ mode. The others correspond to the $R = 0$ mode. If we take $R = 0$ in (4·72) or $R \neq 0$ in (4·73), we obtain $\omega = \pm C_S k$ for the $R = 0$ mode, and $\omega = -i/\tau_1$ for the $R \neq 0$ mode. These results are the same as in previous sections. For the $R \neq 0$ mode, we also have

$$(C_S^2 k^2 \tau_1^2 + 1)D = -\frac{\Sigma_H}{\Sigma_P}R \qquad (4 \cdot 74)$$

This relation corresponds to (4·54) in 4–2–1.

Originally, there were five equations with a time derivative. However, equations (4·26) – (4·28) provide two of the $\omega = 0$ modes:

$$\delta\pi - C_S^2 \delta m = const$$

$$\delta B_z - \frac{B_z}{m}\delta m = const$$

Therefore, only three modes remain. The effect of the ionosphere comes into the system through τ_1 and Σ. The ionospheric effect can be eliminated if we set $\Sigma_H = 0$ and $\tau_1 = \infty$. In this case, the $R \neq 0$ mode does not decay, while the $R = 0$ mode is not affected by these parameters.

Let us compare these solutions with the ordinary MHD equations. The dispersion relation for a nondissipative uniform MHD fluid (cf. *Jackson* [1975] chap. 10) is

$$\omega^2 \delta \mathbf{V}_{x,y} = C_S^2 (\mathbf{k} \cdot \delta \mathbf{V}) \mathbf{k}_{x,y} + V_A^2 (\mathbf{k}_{x,y} \cdot \delta \mathbf{V}_{x,y}) \mathbf{k}_{x,y} + V_A^2 k_z^2 \delta \mathbf{V}_{x,y} \quad (4 \cdot 75)$$

$$\omega^2 \delta V_z = C_S^2 k_z (\mathbf{k} \cdot \delta \mathbf{V}) \quad (4 \cdot 76)$$

The above equations can be rewritten in terms of $D = i\mathbf{k}_{x,y} \cdot \delta \mathbf{V}_{x,y}$, and $R = i\mathbf{k}_{x,y} \times \delta \mathbf{V}_{x,y}$. Operating on equation (4·75) with $\mathbf{k}_{x,y}$ and $\mathbf{k}_{x,y}\times$, we have

$$\omega^2 D = (C_S^2 + V_A^2) k_{x,y}^2 D + C_S^2 k_{x,y}^2 (i k_z \delta V_z) + V_A^2 D k_z^2 \quad (4 \cdot 77)$$

$$\omega^2 R = V_A^2 k_z^2 R \quad (4 \cdot 78)$$

while equation (4·76) can be rewritten directly as

$$(\omega^2 - C_S^2 k_z^2)(i k_z \delta V_z) = C_S^2 k_z^2 D \quad (4 \cdot 79)$$

Equations (4·77) and (4·79) determine the $D \neq 0$ mode (i.e., the $R = 0$ mode) waves. The present height-integrated situation corresponds to a limit of $\delta V_z = 0$ and $k_z = 0$. In this case, equation (4·77) is the same as (4·72) except that the

magnetic tension force term (V_A term) disappears from (4·72) and the ionospheric $\mathbf{J} \times \mathbf{B}$ term (R term) comes into (4·72) instead. Thus, the $R = 0$ mode of (4·72) - (4·73) corresponds to the $R = 0$ mode of the ordinary MHD.

Let us identify this mode. By eliminating δV_z terms from (4·77) and (4·79), and imposing $D \neq 0$, we have

$$\omega^4 - \omega^2 k^2 (C_S^2 + V_A^2) + k^2 k_z^2 C_S^2 V_A^2 = 0 \qquad (4 \cdot 80)$$

These are two modes: the MHD fast wave mode and the MHD slow mode. Equation (4·72) contains only one mode. Since the slow mode propagates along the magnetic field, it disappears on the $k_z = 0$ condition of (4·72). Therefore, the $R = 0$ solution of (4·72) is the MHD fast mode. The phase velocity ω/k of the $R = 0$ mode of (4·72) is C_S, while it is $\sqrt{C_S^2 + V_A^2}$ for the MHD fast mode. Again, the magnetic pressure disappears in our model.

The magnetic pressure force originally comes from the $\mathbf{J} \times \mathbf{B}$ force. It appears being accompanied by Σ (and hence, $1/\tau_1$ in (4·72) and (4·73)). For the $R = 0$ mode, this force is multiplied by $\nabla_{x,y} B_z$. Since we neglect $\nabla_{x,y} B_z$ terms in (4·72), we do not have a V_A term.

Next, we examine the $R \neq 0$ mode. This mode comes from equation (4·78), which corresponds to (4·73). Its dispersion relation is

$$\omega^2 - V_A^2 k_z^2 = 0 \qquad (4 \cdot 81)$$

This is the Alfvén mode and corresponds to the decay solution of (4·73). In an uniform MHD medium, the Alfvén wave propagates along the magnetic field lines. The height integrated plasma sheet lies perpendicular to the zero-order magnetic field. Therefore, we do not have the propagating wave mode in (4·73). The Alfvén wave propagates all the way through the magnetic field between the plasma sheet and the ionosphere with zero transition time. The ionospheric dissipation is also transmitted to the ionosphere immediately. A dissipation term comes into (4·73) as the result of the ionospheric Joule heating. This effect introduces the resistivity in the uniform MHD. The Alfvén mode dispersion relation in the resistive MHD equation (cf. *Alfven and Falthammar* [1963]) is

$$\omega^2 - (V_A^2 + i\frac{\omega}{\mu_0\sigma})k_z^2 = 0 \qquad (4 \cdot 82)$$

The diffusion length (skin depth) of this mode is $2\mu_0\sigma V_A^3/\omega^2$, and the decay time of the propagating wave is given as $1/\omega \sim 2\sigma B_z^2/\rho\omega^2$. Therefore, it is expressed as $1/\omega \sim \rho/2\sigma B_z^2$. Apparently, this expression corresponds to τ_1 except for the difference by a factor of L_0/h_0 which appeared in section 2.

Next, we include a small gradient of B_z (or π). Again, we employ the plane wave approximation; i.e., $D, R \propto \exp[i\mathbf{k}\cdot\mathbf{x} - i\omega t]$. "Small" means its scale length is longer than the wave length; i.e., $k \gg \nabla\pi/\pi$. This assumption also enables us to approximate $\nabla_{x,y}(B_z D) = B_z \nabla_{x,y} D$, etc.. We also neglect δK^m terms because the wave mode is determined by the homogeneous part of the equations. The

basic equations are given in (4·35) and (4·36). Let us take the x in the direction of gradient of (B_z, π, m). They are rewritten as:

$$\frac{\partial^2 D}{\partial t^2} - \frac{\Sigma_H}{\Sigma_P}\frac{1}{\tau_1}\frac{\partial R}{\partial t} - \frac{1}{\Sigma_P B_z}\frac{\partial(\Sigma_P B_z)}{\partial x}\frac{1}{\tau_1}\frac{\partial}{\partial t}[\frac{\partial}{\partial y}\delta\Phi + \frac{\Sigma_H}{\Sigma_P}\frac{\partial}{\partial x}\delta\Phi]$$
$$= C_S^2\nabla_{x,y}^2 D - \frac{1}{m}\frac{\partial \pi}{\partial x}\frac{\partial D}{\partial x} \qquad (4\cdot 83)$$

$$\frac{\partial^2 R}{\partial t^2} + \frac{1}{\tau_1}\frac{\partial R}{\partial t} + \frac{1}{\Sigma_P B_z}\frac{\partial(\Sigma_P B_z)}{\partial x}\frac{1}{\tau_1}\frac{\partial}{\partial t}[\frac{\partial}{\partial x}\delta\Phi - \frac{\Sigma_H}{\Sigma_P}\frac{\partial}{\partial y}\delta\Phi]$$
$$= \frac{1}{m}\frac{\partial \pi}{\partial x}\frac{\partial D}{\partial y} \qquad (4\cdot 84)$$

where $\delta\Phi$ is related to R through (4·23); i.e., $R = -k^2\delta\Phi$ in $(\omega, \mathbf{k})$ space. Therefore, $(\omega, \mathbf{k})$ space expressions of the above equations are

$$-\omega^2 D + i\frac{\Sigma_H}{\Sigma_P}\frac{\omega}{\tau_1}R + (k_B + k_\Sigma)\frac{\omega}{\tau_1}(k_y + \frac{\Sigma_H}{\Sigma_P}k_x)\frac{R}{k^2} = -C_S^2(k^2 D + ik_B k_x D)$$
$$-\omega^2 R - i\frac{1}{\tau_1}\omega R - (k_B + k_\Sigma)\frac{\omega}{\tau_1}(k_x - \frac{\Sigma_H}{\Sigma_P}k_y)\frac{R}{k^2} = iC_S^2 k_B k_y D$$

or

$$[\omega^2 - C_S^2(k^2 + ik_B k_x)]D = [i\frac{\Sigma_H}{\Sigma_P} + (k_y + \frac{\Sigma_H}{\Sigma_P}k_x)\frac{k_B + k_\Sigma}{k^2}]\frac{\omega}{\tau_1}R$$
$$[(\omega^2 + i\frac{\omega}{\tau_1}) + (k_x - \frac{\Sigma_H}{\Sigma_P}k_y)\frac{k_B + k_\Sigma}{k^2}\frac{\omega}{\tau_1}]R = -iC_S^2 k_B k_y D$$

where $1/k_B$ and $1/k_\Sigma$ are the scale lengths of the gradients of B_z (or m) and Σ_P as is given in (4·58) and (4·59), respectively. The above equations are equivalent to (4·72) and (4·73) when $k_B = k_\Sigma = 0$. Here, R and D cannot be separated since both equations have the coupling term.

The dispersion relation is

$$
\begin{aligned}
&[\omega^2 - C_S^2(k^2 + ik_B k_x)]\cdot(\omega^2 + i\frac{\omega}{\tau_1}) + (k_x - \frac{\Sigma_H}{\Sigma_P}k_y)\frac{k_B + k_\Sigma}{k^2}\frac{\omega^3}{\tau_1} \\
&- C_S^2\frac{\omega}{\tau_1}[(k_B + k_\Sigma)k_x - \frac{\Sigma_H}{\Sigma_P}k_\Sigma k_y] \\
&= iC_S^2 k_B\frac{\omega}{\tau_1}\frac{k_B + k_\Sigma}{k^2}[k_x(k_x - \frac{\Sigma_H}{\Sigma_P}k_y) - k_y(k_y + \frac{\Sigma_H}{\Sigma_P}k_x)]
\end{aligned}
$$

Apparently $\omega = 0$ is one solution, which is previously mentioned. The right-hand side is the second order term for k_B and k_Σ; i.e., it is proportional to $(\partial\pi/\partial x)^2$. We neglect this term because we assume that the gradient of π is small, Thus, the dispersion relation for the $\omega \neq 0$ mode is

$$
\begin{aligned}
&[\omega^2 - C_S^2(k^2 + ik_B k_x)]\cdot(\omega\tau_1 + i) \\
&= (C_S^2 - \frac{\omega^2}{k^2})(k_B + k_\Sigma)k_x + \frac{\Sigma_H}{\Sigma_P}[\frac{\omega^2}{k^2}(k_B + k_\Sigma) - C_S^2 k_\Sigma]k_y \qquad (4\cdot 85)
\end{aligned}
$$

Let us examine the modification of the $R = 0$ and the $R \neq 0$ modes by nonzero k_B or k_Σ. We adopt a perturbation method for ω; i.e., we keep the first order terms in k_Σ or k_B.

For the MHD fast ($R \neq 0$) mode, we have

$$
\begin{aligned}
\omega^2 - C_S^2(k^2 + ik_B k_x) &= \frac{1}{\omega\tau_1 + i}(C_S^2 - \frac{\omega^2}{k^2})(k_B + k_\Sigma)k_x|_{\omega = C_S k} \\
&\quad + \frac{1}{\omega\tau_1 + i}\frac{\Sigma_H}{\Sigma_P}[\frac{\omega^2}{k^2}(k_B + k_\Sigma) - C_S^2 k_\Sigma]k_y|_{\omega = C_S k} \\
&= \frac{1}{C_S k\tau_1 + i}C_S^2\frac{\Sigma_H}{\Sigma_P}k_B k_y
\end{aligned}
$$

or retaining up to the first order terms of k_B or k_Σ for both imaginary part and the real part,

$$\omega^2 = C_S^2 k^2 [1 + i\frac{k_B k_x}{k^2} - i\frac{\Sigma_H}{\Sigma_P}\frac{1}{C_S^2 k^2 \tau_1^2 + 1}\frac{k_B k_y}{k^2} + \frac{\Sigma_H}{\Sigma_P}\frac{C_S k \tau_1}{C_S^2 k^2 \tau_1^2 + 1}\frac{k_B k_y}{k^2} \qquad (4 \cdot 86)$$

Since an imaginary part is added, either the forward or the backward propagating wave diverges. This result is consistent with 4–2–4. For the Alfvén ($R = 0$) mode,

$$\begin{aligned}\omega\tau_1 + i &= \frac{1}{\omega^2 - C_S^2(k^2 + ik_B k_x)}(C_S^2 - \frac{\omega^2}{k^2})(k_B + k_\Sigma)k_x|_{\omega=-i/\tau_1} \\ &+ \frac{1}{\omega^2 - C_S^2(k^2 + ik_B k_x)}\frac{\Sigma_H}{\Sigma_P}[\frac{\omega^2}{k^2}(k_B + k_\Sigma) - C_S^2 k_\Sigma]k_y|_{\omega=-i/\tau_1} \\ &= \frac{1}{+\tau_1^2 C_S^2(k^2 + ik_B k_x)} \cdot \\ &- (\tau_1^2 C_S^2 + \frac{1}{k^2})(k_B + k_\Sigma)k_x + \frac{\Sigma_H}{\Sigma_P}[\frac{1}{k^2}(k_B + k_\Sigma) + \tau_1^2 C_S^2 k_\Sigma]k_y\end{aligned}$$

or, neglecting the second order terms in k_B or k_Σ,

$$\omega = -\frac{i}{\tau_1}[1 + i\frac{(k_B + k_\Sigma)k_x}{k^2} - i\frac{\Sigma_H}{\Sigma_P}(\frac{k_\Sigma k_y}{k^2} + \frac{1}{C_S^2 k^2 \tau_1^2 + 1}\frac{k_B k_y}{k^2})] \qquad (4 \cdot 87)$$

Thus, this mode begins to propagate because it has a real part. The mechanism of this propagation is already mentioned in 4–2–1. Note that the main correction terms (the terms inside the parenthesis) have the same form in both (4·86) and (4·87). This correction is larger as k is smaller, i.e., for longer wave length.

CHAPTER 5. LINEAR ANALYSIS OF THE FIELD-ALIGNED CURRENT: 2

— PERTURBATIONS FROM STEADY-STATE FLOWS —

We apply the linear analysis to a steady-state flow instead of to a static equilibrium. The assumptions and the basic equations are already given in chapter 4. Here, we further assume uniform zero-order conductivities. We also neglect $\delta \mathbf{I}^m_{x,y}$ terms. These terms are already assumed constant in chapter 4.

For the zero-order equations, the assumptions are the same as those in chapter 4. As an additional assumption, we assume uniform conductivity. *1.* $\partial/\partial t = 0$; *2.* $T_z = 0$; *3.* $\Sigma_P \propto \Sigma_H = uniform$; *4.* $\xi_x = \xi_y = \sqrt{B_z/B_i}$; *5.* $J_z = 0$; *6.* $\pi \propto m^\gamma$; and *7.* $B_z \propto m$. The zero-order equations are the same as (4·1) – (4·6). Because the conductivity is uniform, the $\nabla_{x,y} \mathbf{I}^i_{x,y} = 0$ condition gives $\nabla_{x,y}(B_z \mathbf{V}_{x,y} \times \hat{z}) = 0$. Thus, the zero-order equations are,

$$m(\mathbf{V}_{x,y} \cdot \nabla_{x,y})\mathbf{V}_{x,y} = -\nabla_{x,y}\pi + B_z \mathbf{I}_{x,y} \times \hat{z} \qquad (5 \cdot 1)$$

$$\nabla_{x,y}(B_z \mathbf{V}_{x,y} \times \hat{z}) = 0 \qquad (5 \cdot 2)$$

$$\nabla_{x,y}(B_z \mathbf{V}_{x,y}) = 0 \qquad (5 \cdot 3)$$

$$\mathbf{I}^i_{x,y} = \Sigma_P B_z \mathbf{V}_{x,y} \times \hat{z} + \Sigma_H B_z \mathbf{V}_{x,y} \qquad (5 \cdot 4)$$

$$\nabla_{x,y}(\mathbf{I}_{x,y} - \mathbf{I}^i_{x,y}) = 0 \qquad (5 \cdot 5)$$

The assumptions for the first order equations are: *1.* $\delta B_z / \delta B_{x,y} \gg \zeta h / L_0$; *2.* T_z terms are totally neglected; *3.* the temporal change of the mapping points is

neglected (i.e., $\delta\xi = 0$); and 4. $\delta\mathbf{I}^m_{x,y}$ is neglected. The first three assumptions are the same as in chapter 4. The first order equations are:

$$m\frac{\partial}{\partial t}\delta\mathbf{V}_{x,y} = -\delta m(\mathbf{V}_{x,y}\cdot\nabla_{x,y})\mathbf{V}_{x,y} - m(\delta\mathbf{V}_{x,y}\cdot\nabla_{x,y})\mathbf{V}_{x,y} - m(\mathbf{V}_{x,y}\cdot\nabla_{x,y})\delta\mathbf{V}_{x,y}$$
$$- \nabla_{x,y}\delta\pi + \mathbf{I}_{x,y}\times\hat{z}\delta B_z + B_z\delta\mathbf{I}^i_{x,y}\times\hat{z} \qquad (5\cdot 6)$$

$$\frac{\partial}{\partial t}\delta m = -m\mathbf{V}_{x,y}\cdot\nabla_{x,y}(\frac{\delta m}{m}) - \frac{m}{B_z}D \qquad (5\cdot 7)$$

$$\frac{\partial}{\partial t}\delta\pi = -\pi\mathbf{V}_{x,y}\cdot\nabla_{x,y}(\frac{\delta\pi}{\pi}) - \frac{\gamma\pi}{B_z}D \qquad (5\cdot 8)$$

$$\frac{\partial}{\partial t}\delta B_z = -B_z\mathbf{V}_{x,y}\cdot\nabla_{x,y}(\frac{\delta B_z}{B_z}) - D \qquad (5\cdot 9)$$

$$\delta\mathbf{I}^i_{x,y} = \Sigma_P\nabla_{x,y}\delta\Phi + \delta\Sigma_P B_z\mathbf{V}_{x,y}\times\hat{z}$$
$$+ \Sigma_H\hat{z}\times\nabla_{x,y}\delta\Phi + \delta\Sigma_H B_z\mathbf{V}_{x,y} \qquad (5\cdot 10)$$

$$\delta J_z = -\nabla_{x,y}\cdot\delta\mathbf{I}^i_{x,y} \qquad (5\cdot 11)$$

$$\hat{z}\times\nabla_{x,y}\delta\Phi = B_z\delta\mathbf{V}_{x,y} + \mathbf{V}_{x,y}\delta B_z + \nabla_{x,y}\delta\Psi \qquad (5\cdot 12)$$

$$\nabla^2_{x,y}\delta\Phi = R - [B_z\mathbf{V}_{x,y}\times\nabla_{x,y}(\frac{\delta B_z}{B_z})]_z \qquad (5\cdot 13)$$

$$\nabla^2_{x,y}\delta\Psi = -D - B_z\mathbf{V}_{x,y}\cdot\nabla_{x,y}(\frac{\delta B_z}{B_z}) \qquad (5\cdot 14)$$

where D and R are defined as (4·21) and (4·22) of chapter 4; i.e.,

$$D = \nabla_{x,y}\cdot(B_z\delta\mathbf{V}_{x,y}) \qquad (5\cdot 15)$$

$$R = \nabla_{x,y}\cdot(B_z\delta\mathbf{V}_{x,y}\times\hat{z}) \qquad (5\cdot 16)$$

In this chapter, we study the perturbation from an 1–D flow or a pure circular flow.

5–1. Perturbation from 1–D Flow

For the next four sections (5–1 to 5–4), we take the zero-order flow as one dimensional in the x direction, i.e., $\mathbf{V}_{x,y} = V_x(x)\hat{x}$. The uniform flow is a special case. The zero-order equations are

$$mV_x = \text{const} \tag{5·17}$$

$$I_x = 0 \tag{5·18}$$

$$\begin{aligned} I_y B_z &= \frac{\partial \pi}{\partial x} + mV_x \frac{\partial V_x}{\partial x} \\ &= (C_S^2 - V_x^2)\frac{\partial m}{\partial x} \end{aligned} \tag{5·19}$$

where $C_S^2 = \gamma\pi/m$ as was already introduced in the previous chapter. The first order equations are

$$m\frac{\partial}{\partial t}\delta V_x = -V_x\delta(m\frac{\partial}{\partial x}V_x) - m\frac{\partial V_x}{\partial x}\delta V_x - \frac{\partial}{\partial x}\delta\pi + \delta B_z I_y + B_z\delta I_y$$

$$\begin{aligned} \text{or}\quad \frac{\partial}{\partial t}\frac{\delta V_x}{V_x} &= -\frac{\delta(mV_x^2)}{mV_x^2}\frac{\partial V_x}{\partial x} - V_x\frac{\partial}{\partial x}(\frac{\delta V_x}{V_x}) - \frac{\partial}{\partial x}(\frac{\delta\pi}{mV_x}) \\ &\quad + \frac{I_y}{mV_x}\delta B_z + \frac{B_z}{mV_x}\delta I_y \end{aligned} \tag{5·20}$$

$$\begin{aligned} &= -V_x\frac{\partial}{\partial x}(\frac{\delta V_x}{V_x} + \frac{\delta\pi}{mV_x^2}) + \frac{1}{\tau_2}\frac{\delta(mV_x^2+\pi)}{mV_x^2} \\ &\quad + \frac{I_y}{mV_x}\delta B_z + \frac{B_z}{mV_x}\delta I_y \end{aligned} \tag{5·20′}$$

$$\frac{\partial}{\partial t}\delta V_y = -V_x\frac{\partial}{\partial x}\delta V_y - \frac{1}{m}\frac{\partial}{\partial y}\delta\pi - \frac{B_z}{m}\delta I_x \tag{5·21}$$

$$\frac{\partial}{\partial t}\delta m = -m[V_x\frac{\partial}{\partial x}(\frac{\delta m}{m}) + \frac{D}{B_z}] \tag{5·22}$$

$$\frac{\partial}{\partial t}\delta\pi = -\pi[V_x\frac{\partial}{\partial x}(\frac{\delta\pi}{\pi}) + \gamma\frac{D}{B_z}] \tag{5·23}$$

$$= -mV_x^2[V_x\frac{\partial}{\partial x}(\frac{\delta\pi}{mV_x^2}) + \frac{C_S^2}{V_x^2}\frac{D}{B_z} - \frac{\gamma+1}{\tau_2}\frac{\delta\pi}{mV_x^2}] \tag{5·23'}$$

$$\frac{\partial}{\partial t}\delta B_z = -B_z[V_x\frac{\partial}{\partial x}(\frac{\delta B_z}{B_z}) + \frac{D}{B_z}] \tag{5·24}$$

$$\delta\mathbf{I}_{x,y} = \delta\mathbf{I}^i_{x,y}$$

$$= \Sigma_P\nabla_{x,y}\delta\Phi + \Sigma_H\hat{z}\times\nabla_{x,y}\delta\Phi - \hat{y}B_zV_x\delta\Sigma_P + \hat{x}B_zV_x\delta\Sigma_H \tag{5·25}$$

$$\delta J_z = -\nabla_{x,y}\cdot\delta\mathbf{I}^i_{x,y} \tag{5·26}$$

$$\nabla^2_{x,y}\delta\Phi = R - V_x\frac{\partial}{\partial y}\delta B_z \tag{5·27}$$

where

$$\frac{1}{\tau_2} = -\frac{\partial V_x}{\partial x} \tag{5·28}$$

$$= \frac{V_x}{m}\frac{\partial m}{\partial x}$$

$$= V_xk_B$$

and k_B is given as (4·58) of chapter 4. Taking the divergence and the rotation of (5·20) and (5·21) after multiplying by B_z, we have the equations for D and R:

$$\frac{\partial}{\partial t}D = -\frac{\partial}{\partial x}[V_xD] + \frac{\partial}{\partial x}[\frac{1}{\tau_2}B_z\delta V_x] + B_zV_x\frac{\partial}{\partial x}[\frac{1}{\tau_2}(\frac{\delta m}{m} + \frac{\delta V_x}{V_x})]$$
$$- \frac{B_z}{m}\nabla^2_{x,y}\delta\pi + \frac{B_z}{m}\frac{\partial}{\partial x}(I_y\delta B_z) + \frac{B_z^2}{m}\nabla_{x,y}(\delta\mathbf{I}_{x,y}\times\hat{z}) + \frac{B_z}{m}\frac{\partial B_z}{\partial x}\delta I_y$$
$$= \frac{D}{\tau_2} - V_x\frac{\partial D}{\partial x} + B_zV_x\frac{\partial}{\partial x}[\frac{1}{\tau_2}(\frac{\delta m}{m} + 2\frac{\delta V_x}{V_x})] - \frac{B_z}{m}\nabla^2_{x,y}\delta\pi + \frac{B_z}{m}\frac{\partial}{\partial x}(I_y\delta B_z)$$
$$+ \frac{\Sigma_H}{\Sigma_P}\frac{1}{\tau_1}\nabla^2_{x,y}\delta\Phi - \frac{B_zV_x}{\tau_1}(\frac{\partial}{\partial x}\frac{\delta\Sigma_P}{\Sigma_P} + \frac{\partial}{\partial y}\frac{\delta\Sigma_H}{\Sigma_P}) + \frac{1}{V_x\tau_1\tau_2}\frac{\delta I_y}{\Sigma_P} \tag{5·29}$$

$$\frac{\partial}{\partial t}R = \frac{R}{\tau_2} - V_x\frac{\partial R}{\partial x} + B_z V_x \frac{\partial}{\partial x}(\frac{1}{\tau_2}\frac{\delta V_y}{V_x}) - B_z V_x \frac{1}{\tau_2}\frac{\partial}{\partial y}(\frac{\delta m}{m} + \frac{\delta V_x}{V_x}) - \frac{B_z}{m} I_y \frac{\partial}{\partial y}\delta B_z$$
$$- \frac{1}{\tau_1}\nabla^2_{x,y}\delta\Phi - \hat{x}B_z V_x \tau_1 (\frac{\partial}{\partial x}\frac{\delta\Sigma_H}{\Sigma_P} - \frac{\partial}{\partial y}\frac{\delta\Sigma_P}{\Sigma_P}) - \frac{1}{V_x\tau_1\tau_2}\frac{\delta I_x}{\Sigma_P} \qquad (5\cdot 30)$$

where

$$\frac{1}{\tau_1} = \frac{\Sigma_P B_z^2}{m} \qquad (5\cdot 31)$$

is already determined in (4·37) of chapter 4. These are the basic equations for sections 5–2 and 5–3.

5–2. Perturbation from Parallel Uniform Flow

As the simplest case, we assume a uniform flow; i.e., the zero-order V_x, m, π and B_z are uniform. All of the zero-order equations (5·17) – (5·19) are automatically satisfied and we have $\mathbf{I}_{x,y} = 0$. Since the uniform condition means $1/\tau_2 = 0$, the first order equations are simplified to:

$$\frac{d}{dt}\delta m = -\frac{m}{B_z}D \qquad (5\cdot 32)$$

$$\frac{d}{dt}\delta\pi = -\frac{\gamma\pi}{B_z}D \qquad (5\cdot 33)$$

$$\frac{d}{dt}\delta B_z = -D \qquad (5\cdot 34)$$

$$\frac{dD}{dt} = -\frac{B_z}{m}\nabla^2_{x,y}\delta\pi + \frac{\Sigma_H}{\Sigma_P}\frac{1}{\tau_1}(R - V_x\frac{\partial}{\partial y}\delta B_z)$$
$$- \frac{B_z V_x}{\tau_1}(\frac{\partial}{\partial x}\frac{\delta\Sigma_P}{\Sigma_P} + \frac{\partial}{\partial y}\frac{\delta\Sigma_H}{\Sigma_P}) \qquad (5\cdot 35)$$

$$\frac{dR}{dt} + \frac{R}{\tau_1} = \frac{V_x}{\tau_1}\frac{\partial}{\partial y}\delta B_z - \hat{x}B_z V_x \tau_1 \left(\frac{\partial}{\partial x}\frac{\delta\Sigma_H}{\Sigma_P} - \frac{\partial}{\partial y}\frac{\delta\Sigma_P}{\Sigma_P}\right) \qquad (5 \cdot 36)$$

$$\delta J_z = \Sigma_P \tau_1 \frac{d}{dt} R \qquad (5 \cdot 37)$$

where d/dt is the zero-order full time derivative:

$$\frac{d}{dt} = \frac{\partial}{\partial t} + V_x \frac{\partial}{\partial x} \qquad (5 \cdot 38)$$

and $\delta\Sigma_P$ and $\delta\Sigma_H$ are given externally.

The first three equations (5·32) – (5·34) are exactly the same as the corresponding equations (4·26) – (4·28) of chapter 4 except for the difference in the time derivatives (partial or total) caused by Lorentz transformation. The advantage of the present expression (with nonzero V_x) is that we may also consider the energy dissipation because it is no more the second order quantity of δ. The last two equations (5·35) and (5·36) also correspond to Lorentz transformation of (4·33) and (4·34) of chapter 4. The additional terms (i.e., the zero-order $\mathbf{V}_{x,y}$ terms) here come from $\delta\mathbf{I}^i_{x,y}$. The field-aligned current is directly expressed by dR/dt instead of R itself (cf. (4·30) in chapter 4). The left-hand side of (5·36) causes exponential-type decay of R by Joule dissipation in the ionosphere, while the right-hand side excites nonzero R. Since the response of R to the source term is exponential, δJ_z also decays with a time constant τ_1 too. The behavior of δJ_z is the same as the $\mathbf{V}_{x,y} = 0$ case in chapter 4. If we assume $\delta V_{y0} = 0$, and $\partial/\partial x = 0$

for the first order quantities also, we have a shear flow; i.e., $D_0 = 0$. This case was already studied in section 4–2, and we do not discuss it here again.

We study two extreme cases: when $\delta\Sigma_P$ and $\delta\Sigma_H$ are the most important, and when they are negligible. Let us extract the effect of the conductivity gradient first, for the conductivity gradient is believed to play an important role in generating the region 2 field-aligned current [e.g., *Kan*, 1987]. In order to formulate this situation, we neglect δB_z terms and the $\delta\pi$ term compared to $\delta\Sigma_P$ terms or $\delta\Sigma_H$ terms in equations (5·35) and (5·36):

$$\frac{dD}{dt} = \frac{\Sigma_H}{\Sigma_P}\frac{R}{\tau_1} - \frac{B_z V_x}{\tau_1}\left[\frac{\partial}{\partial x}\left(\frac{\delta\Sigma_P}{\Sigma_P}\right) + \frac{\partial}{\partial y}\left(\frac{\delta\Sigma_H}{\Sigma_P}\right)\right] \tag{5·39}$$

$$\frac{dR}{dt} + \frac{R}{\tau_1} = \frac{B_z V_x}{\tau_1}\left[\frac{\partial}{\partial y}\left(\frac{\delta\Sigma_P}{\Sigma_P}\right) - \frac{\partial}{\partial x}\left(\frac{\delta\Sigma_H}{\Sigma_P}\right)\right] \tag{5·40}$$

Immediately from (5·40), R is

$$R = R_0 e^{-t/\tau_1} + \frac{B_z V_x}{\Sigma_P \tau_1} e^{-t/\tau_1} \int_0^t e^{t'/\tau_1}\left(\frac{\partial \delta\Sigma_P}{\partial y} - \frac{\partial \delta\Sigma_H}{\partial x}\right)dt' \tag{5·41}$$

The field-aligned current generation by the nonuniform conductivity is given as

$$\begin{aligned}\delta J_z &= \Sigma_P \tau_1 \frac{dR}{dt} \\ &= \delta J_{z0} e^{-t/\tau_1} + B_z V_x e^{-t/\tau_1} \int_0^t e^{t'/\tau_1} \frac{\partial}{\partial t'}\left(\frac{\partial \delta\Sigma_P}{\partial y} - \frac{\partial \delta\Sigma_H}{\partial x}\right)dt'\end{aligned} \tag{5·42}$$

where R_0 and J_{z0} are related as $\delta J_{z0} = -\Sigma_P R_0$. We can extract two effects from this equation: one is the simple decay of R from its initial value, and the

other is the modulation by the conductivity gradient. The response of the field-aligned current to the conductivity perturbations is delayed by a time constant τ_1. If $\delta\Sigma_P$ and $\delta\Sigma_H$ are time independent, the second term of (5·41) disappears. Only the x gradient (corresponds to north-south direction at midnight) of the Hall conductivity contributes to the field-aligned current generation.

Since the decay is associated with Joule dissipation in the ionosphere, this decay time has to be the same as the energy dissipation time. Suppose we have $\delta\mathbf{V}_{x,y} \neq 0$ at $t=0$. The initial extra kinetic energy is given as $m(\mathbf{V}_{x,y}+\delta\mathbf{V}_{x,y})^2 - mV_x^2 = 2mV_x\delta V_x$ in the first order approximation. Note that the energy becomes the second order quantity for the $\mathbf{V}_{x,y} = 0$ cases of chapter 4, and hence, we did not discuss the energy dissipation time there. The energy is consumed in the ionosphere with a rate of $\Sigma_P B_z^2(\mathbf{V}_{x,y}+\delta\mathbf{V}_{x,y})^2$, while we have the energy supply in the magnetosphere through the $\mathbf{I}^m_{x,y} \times \mathbf{B}$ force with a rate of $\Sigma_P B_z^2 V_x^2$. Net dissipation rate of the energy is $2\Sigma_P B_z^2 V_x \delta V_x$ to the first order. Therefore, the energy dissipation time is given as

$$\begin{aligned}\tau_1 &= \frac{2mV_x\delta V_x}{2\Sigma_P B_z^2 V_x \delta V_x} \\ &= \frac{m}{\Sigma_P B^2}\end{aligned}$$

Next, we neglect the conductivity gradient. Equations (5·35) for D and (5·36) for R are simplified to

$$\frac{dD}{dt} + \frac{B_z}{m}\nabla^2_{x,y}\delta\pi + \frac{\Sigma_H}{\Sigma_P}\frac{V_x}{\tau_1}\frac{\partial}{\partial y}\delta B_z = \frac{\Sigma_H}{\Sigma_P}\frac{R}{\tau_1} \qquad (5\cdot 43)$$

$$\tau_1 \frac{dR}{dt} + R = V_x \frac{\partial}{\partial y} \delta B_z \qquad (5 \cdot 44)$$

The second term of (5·43) comes from the pressure gradient force, and both of the Σ_H terms come from the $\delta \mathbf{I}_H \times \mathbf{B}$ drag force as is discussed in sections 4–2–1 and 4–2–3. However, the driving mechanisms for such ionospheric currents are different between the present case and the previous case (section 4–2). Here, the y component electric field is given as $V_x \delta B_z$. However, the zero-order convection is zero in section 4: the electric field has to be given as $B_z \delta V_x$, and this δV_x is driven by the $\mathbf{J} \times \mathbf{B}$ force ($I_y \delta B_z$ term). Both the R term and the δB_z term in (5·44) come from the $\delta \mathbf{I}_P \times \mathbf{B}$ force. According to the second equation, response of R to the change of δB_z is delayed. In order to simplify (5·43), we approximate (5·44) as

$$\frac{R}{\tau_1} = \eta_r \frac{V_x}{\tau_1} \frac{\partial}{\partial y} \delta B_z \qquad (5 \cdot 45)$$

where $0 < \eta_r < 1$. Strictly speaking, η_r is time dependent; however, we take it to be a constant. For slow phenomena (scale time $> \tau_1$), this is a good approximation because of $\eta_r \ll 1$. Taking the full time derivative (d/dt) of (5·43), we have a second order differential equation for D:

$$\frac{d^2 D}{dt^2} = C_S^2 \nabla_{x,y}^2 D + \frac{\Sigma_H}{\Sigma_P} V_x^2 k_V \frac{\partial}{\partial y} D \qquad (5 \cdot 46)$$

$$where \qquad k_V = \eta_r \frac{1}{V_x \tau_1} \qquad (5 \cdot 47)$$

This equation has the same structure as (4·66) of section 4–2–4. Both equations have the dispersive terms (last terms). As mentioned above, these terms come

from the $-\delta \mathbf{I}_H \times \mathbf{B}$ force. The solution for this equation is discussed later in section 5–4.

The wave of D also generates a significant amount of the field-aligned current. Combining (5·37), (5·44) and (5·34), the field-aligned current is approximately expressed as:

$$\delta J_z \sim -\eta_r \Sigma_P V_x \frac{\partial D}{\partial y} \qquad (5 \cdot 48)$$

Apparently, the senses of the field-aligned currents are opposite for the $+y$ propagation and the $-y$ propagation; it is consistent with both region 1 and region 2 field-aligned currents.

5–3. Inclusion of the Second Dimension

In this section, we employ the 1–D parallel compressional flow (cf. section 3–3) for the zero order. This flow includes the 1–D standing wave without the field-aligned currents. The gradient of the zero-order π is parallel to the gradient of B_z, as is automatically guaranteed by the 1–D assumption. This property and the $J_z = 0$ condition imply that the wave, if it exists, is a nonlinear extension of the linear $R = 0$ mode wave. We now add the linear perturbation which varies in the perpendicular direction of the flow as is shown in Figure 5–1.

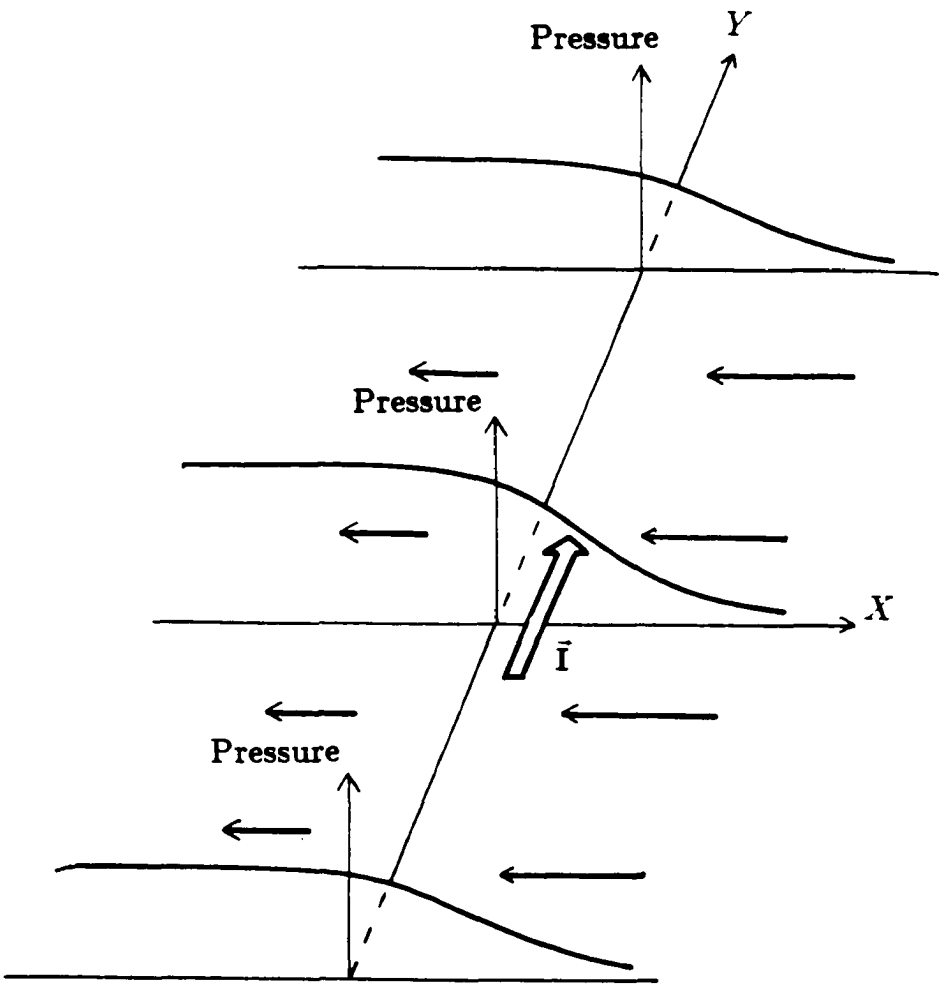

Figure 5–1. Electric current in a finite amplitude wave. Wave reference frame coordinates (X: propagation direction) are adopted. Pressure profile is indicated by solid lines. Since the inflow velocity (solid arrow) is expected to exceed C_S, the electric current (open arrow) flows in $+Y$ direction. The wave amplitude, and hence, the current intensity change in the y direction.

The basic equations are (5·20) – (5·27). According to the discussion in section 4–2, nonzero I_y causes y asymmetry through the dispersive term (last term of (4·66) of chapter 4) in the equation for D. The perturbation of δB_z causes x component convection δV_x through the magnetospheric $\mathbf{I} \times \mathbf{B}$ force because the zero-order I_y is not zero. As shown in Figure 2–3, the convection electric field produces the x component Hall current in the ionosphere, and the $\mathbf{I}_H \times \mathbf{B}$ force acts on the ionospheric plasma in the y direction. Its reaction force, which is represented by the last term ($B_z \delta I_x$ term) in equation (5·21), causes the y asymmetry. We concentrate on this mechanism under some simplified assumptions.

Since we study the wave, we do not include the conductivity gradient; we assume $\delta\Sigma = 0$. We also assume that τ_2 is uniform too. Now, let us examine if we may assume that the first order quantities depend only on y. That does not necessarily mean $(\partial/\partial x)\delta B_z = 0$; i.e., $(\partial/\partial x)(\delta B_z/B_z) = 0$ is also possible. Here, we take $\partial R/\partial x = 0$. In this sense, we assume that $\delta B_z/B_z$ and $\delta \mathbf{V}_{x,y}/V_x$ are x independent. Under these assumptions, equations for $\delta\Phi$ and $\delta\Psi$ become

$$\frac{\partial}{\partial y}\delta\Phi + \frac{\partial}{\partial x}\delta\Psi = -B_z\delta V_x - V_x\delta B_z$$

$$\frac{\partial}{\partial x}\delta\Phi - \frac{\partial}{\partial y}\delta\Psi = B_z\delta V_y$$

$$\nabla^2_{x,y}\delta\Phi = -B_z\frac{\partial}{\partial y}\delta V_x - V_x\frac{\partial}{\partial y}\delta B_z$$

$$\nabla^2_{x,y}\delta\Psi = -B_z\frac{\partial}{\partial y}\delta V_y$$

and hence,

$$\nabla_{x,y}\delta\Phi = -\hat{y}(B_z\delta V_x + V_x\delta B_z) \qquad (5\cdot 49)$$

$$\nabla_{x,y}\delta\Psi = -\hat{y}B_z\delta V_y$$

Equation (5·25) for $\delta\mathbf{I}_{x,y}$ is rewritten as

$$\delta\mathbf{I}_{x,y} = (\hat{x}\Sigma_H - \hat{y}\Sigma_P)B_zV_x(\frac{\delta V_x}{V_x} + \frac{\delta B_z}{B_z}) \qquad (5\cdot 50)$$

Since we consider the mechanism mentioned above, we neglect the kinetic terms in (5·20); i.e., the deviation satisfies

$$\delta(mV_x\frac{\partial V_x}{\partial x} + \frac{\partial \pi}{\partial x}) = 0$$

We also assume, as we did in the previous chapter, that $1/\tau_1 \gg \partial/\partial t \gg 1/\tau_2$; i.e., the zero-order gradient is small, and the decay of R is quick compared to the time scale of the field-aligned current. Under the above assumptions and with the help of (5·49) and (5·50), equations (5·20), (5·21) and (5·24) are simplified to

$$\frac{\partial}{\partial t}\frac{\delta V_x}{V_x} = \frac{I_y}{mV_x}\delta B_z - \frac{1}{\tau_1}(\frac{\delta V_x}{V_x} + \frac{\delta B_z}{B_z})$$

$$or \qquad \frac{I_y}{mV_x}\delta B_z = \frac{1}{\tau_1}(\frac{\delta V_x}{V_x} + \frac{\delta B_z}{B_z}) \qquad (5\cdot 51)$$

$$\frac{\partial}{\partial t}\frac{\delta V_y}{V_x} = \frac{1}{\tau_2}\frac{\delta V_y}{V_x} - \frac{\pi}{mV_x}\frac{\partial}{\partial y}\frac{\delta\pi}{\pi} - \frac{\Sigma_H}{\Sigma_P}\frac{1}{\tau_1}(\frac{\delta V_x}{V_x} + \frac{\delta B_z}{B_z})$$

$$or \qquad \frac{\partial}{\partial t}\delta V_y = -\frac{\partial}{\partial y}\frac{\delta\pi}{m} - \frac{\Sigma_H}{\Sigma_P}\frac{I_y}{m}\delta B_z \qquad (5\cdot 52)$$

$$\frac{\partial}{\partial t}\delta B_z = -D \qquad (5\cdot 53)$$

By taking the y derivative after multiplication by B_z, the second equation is further rewritten as

$$\frac{\partial}{\partial t}D = -\frac{\partial^2}{\partial y^2}\frac{B_z\delta\pi}{m} - \frac{\Sigma_H}{\Sigma_P}\frac{B_z I_y}{m}\frac{\partial}{\partial y}\delta B_z \qquad (5\cdot 54)$$

This equation is the same as (4·65) in chapter 4 in which the zero-order I_y is expressed as $B_z I_y = \partial\pi/\partial x$. Thus, equation (5·54) is a generalized form of (4·65) in chapter 4. As is expected, the last term comes from the $\delta\mathbf{I}_H \times \mathbf{B}$ force, and this Hall current is driven by δV_x through the convection electric field.

Taking the time derivative of (5·54), we have

$$\frac{\partial^2 D}{\partial t^2} = C_S^2\frac{\partial^2 D}{\partial y^2} + \frac{\Sigma_H}{\Sigma_P}\frac{B_z I_y}{m}\frac{\partial D}{\partial y} \qquad (5\cdot 55)$$

where we used

$$\frac{\partial}{\partial t}\frac{\delta\pi}{m} = -C_S^2\frac{D}{B_z} \qquad (5\cdot 56)$$

This equation is obtained if we also assume $(\partial/\partial x)(\delta\pi/\pi) = 0$. In this case, we may not assume the x independence for $\delta m/m$ because of the condition (5·51).

Equation (5·55) is the governing equation for the longitudinal wave (D mode) propagating perpendicular to the zero-order gradient. This form is more general than the final form of section 4–2–3. According to (5·19), the current flows in the $+y$ direction if the inflow velocity exceeds C_S as is the case with the nonlinear fast mode wave. This situation is demonstrated in Figure 5–1. Otherwise, it is

in the $-y$ direction, which is the same as in section 4–2–3. Thus, the sign of the coefficient of (5·55) is opposite from the previous cases.

5–4. Amplitude Modulation of Waves

The final equations of section 4–2–2 (equation (4·59) of chapter 4), section 4–2–3 (equation (4·65) of chapter 4), section 5–2 (equation (5·46)), and section 5–3 (equation (5·55)) have the same form. Only the initial conditions and the signs of the coefficient for the last terms are different. Here, we consider a general form:

$$\frac{\partial^2 D}{\partial t^2} = C_S^2\left(\frac{\partial^2 D}{\partial z^2} + \alpha\frac{\partial D}{\partial z}\right) \qquad (5\cdot 57)$$

$$where \qquad C_S^2 = \frac{\gamma\pi}{m}$$

We set $z = x$ and $\alpha = -k_B > 0$ in order to apply to 4–2–2, while we set $z = y$ and $\alpha = (\Sigma_H/\Sigma_P)k_B < 0$ for 4–2–3, $\alpha = (\Sigma_H/\Sigma_P)(V_x^2/C_S^2)k_B < 0$ for 5–2, and $\alpha = (\Sigma_H/\Sigma_P)(B_z I_y/mC_S^2)$ for 5–3. For simplicity, C_S and α are assumed to be constants. The coefficient α can be either positive or negative. The initial conditions are given by $D_0 = D|_{t=0}$ and $D_1 = \partial D/\partial t|_{t=0}$. The solution of (5·57) has to be different from the ordinary wave because of the effect of α. We examine the effect of α on the original wave equation.

Let us adopt the Fourier transform for the z which is defined as

$$D_k(t) = \int_{-\infty}^{\infty} D(t,z)e^{-ikz}dz \qquad (5\cdot 58)$$

$$D(t,z) = \frac{1}{2\pi}\int_{-\infty}^{\infty} D_k(t)e^{ikz}dk \qquad (5\cdot 59)$$

If $D(z=\pm\infty)=0$, we may apply (5·58) to equation (5·57):

$$\frac{\partial^2 D_k}{\partial t^2} + C_S^2(k^2 - ik\alpha)D_k = 0 \qquad (5\cdot 60)$$

The general solution of this equation is

$$D_k = c_f(k)\exp(-i\omega t) + c_b(k)\exp(i\omega t) \qquad (5\cdot 61)$$

$$where \qquad \omega^2 = C_S^2(k^2 - ik\alpha) \qquad (5\cdot 62)$$

We consider modifications of the wave equation by α, and we can take α small. Therefore, ω is approximated as

$$\omega = C_S k - \frac{i}{\tau_2} \qquad (5\cdot 63)$$

$$where \qquad \tau_2 = \frac{2}{C_S\alpha} \qquad (5\cdot 64)$$

and $D(t,z)$ is expressed as

$$\begin{aligned} D(t,z) = \exp(-\frac{t}{\tau_2})\frac{1}{2\pi}\int_{-\infty}^{\infty} c_f(k)\exp[ik(z - C_S t)]dk \\ + \exp(\frac{t}{\tau_2})\frac{1}{2\pi}\int_{-\infty}^{\infty} c_b(k)\exp[ik(z + C_S t)]dk \end{aligned} \qquad (5\cdot 65)$$

The first term corresponds to a forward propagating wave, and the second term corresponds to a backward propagating wave. The coefficients (c_f and c_b) are

determined from the initial conditions:

$$c_f(k) + c_b(k) = \int_{-\infty}^{\infty} D_0(z) e^{-ikz} dz$$
$$-ik(c_f(k) - c_b(k)) = \int_{-\infty}^{\infty} D_1(z) e^{-ikz} dz$$

or

$$c_f(k) = \frac{1}{2}\int_{-\infty}^{\infty} D_0(z') e^{-ikz'} dz' - \frac{1}{2ik}\int_{-\infty}^{\infty} D_1(z') e^{-ikz'} dz'$$
$$c_b(k) = \frac{1}{2}\int_{-\infty}^{\infty} D_0(z') e^{-ikz'} dz' + \frac{1}{2ik}\int_{-\infty}^{\infty} D_1(z') e^{-ikz'} dz'$$

Substituting $c_f(k)$ into the first terms on the left side of (5·65), the forward propagating wave is calculated as

$$\begin{aligned} D_f(t,z) &= \frac{1}{2}\exp(-\frac{t}{\tau_2})[\frac{1}{2\pi}\int_{-\infty}^{\infty} D_0(z')dz' \int_{-\infty}^{\infty} e^{ik(z-C_S t-z')}dk \\ &\quad - \frac{1}{2\pi i}\int_{-\infty}^{\infty} D_1(z')dz' \int_{-\infty}^{\infty} \frac{1}{k} e^{ik(z-C_S t-z')}dk] \\ &= \frac{1}{2}\exp(-\frac{t}{\tau_2})[\int_{-\infty}^{\infty} D_0(z')\delta(z - C_S t - z')dz' \\ &\quad - \int_{-\infty}^{\infty}\int^{z'} D_1(z")dz"\delta(z - C_S t - z')dz'] \\ &= \frac{1}{2}\exp(-\frac{t}{\tau_2})[D_0(z - C_S t) - \int^{z-C_S t} D_1(z")dz"] \end{aligned}$$

The backward propagating wave is calculated similarly. Combining both, the solution for $D(t,z)$ is obtained as

$$D(t,z) = \frac{1}{2}\exp(-\frac{t}{\tau_2})W(\zeta = z - C_S t)$$

$$+\frac{1}{2}\exp(\frac{t}{\tau_2})W(\zeta = z + C_S t) \qquad (5\cdot 66)$$

$$where \qquad W(\zeta) = D_0(\zeta) - \int^{\zeta} D_1(z')dz' \qquad (5\cdot 67)$$

The first term of (5·66) represents a forward propagating wave while the second term represents a backward propagating wave. The sign of τ_2 depends on the sign of α, and it determines whether the propagating wave grows or decays. In other words, the wave propagation is asymmetric along the y direction even though the zero-order configuration is symmetric.

Let us apply this result to the more general case (5·55). Since $\alpha = (\Sigma_H/\Sigma_P)(B_z I_y/mC_S^2)$, $sign(\tau_2) = sign(I_y)$ where I_y is the zero-order current direction. Apparently, the wave is amplified in the $-I_y$ direction. For the case of section 4–2–3, we have $I_y < 0$, and hence, the wave is amplified in the $+y$ direction. Now, we consider a nonlinear wave in the plasma sheet travelling toward the tail (cf. section 5–3). On the front side of the wave, the current flows dawnward. It is caused by the dynamo mechanism of the finite amplitude wave; i.e., the flow is decelerated losing its kinetic energy, and the current flows in the opposite direction to the convection electric field. That dynamo current has to connect with the region 1 field-aligned current. Thus, the macroscopic wave on the region 1 field-aligned current system is amplified as it travels westward. However, on the other places, the wave is amplified as it travels eastward. Further discussions are presented in chapter 6 based on the numerical results.

As mentioned in the previous sections, the α term comes from the y asymmetry of the $\mathbf{I}_H \times \mathbf{B}$ force. This force is responsible for the wave amplification or decay in the y direction. The longitudinal wave ($\delta V_y \neq 0$) causes increase of $B_z V_x$ by $V_x \delta B_z$ or by $B_z \delta V_x$ (in this case, $I_y \delta B_z$ causes δV_x because $I_y \neq 0$). The additional convection electric field causes the ionospheric current, and hence, the $\mathbf{J} \times \mathbf{B}$ force on the ionospheric plasma. The force caused by the Pedersen current is symmetric, while the part caused by the Hall current is asymmetric in the $\pm y$ directions. Therefore, its reaction force on the plasma sheet is asymmetric too; i.e., the reaction force enforces or decreases the pressure gradient restoring force of the wave.

Let us consider the energy. We have to consider the ultimate force that causes the asymmetry. For the case of section 5–3 or 4–2–3, $I_y \delta B_z$ drives the convection δV_x. Thus, the energy change by this force is $I_y \delta B_z \delta V_x$, which is a second order quantity.

5–5. Perturbation from a Circular Flow

As it is one of the typical convection patterns observed in space [*Hones et al.*, 1983], we consider a circular flow. The zero-order equations are given in section 3–4 in which incompressible circular flow with $V_r = 0$ is assumed. Since our interest is the effect of the circular configuration, we assume $\partial/\partial\phi = 0$ for the first order

quantities too. Therefore, for an arbitrary vector $\mathbf{A}_{x,y}$ and an arbitrary function f, we have

$$\nabla_{x,y}\delta f = \hat{r}\frac{\partial}{\partial r}\delta f$$
$$\nabla_{x,y}\cdot\delta\mathbf{A}_{x,y} = \frac{1}{r}\frac{\partial}{\partial r}(r\delta A_r)$$

We assume that $\delta\Sigma_P = \delta\Sigma_H = 0$ because we have already studied this effect in 5–2. For the same reason, we also assume uniform B_z (and hence, uniform π) as the zero order. This assumption provides $\hat{r}V_\phi \propto 1/r$ from the zero-order $J_z = 0$ condition. In this case, the centripetal force mV_ϕ^2/r is to be balanced with the $\mathbf{J}\times\mathbf{B}$ force instead of the pressure gradient force. Under these assumptions, the field-aligned current is expressed as

$$\delta J_z = -\Sigma_P B_z V_\phi \frac{\partial}{\partial r}\left(\frac{\delta V_\phi}{V_\phi} + \frac{\delta B_z}{B_z}\right) \qquad (5\cdot 68)$$

Apparently, the change of V_ϕ (which might be caused by the viscous-like interaction) causes the field-aligned current generation. The other first order basic equations (5·6) – (5·10) are rewritten in (r,θ) cylindrical coordinates as:

$$\delta I_r^i = \Sigma_P B_z V_\phi\left(\frac{\delta V_\phi}{V_\phi} + \frac{\delta B_z}{B_z}\right) \qquad (5\cdot 69)$$
$$\delta I_\phi^i = \frac{\Sigma_H}{\Sigma_P}\delta I_r^i \qquad (5\cdot 70)$$
$$m\frac{\partial}{\partial t}\delta\mathbf{V}_{x,y} = \frac{\delta(mV_\phi^2)}{r}\hat{r} - \frac{m\delta V_r}{r}\frac{\partial}{\partial r}(rV_\phi)\hat{r} - \nabla_{x,y}\delta\pi$$
$$+ I_\phi\delta B_z\hat{r} + B_z\delta\mathbf{I}_{x,y}^i\times\hat{z}$$

$$or \qquad m\frac{\partial}{\partial t}\delta V_r = \frac{\delta(mV_\phi^2)}{r} - \frac{\partial}{\partial r}\delta\pi + I_\phi \delta B_z$$
$$+ \Sigma_H B_z^2 V_\phi \left(\frac{\delta V_\phi}{V_\phi} + \frac{\delta B_z}{B_z}\right) \qquad (5\cdot 71)$$

$$m\frac{\partial}{\partial t}\delta V_\phi = -\Sigma_P B_z^2 V_\phi \left(\frac{\delta V_\phi}{V_\phi} + \frac{\delta B_z}{B_z}\right) \qquad (5\cdot 72)$$

$$\frac{\partial}{\partial t}\delta m = -\frac{m}{B_z} D \qquad (5\cdot 73)$$

$$\frac{\partial}{\partial t}\delta\pi = -\frac{\gamma\pi}{B_z} D \qquad (5\cdot 74)$$

$$\frac{\partial}{\partial t}\delta B_z = -D \qquad (5\cdot 75)$$

$$where \qquad D = \frac{B_z}{r}\frac{\partial}{\partial r}(r\delta V_r) \qquad (5\cdot 76)$$

$$R = \frac{B_z}{r}\frac{\partial}{\partial r}(r\delta V_\phi) \qquad (5\cdot 77)$$

From (5·77) and (5·72), the equation for R is given as

$$\frac{m}{B_z}\frac{\partial}{\partial t}R = -\Sigma_P B_z \left(R + V_\phi \frac{\partial}{\partial r}\delta B_z\right) \qquad (5\cdot 78)$$

Therefore, the field-aligned current is also expressed as $\delta J_z = \Sigma_P \tau_1 \partial R/\partial t$.

We study two cases: (1) nonzero δV_ϕ is given in the steady state; and (2) nonzero δV_r is given in the steady state.

5–5–1. Pure Circular Flow

We consider a situation in which $\delta V_\phi \neq 0$ is given initially. This perturbation can be caused by the viscous-like interaction. The initial value problem with nonzero δV_ϕ is essentially the same as 4–2–1. We may simplify the basic equations

with the assumption of $\delta V_\phi > \delta V_r$. Since $R \gg D$ according to (5·76) and (5·77), the main equation is (5·78). As is expected from the result of section 4–2–1, we have a decay equation. However, this equation is modified by δB_z (and hence, D) because of the nonzero V_ϕ.

The effect of $D \neq 0$ on the behavior of R cannot be neglected if the δB_z term becomes as large as the R term in the equation for R. The equation for δV_r is approximated as

$$\frac{\partial}{\partial t}\delta V_r \sim (\frac{2V_\phi}{r} + \frac{\Sigma_H}{\Sigma_P}\frac{1}{\tau_1})\delta V_\phi \qquad (5 \cdot 79)$$

Substituting (5·79) and (5·76) into (5·75), we have

$$\begin{aligned}\frac{\partial^2}{\partial t^2}\delta B_z &= -2B_z\delta V_\phi\frac{\partial}{\partial r}(\frac{V_\phi}{r} - \frac{B_z}{r}(\frac{2V_\phi}{r} + \frac{\Sigma_H}{\Sigma_P}\frac{1}{\tau_1})\frac{\partial}{\partial r}(r\delta V_\phi) \\ &= \frac{4B_z\delta V_\phi V_\phi}{r^2} - (\frac{2V_\phi}{r} + \frac{\Sigma_H}{\Sigma_P}\frac{1}{\tau_1})R\end{aligned}$$

Since we have nonzero V_ϕ, we may set $B_z\delta V_\phi/r$ smaller than R. Therefore,

$$\delta B_z \sim -\Omega_1 R t^2$$

$$where \qquad \Omega_1 = \frac{2V_\phi}{r} + \frac{\Sigma_H}{\Sigma_P}\frac{1}{\tau_1} \qquad (5 \cdot 80)$$

The decay equation (5·78) is rewritten as

$$\frac{\partial}{\partial t}R = -\frac{1}{\tau_1}[R + V_\phi t^2\frac{\partial}{\partial r}(\Omega_1 R)] \qquad (5 \cdot 81)$$

This result is valid for small t when $R \gg D$; i.e., t has to be smaller than r/V_ϕ and τ_1.

5–5–2. Cyclone-Type Flow

Circular flows with nonzero V_r are typical phenomena both in space and on the earth. Even on the solar surface, some of the sunspots show this spiral flow. Here, we consider the vacuuming effect on the circular flow. We assume $\delta V_\phi = 0$ instead of $\delta V_r = 0$ at $(t=0)$; i.e., we consider the effect of δV_r. Immediately following this assumption, we have $R_0 = 0$. Therefore, $R \ll D$ is assumed in the basic equations.

The basic equations for R and D under $R \ll D$ are

$$\frac{m}{B_z}\frac{\partial D}{\partial t} = -(\frac{m}{B_z}\frac{\partial}{\partial r}\delta B_z - \frac{\partial}{\partial r}\delta m)\frac{V_\phi^2}{r} - \frac{m}{r}(\frac{\delta B_z}{B_z} - \frac{\delta m}{m})\frac{\partial}{\partial r}(V_\phi^2)$$
$$- \nabla_{x,y}^2 \delta\pi + \Sigma_H B_z V_\phi \frac{\partial}{\partial r}\delta B_z \qquad (5\cdot 82)$$

$$R = \frac{V_x}{\tau_1} e^{-t/\tau_1} \int_0^t e^{t'/\tau_1} \frac{\partial}{\partial r}\delta B_z dt' \qquad (5\cdot 83)$$

where the field-aligned current is expressed as

$$\delta J_z = -\Sigma_P V_\phi \frac{\partial}{\partial r}\delta B_z \qquad (5\cdot 84)$$
$$= \Sigma_P V_\phi \int_0^t \frac{\partial D}{\partial r} dt'$$

The vacuuming in the circular flow (nonzero δV_r) causes the field-aligned current generation. In other words, a cyclone-type structure in space [e.g., *Hones et al*, 1983] is generating the field-aligned current. Note that δV_r can be related to δT_z; i.e., if we first have a δT_z–like meteorological cyclone, that causes nonzero δV_r, $\delta\pi$ and δm.

Let us examine the behavior of D. Taking the time derivative of (5·82), we have

$$\frac{m}{B_z}\frac{\partial^2 D}{\partial t^2} = [\frac{m}{B_z}\frac{\partial}{\partial r}D - \frac{\partial}{\partial r}(\frac{m}{B_z}D)]\frac{V_\phi^2}{r} + \frac{m}{r}(\frac{D}{B_z} - \frac{mD}{B_z m})\frac{\partial}{\partial r}(V_\phi^2)$$
$$+ \frac{1}{r}\frac{\partial}{\partial r}[r\frac{\partial}{\partial r}(\frac{\gamma\pi}{B_z}D)] - \Sigma_H B_z V_\phi \frac{\partial D}{\partial r}$$

$$or \qquad \frac{\partial^2 D}{\partial t^2} = C_S^2 \frac{1}{r}\frac{\partial}{\partial r}(r\frac{\partial D}{\partial r}) - \frac{\Sigma_H}{\Sigma_P}V_\phi \tau_1 \frac{\partial D}{\partial r} \qquad (5 \cdot 85)$$

This equation has the same form as (5·47) of section 5–2, and the solution is to be given in the same manner as 5–4.

CHAPTER 6. NUMERICAL STUDY

The field-aligned current generation in the plasma sheet, coupled with the ionosphere, is studied by means of numerical simulations. The time evolutional equations are integrated by the Two Step Lax Wendroff method [*MacCormack*, 1969], and a Poisson's equation is solved by the method of *Boisvert* [1984]. We specifically consider the situation when an enhanced convection (uniform) hits the inner edge of the plasma sheet [e.g., *Jaggi and Wolf*, 1973], i.e., the plasmapause. The resultant compression causes the increase of pressure there. We study the response of the M–I coupling system to this situation. For example, the redistribution of the pressure (that moves the plasma) and the field-aligned currents are studied. Therefore, our simulation box is located tailward of the inner edge of the plasma sheet. The meshes of the simulation box are $0.04\ L_0 \times 0.04\ L_0$, and the box size is $1.6\ L_0 \times 1.6\ L_0$. Note that $L_0 \gg h_0$ and hence, $L_0 \gg 1$ Re (earth radius).

Since we consider the dynamics caused by the two-dimensional flow, we do not consider the effect of T_z (unit mass transfer from $z = h$ boundary). Therefore, we set $u_z = 0$ and $h = h_0 = uniform$. We also neglect the change of the mapping point which is expressed by equation (2·29). In order to examine the validity of the numerical result, including the numerical instability, we perform a comparative study for different parameters, and also we compare the result with the analytical results.

6–1. Dimensionless Equations

First, we obtain dimensionless basic equations. Let V_0, B_0, ρ_0, P_0, and Σ_0 be the initial values of $|V_{x,y}|$, B_z, ρ, P, and Σ_P at the inflow boundary. We normalize the basic equations of chapter 2 by these reference values. The dimensionless time is defined as $\tau = (V_0/L_0)t$ where L_0 is the length of the area under consideration.

The dimensionless basic equations under the above assumptions are

$$m^*\frac{\partial}{\partial\tau}\mathbf{V}^*_{x,y} + m^*(\mathbf{V}^*_{x,y}\cdot\nabla^*_{x,y})\mathbf{V}^*_{x,y} = -M_S^{-2}\nabla^*_{x,y}\pi^* + \frac{L_0}{h_0}M_A^{-2}B^*_z(\mathbf{I}^*_{x,y}\times\hat{z}) + M_A^{-2}\zeta J^*_z\mathbf{I}^*_{x,y} \quad (6\cdot1)$$

$$\mathbf{I}^*_{x,y} = \mathbf{I}^{i*}_{x,y} + \mathbf{I}^{m*}_{x,y} \quad (6\cdot2)$$

$$\frac{\partial}{\partial\tau}m^* + \nabla^*_{x,y}\cdot(m^*\mathbf{V}^*_{x,y}) = 0 \quad (6\cdot3)$$

$$\frac{\partial}{\partial\tau}\pi^* + \nabla^*_{x,y}\cdot(\pi^*\mathbf{V}^*_{x,y}) = -(\gamma-1)\pi^*\nabla^*_{x,y}\cdot\mathbf{V}^*_{x,y} \quad (6\cdot4)$$

$$\frac{\partial}{\partial\tau}B^*_z + \nabla^*_{x,y}\cdot(B^*_z\mathbf{V}^*_{x,y}) = 0 \quad (6\cdot5)$$

$$\eta I^{i*}_x = \frac{\xi_y}{\xi_x}\Sigma_P^{(m)^*}\left(\frac{\partial}{\partial y^*}\Psi^* + V^*_yB^*_z\right) + \Sigma_H^{(m)^*}\left(\frac{\partial}{\partial x^*}\Psi^* + V^*_xB^*_z\right) \quad (6\cdot6)$$

$$\eta I^{i*}_y = -\frac{\xi_x}{\xi_y}\Sigma_P^{(m)^*}\left(\frac{\partial}{\partial x^*}\Psi^* + V^*_xB^*_z\right) + \Sigma_H^{(m)^*}\left(\frac{\partial}{\partial y^*}\Psi^* + V^*_yB^*_z\right) \quad (6\cdot7)$$

$$J^*_z(z=h) = -\nabla^*_{x,y}\cdot\mathbf{I}^{i*}_{x,y} \quad (6\cdot8)$$

$$\nabla^{*2}_{x,y}\Psi^* = -\nabla^*_{x,y}\cdot(\mathbf{V}^*_{x,y}B^*_z) \quad (6\cdot9)$$

where $x^* = x/L_0$, $y^* = y/L_0$, $\mathbf{V}^*_{x,y} = \mathbf{V}_{x,y}/V_0$, $B^*_z = B_z/B_0$, $\rho^* = \rho/\rho_0$, $P^* = P/P_0$, $\Sigma_P^{(m)^*} = \Sigma_P^{(m)}/\Sigma_0$, $\Sigma_H^{(m)^*} = \Sigma_H^{(m)}/\Sigma_0$, $m^* = m/(\rho_0h_0)$, $\pi^* = \pi/(P_0h_0)$, Ψ^*

$= \Psi/(L_0 V_0 B_0)$, $\mathbf{I}^*_{x,y} = \mathbf{I}_{x,y}/(B_0/\mu_0)$, $J^*_z = J_z/(B_0/\mu_0 L_0)$, $M_A = V_0/(B_0/\sqrt{\mu_0\rho_0})$, $M_S = V_0/\sqrt{P_0/\rho_0}$, $\beta = P_0/(B_0^2/2\mu_0) = 2M_A^2/M_S^2$, and $\eta = 1/(\mu_0\Sigma_0 V_0)$. In order to see the effect of the Hall conductivity, we simulate for different Σ^*_H values; i.e., Σ^*_H is treated as a parameter, like η and ξ_x/ξ_y.

The condition (2·9') becomes

$$\beta = O(1)$$

The magnetospheric part of the plasma sheet current $\mathbf{I}^{m*}_{x,y}$ is given externally, and has to satisfy $\nabla^*_{x,y}\cdot\mathbf{I}^{m*}_{x,y} = 0$. Also, ξ_x/ξ_y, Σ_P, and Σ_H are given externally.

Since we apply the Two Step Lax Wendroff method [*MacCormack*, 1969], we rewrite the time evolutional equations in conservative forms. The continuity equation (6·3), energy equation (6·4), and the induction equation (6·5) are already in the conservative forms. The momentum equation is rewritten as

$$\frac{\partial}{\partial\tau}(m^*V^*_x) + \nabla^*_{x,y}\cdot(m^*V^*_x\mathbf{V}^*_{x,y}) = -M_S^{-2}\frac{\partial\pi^*}{\partial x^*} + \frac{L_0}{h_0}M_A^{-2}I^*_y B^*_z + M_A^{-2}\zeta J^*_z I^*_x \qquad (6\cdot 10)$$

$$\frac{\partial}{\partial\tau}(m^*V^*_y) + \nabla^*_{x,y}\cdot(m^*V^*_y\mathbf{V}^*_{x,y}) = -M_S^{-2}\frac{\partial\pi^*}{\partial y^*} - \frac{L_0}{h_0}M_A^{-2}I^*_x B^*_z + M_A^{-2}\zeta J^*_z I^*_y \qquad (6\cdot 11)$$

The equation set (6·2) – (6·11) is simpler than the ordinary 2-D MHD equations because the (x, y) components of the induction equation are replaced by the ionospheric Ohm's law. In this sense, Ampere's law is not included, which is the

same assumption as in the convection model [*Harel et al.*, 1981; *Wolf and Spiro*, 1985]. The numerical stability of these basic equations must be better because we have the resistive terms in the momentum equations because of the ionospheric conductivity.

6–2. Enhancement of Plasma Sheet Convection

As mentioned above, we consider the situation when an enhanced earthward convection hits the inner edge of the plasma sheet, and compresses the plasma. Since our simulation box is located tailward of the inner edge of the plasma sheet, the effect of the compression does not exist inside the box. In this way, we may assume the initial flow uniform inside the simulation box at $\tau = 0$. We set the simplest initial condition: $\Psi^* = 0$, $V_y^* = 0$, $J_z^* = 0$, and uniform V_x^*, B_z^*, m^*, and π^*. Since all the above quantities are uniform in the present case, we have $V_x^* = 1$, $m^* = 1$, $B_z^* = 1$, $\pi^* = 1$, and $\Sigma_P^* = 1$ as the initial conditions. According to the momentum equation, we immediately have $\mathbf{I}_{x,y}^* = 0$. Therefore, the magnetospheric part of the plasma sheet current is

$$I_x^{m*} = I_x^* - I_x^{i*}$$
$$= -\frac{\Sigma_H^*}{\eta}$$
$$I_y^{m*} = I_y^* - I_y^{i*}$$

$$= \frac{1}{\eta}\frac{\xi_x}{\xi_y}$$

This $\mathbf{I}^{m*}_{x,y}$ is assumed to be constant throughout the simulation; i.e., we do not study the effect of the temporal change of the $\mathbf{J} \times \mathbf{B}$ driving force. For the same reason, we can assume the boundary values of $\mathbf{I}^{i*}_{x,y}$ to be constant throughout the simulation too.

Next, we consider the boundary conditions associated with the compression by enhanced convection at the inner edge of the plasma sheet. We increase the pressure at the outflow boundary. This condition is common for several different physical situations. For example, if we set $\rho = const$ at the same boundary, the situation is simply an increase of the temperature. In this case, the plasma heating takes place on the downstream boundary. If the density also increases such that it satisfies $\rho \propto P^{1/\gamma}$ at that boundary, the density increase takes place downstream, obeying the polytropic law. However, unless the magnetic field on that boundary is specified, we may not distinguish if the density increase is caused by the compression of the convection, or the injection of the plasma from the $z = h$ boundary ($T_z = 0$ assumption is not imposed at the boundary). If B_z also increases accordingly, we may consider that the situation represents the plasma compression. We consider this case. Practically, we set the outflow ρ and B_z

conditions according to

$$\frac{dm^*}{d\tau} = \frac{1}{\gamma}\frac{d\pi^*}{d\tau} = \frac{dB_z^*}{d\tau}$$

where $d/d\tau$ is the Lagrange derivative.

Let us describe this condition explicitly in terms of the mesh points (i, j). We take a fluid element on the outflow boundary at $\tau = \tau_n$, where n is the time step. Since the quantities at the outflow boundary are the results of the convection, the boundary values at $\tau = \tau_n$ can be determined in terms of the previous ($\tau = \tau_{n-1}$) values of the same fluid element at the previous position of this fluid element. In this procedure, we just need to know the total time (Lagrange) derivative, or the compressibility $\nabla_{x,y}\cdot\mathbf{V}_{x,y}$, instead. Thus, $\nabla_{x,y}\cdot\mathbf{V}_{x,y}$ is the only quantity that we may specify; i.e., we may not specify more than two quantities at the same time on the outflow boundary. Note that we presumed $T_z = 0$ also at the boundary. Otherwise, we may specify m^* and π^* independently. In this case, we may consider the temperature increase as mentioned above.

Here, we specify the pressure instead of $\nabla_{x,y}\cdot\mathbf{V}_{x,y}$, and the other quantities are determined in terms of $\nabla_{x,y}\cdot\mathbf{V}_{x,y}$. This method is essentially the same as *Leith*'s method [1965] by which we may avoid the mismatch of the outflow boundary conditions caused by the over-determination. We specify the pressure in the present

situation. The other quantities, not only m^* and B_z^*, but also $m^*\mathbf{V}_{x,y}^*$, are determined in terms of this *Leith*'s method as they are written in the conservative forms. Note that there are additional terms in the momentum equation caused by the pressure gradient force and the $\mathbf{J} \times \mathbf{B}$ force.

Now, we impose the pressure increase at the outflow ($i = 1$) boundary:

$$\pi_{1,j}^*(n) = (1 + \lambda\tau_n)\pi_{1,j}^*(0) \qquad for\ n < n_0$$

$$\pi_{1,j}^*(n) = \pi_{1,j}^*(n_0) \qquad for\ n < n_0$$

where n is the time step and λ is a constant factor. The compression is expressed as

$$\nabla_{x,y}^* \cdot \mathbf{V}_{x,y}^* = \frac{1}{\gamma\bar{\pi}^*}\frac{\Delta\pi^*}{\Delta\tau}$$

where $\Delta\pi^*$ is the change of the pressure of the same fluid element from τ_{n-1} to τ_n, and $\bar{\pi}^*$ is the average of the pressure of these two points. The pressure increase on the outflow boundary is the greatest in the center and smoothly diminishes towards the dusk or dawn side edge. Eventually, the degree of the pressure increase is linearly interpolated between the center and the dawn or dusk side edge on the outflow boundary. The pressure increase continues constantly from $n = 0$ to n_0. We increase the pressure up to twice its initial value in $\tau = 2$. According to the linear analysis, this condition can excite the waves because of not only $D \neq 0$

but also of $\partial D/\partial t \neq 0$ at the outflow boundary. In the present simulation, $\Delta\tau$ is determined for each time step according to the velocity as

$$\Delta\tau = \frac{1}{4}\frac{Min(\Delta x, \Delta y)}{U_{max} + C_S}$$

Let us move to the other boundaries (upstream and sides). The boundary values may not be determined externally because the change of these boundary values should be the result of the propagation (or conduction) of the change of the pressure from the outflow boundary. Practically, we set a 'free' boundary condition for the inflow boundary and side boundaries. That 'free' condition provides constant values until the effect of the pressure change arrives there, and also provides an inelastic boundary for waves; i.e., any deviations that belong to the wave propagating normal to the boundary are all transmitted through those boundaries, and the amplitudes of the reflected waves are negligibly small. This 'free' boundary condition is achieved by setting the first spatial derivative in the normal direction as zero. In fact, the wave is reflected at these boundaries if we do not employ the 'free' boundary condition.

6–3. Numerical Results

There are several parameters that are given externally. We do not study all combinations of these parameters. We first choose a basic set of parameters, and

later, we change these parameters one by one so that we may compare and study the different value of each parameter. The examined parameter sets are listed in Table 6–1.

6–3–1. Wave Formation

Figures 6–1*a* to 6–1*d* show the numerical results (nonlinear) at 100, 250, 500 and 1500 time steps, respectively, when $\eta = 1$, $\xi_x/\xi_y = 1$, $\Sigma_H^* = 0.5$, $M_A^2 = 0.2$, $M_S^2 = 0.5$ (i.e., $\beta = 0.8$), $\gamma = 1$ (isothermal), and $T_z^* = 0$. The top left panels show the pressure π^*, the top right panels show the velocity $\mathbf{V}_{x,y}^*$, the bottom left panels show the field-aligned current J_z^*, and the bottom right panels show the magnetospheric current $\mathbf{I}_{x,y}^*$. The distributions of B_z and ρ are similar to that of the pressure, and hence, we do not show them here. Since we set the background pressure uniform at $\tau = 0$, there is no background current such as the dawn to dusk current. In the real magnetosphere, we have to add such currents to the 'total' current in the figure.

As one can recognize from Figure 6–1*a* ($\tau = 0.41$), the increased pressure at the outflow boundary propagates in the form of a wave. As is shown in section 4–4, we have only one mode of propagating a wave in the (x, y) direction (perpendicular to **B**). The wave front is characterized by a dusk to dawn current as well as the steep pressure increase. This is followed by a gradual increase of the pressure. Since the

Table 6–1 Parameters of Numerical Models

Figure	Demonstrated τ	M_a^2	M_s^2	β	γ	η	Σ_H^*	ξ_x/ξ_y
Default		0.2	0.5	0.8	1.0	1.0	+0.5	1.0
6–1	0.4, 1.0, 2.0, 6.1	–	–	–	–	–	–	–
6–2	1.0, 2.0	0.4	1.0	–	–	–	–	–
6–3	1.0, 2.0	0.1	0.25	–	–	–	–	–
6–4	1.0, 2.0, 6.1	0.4	–	1.6	–	–	–	–
6–5	0.4, 1.0	0.1	–	0.4	–	–	–	–
6–6	1.0, 1.0	–	0.25	1.6	–	–	–	–
6–7	1.0, 2.0	–	–	–	2.0	–	–	–
6–8	0.4, 1.0	–	–	–	–	0.2	–	–
6–9	0.4, 1.0, 2.0	–	–	–	–	5.0	–	–
6–10	1.0, 6.2	–	–	–	–	–	0	–
6–11	0.4, 1.0	–	–	–	–	–	–	2.0
6–12	1.0, 2.1, 6.1	–	–	–	–	–	–	0.5

Table 6–1. Parameters of Numerical Models

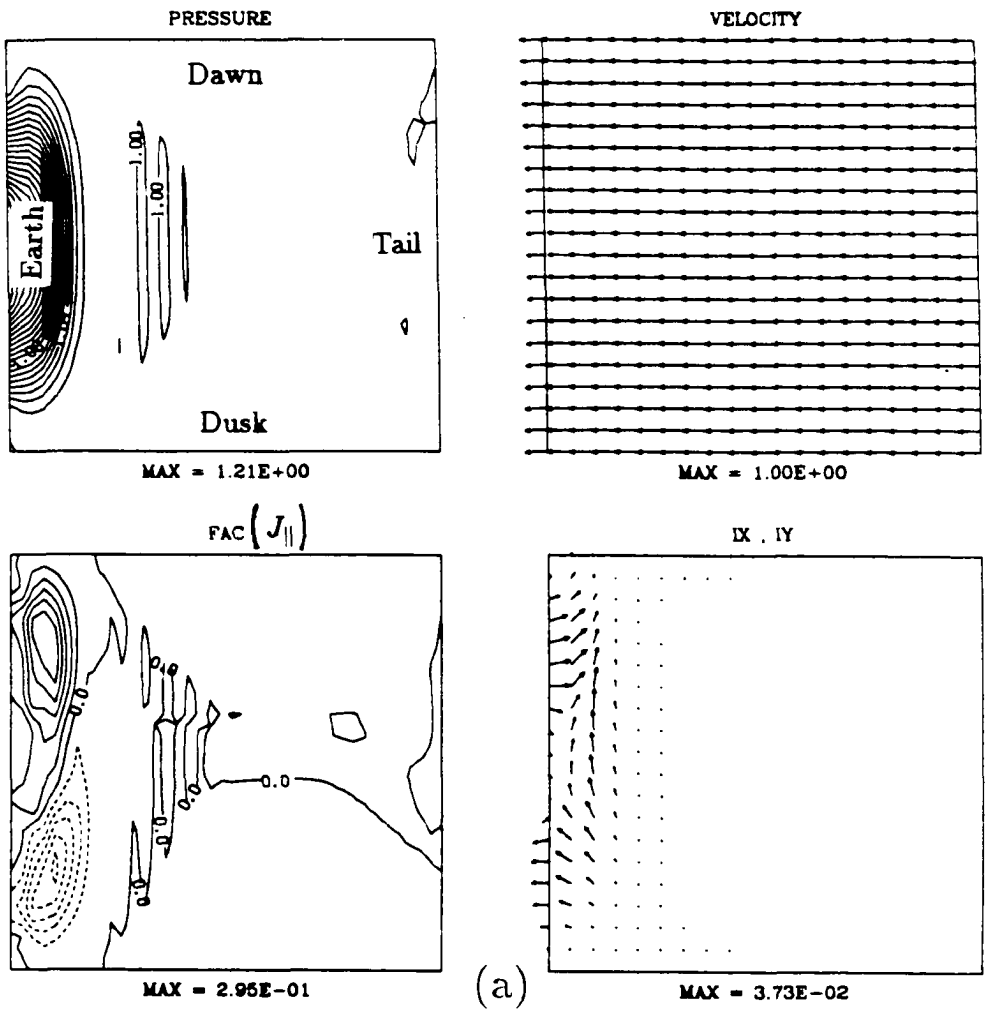

Figure 6–1. Numerical results for basic parameters. They are $\eta = 1$, $\xi_x/\xi_y = 1$, $\Sigma_H^* = 0.5$, $M_A^2 = 0.2$, $M_S^2 = 0.5$ (i.e., $\beta = 0.8$), $\gamma = 1$ (isothermal), and $T_z^* = 0$. Results at (a) 100 time steps, (b) 250 time steps, (c) 500 time steps, and (d) 1500 time steps are listed. The top left panels show the pressure π^*, the top right panels show the velocity $\mathbf{V}_{x,y}^*$, the bottom left panels show the field-aligned current J_z^*, and the bottom right panels show the magnetospheric current $\mathbf{I}_{x,y}^*$. The distributions of B_z and ρ are similar to that of the pressure, and hence, we do not show them here.

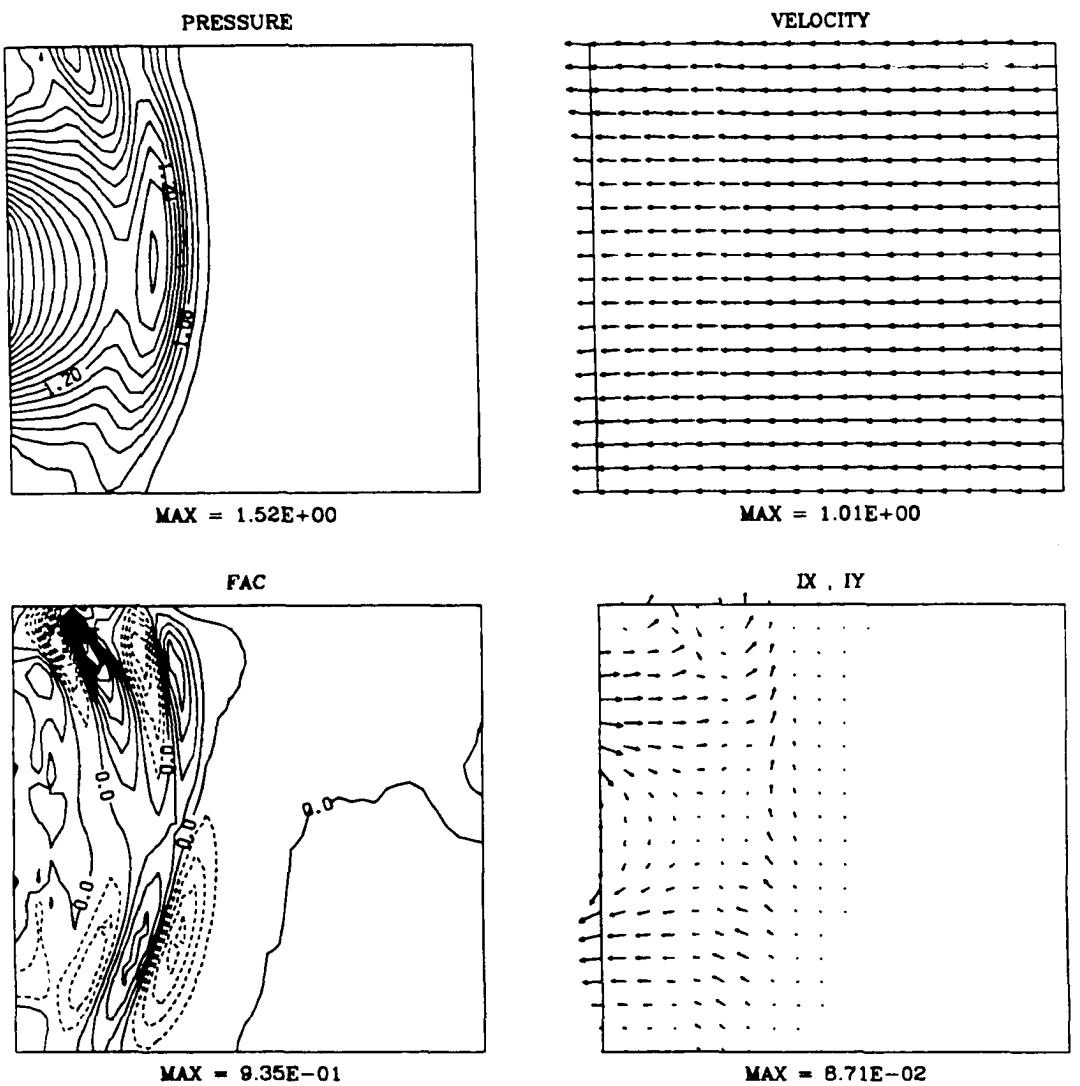

Figure 6–1 (b) 250 time steps ($\tau = 1.03$)

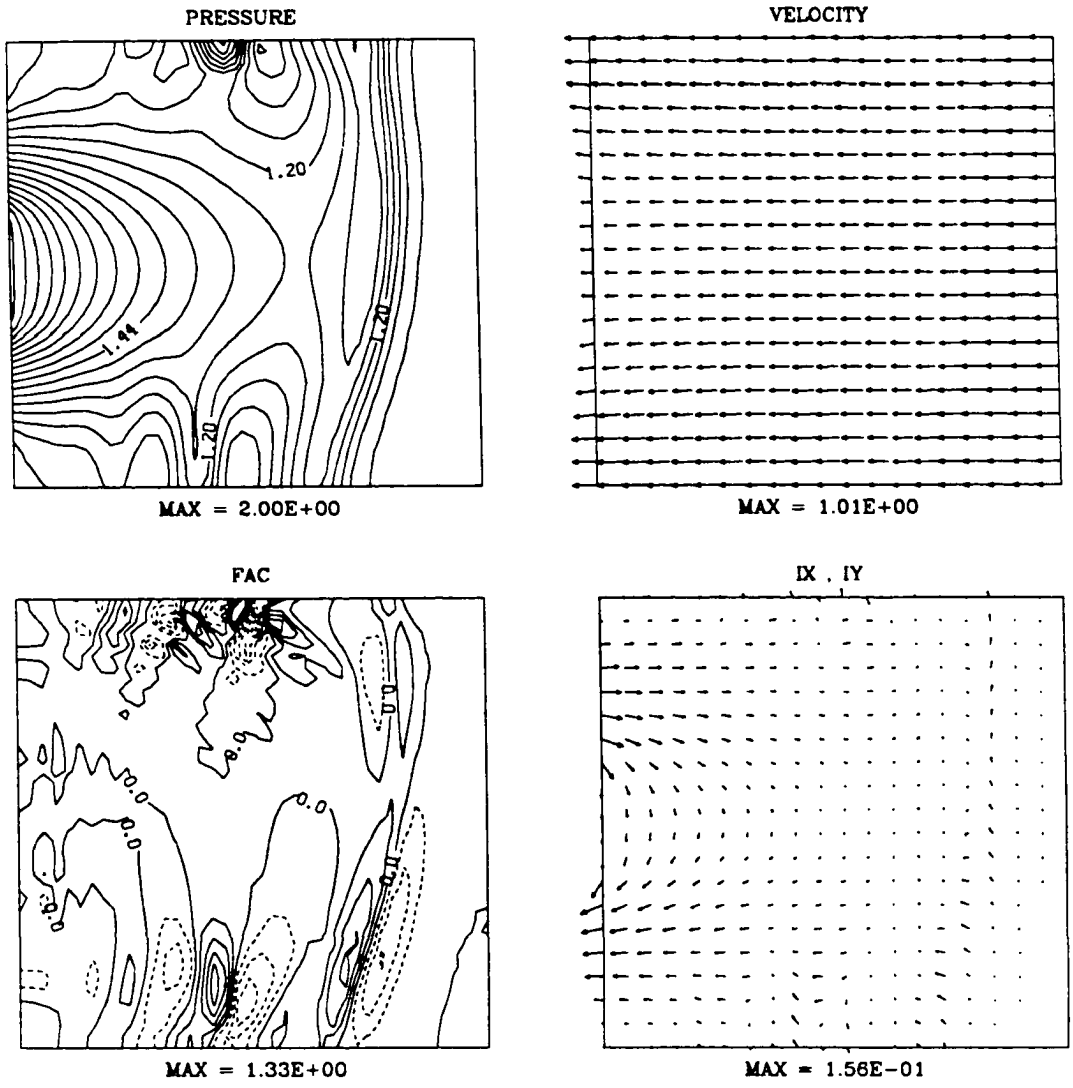

Figure 6–1 (c) 500 time steps ($\tau = 2.05$)

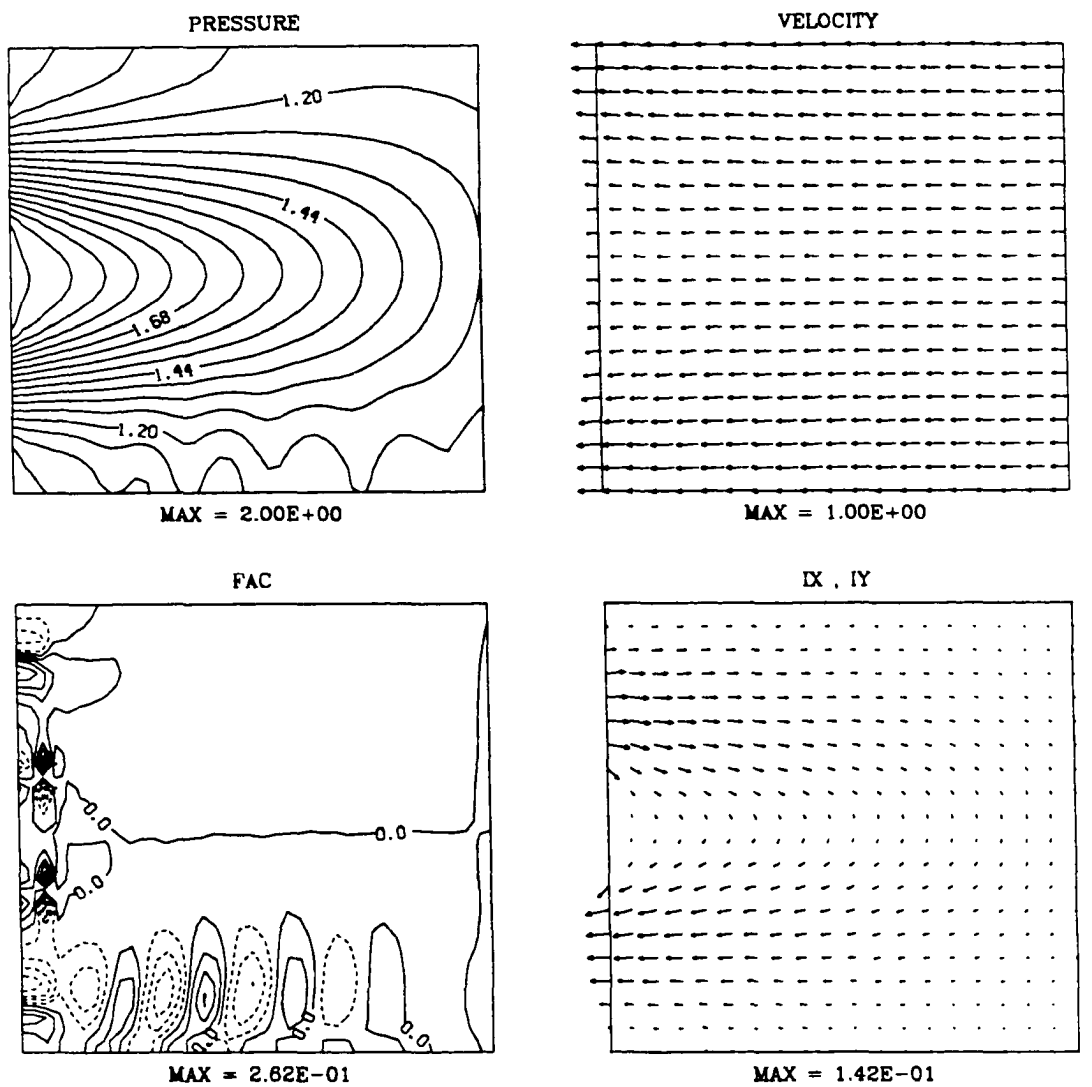

Figure 6–1 (d) 1500 time steps ($\tau = 6.12$)

convection electric field is duskward, the current satisfies the dynamo condition: $\mathbf{I} \cdot \mathbf{E} < 0$. The kinetic energy of the convection changes to electromagnetic energy because of this wave. The divergence of the dusk to dawn current produces a pair of field-aligned currents. Its sense is of the region 1 field-aligned current's; i.e., the field-aligned current flows into the ionosphere on the dawn side, and flows out of the ionosphere on the dusk side. The intensity of the field-aligned current is 0.3 on the normalized scale, that is, the order of $10^{-7}\,\mathrm{A/m^2}$ in the ionosphere. It agrees with the observation [e.g., *Kamide et al.*, 1986]. Since the inner edge of the plasma sheet is located outside (downstream) of the simulation box, the region 2 field-aligned current does not necessarily exist in the present result. An asymmetry is found between dawn and dusk in the pressure. This asymmetry comes from the Hall conductivity as is examined later.

The simulation code is examined for the linear case; i.e., when the pressure increase is as small as 10%. The qualitative feature is the same as Figure 6–1, and is consistent with the linear analysis for waves as is shown below.

Now, let us compare 100 time steps ($\tau = 0.41$) and 250 time steps ($\tau = 1.03$). The thickness of the wave in terms of the field-aligned currents decreases: the wave is steepening as it propagates. The field-aligned current distribution at 250 time steps is more complicated; a new pair of intense field-aligned currents is found at the downstream side of the first pair. The flow directions of the field-aligned

currents are opposite between this pair and the first pair; i.e., the second pair flows with the region 2 field-aligned current's sense.

A more complicated feature is found at 500 time steps ($\tau = 2.05$). The wave propagation is faster on the dawn side than the dusk side. The intensities of the field-aligned currents are much stronger in the dusk side than in the dawn side for both pairs. This result is consistent with the analytical result of sections 5–3 and 5–4 because the current is flowing from dusk to dawn. The asymmetry has been attributed to the ionospheric Hall current in these sections. We study the effect of the ionospheric Hall conductivity later in this chapter too.

We also observe a wake-like structure behind the intense field-aligned currents. However, it is not certain whether this wake-like structure is actual or merely numerical noise, especially in the vicinity of the side boundaries. These (artificial or real) wakes first appear on the dawn side (250 time steps). Pressure decrease behind the wave contributes to the formation of the wakes. Later, at 500 time steps, they appear on the dusk side too and the dusk side wakes remains longer after the dawn side wakes propagate out of the upstream boundary. At 1500 time steps ($\tau = 6.12$), only the dusk side wakes exist. In order to find out whether the wake structure behind the wave is actual or artificial, we have to simulate for different parameters and compare the results. Therefore, we do not claim it is the wake structure. Note that the small structure at the vicinity of the outflow

boundary is an artificial one caused by the solid boundary condition. Other than the wake-like structure, the distributions at 1500 time steps can be considered as the asymptotic states; the pressure distribution of the convection is such that there is no field-aligned current. This is consistent with the analytical result. In fact, the convection is divergence-free and rotation-free, and the B_z distribution is very similar to the pressure distribution so that ∇P is parallel to $\nabla|B|$. The y component of the plasma sheet current is dawn to dusk on the noon-midnight meridian and is divergence-free.

According to section 3-3, the resultant current direction (dusk to dawn) implies $|V_x| > C_S$ on the wave reference frame. This is also verified directly from the figure. The wave propagates 1.3 L_0 in 500 time steps ($\tau = 2.05$); i.e., the propagation speed is 0.68 on the simulation box. Adding the flow velocities on the upstream side (=1.0) and on the downstream side (=0.75), the convection velocities with respect to the wave are given as 1.7 and 1.4 on the upstream and the downstream sides, respectively. It is a few hundred km/sec in the real space. On the other hand, the normalized sound speed can be calculated as $M_S^{-1} = 1.4$, which is the same as the downstream side convection velocity. The Mach number is nearly 1.2 at the upstream side whereas it is nearly unity at the downstream side. Note that the sound speed does not change through the wave because $\gamma = 1$.

Let us identify the wave mode. As is studied in section 4–4, there exists only one propagating wave mode (the MHD fast mode wave) on the convection reference frame. The MHD fast wave propagates with the local sound speed in the present system. If the wave is nonlinear, the convection velocities on the upstream side have to be larger than the sound speed. Also, the changes of the pressure and the magnetic field are in phase for the fast mode wave. Both features are observed for the simulated wave. We may conclude that it corresponds to the MHD fast mode wave.

The MHD fast wave does not generate field-aligned currents in the linear approximation. Even the nonlinear wave does not generate field-aligned currents if the wave is one dimensional as shown in section 3–3. In fact, on the meridian line in the simulation box ($y = 0$), we do not observe the field-aligned currents. However, the wave amplitude changes in the y direction because of the outflow boundary condition. As the result, the wave front carries the finite pressure change, and it provides the background pressure gradient in the y direction while the wave propagates in the x direction. In this case, the R (Alfvén) mode and the D (fast) mode are coupled through the ionospheric Hall current as shown in section 4–4.

The dynamo mechanism is strong in the center and weak on the dawn/dusk sides. That causes the divergence of the dynamo current to generate the second

pair of field-aligned currents. Figure 6–1*b* also shows that the second pair of field-aligned currents is the result of the divergence of the x component current. The divergence of I_x contributes both pairs of the field-aligned currents. Therefore, the first pair is always stronger than the second pair.

According to section 4–4, the field-aligned current (R mode) is excited by the MHD fast mode (D mode), which is essentially independent of the field-aligned current generation. The simulated wave in the simulation keeps the features of the MHD fast mode (propagation direction, propagation speed, change of B and π are in phase, and compression at the wave front) except that it is accompanied by the field-aligned currents. If the R mode becomes separated from the D mode, it is possible that smaller field-aligned current systems are convected downstream as the decaying Alfvén mode.

Let us apply this result to the substorm. The simulated wave might correspond to the poleward expansion after the substorm onset. According to Figure 2–1, the poleward corresponds to the tailward. The expansion is slightly faster on the dawn side, and it generates the region 1 field-aligned currents according to the present result. The more intense field-aligned currents on the dusk side is also observed. It might contribute to the westward travelling surge, though it is not very clear. Both phenomena are considered large-scale, as is the present model. The complicated field-aligned current patterns associated with the wake-like structure, if it is not

numerical noise, can explain the complicated field-aligned current patterns around local midnight.

6–3–2. Effect of Convection Velocity

Figures 6–2*a* and 6–2*b* (200 and 400 time steps, respectively) show the results when we set $M_A^2 = 0.4$ instead of 0.2. All the other parameters are the same as in the previous case except the same β value implies $M_S^2 = 1.0$ instead of 0.5. $M_S = 1.0$ means that a linear D mode wave does not move in the simulation box reference frame. However, the propagation speed of the finite amplitude wave is faster than the sound (the MHD fast mode) speed as is seen in Figure 6–1. Thus, the wave is still propagating upstream.

The features at 200 time steps ($\tau = 1.00$) are essentially the same as the previous case, with some minor differences. The dawn-dusk asymmetry is more clear in the present case according to the pressure. Since the propagation velocity is slower in Figure 6–2 than Figure 6–1, quantities such as the pressure and the field-aligned current have steeper gradients. Thus, we can see the intense plasma sheet currents and field-aligned currents near the wave. Their amplitudes are more than twice those of Figure 6–1. The steeper gradient introduces a numerical instability on the wake-like structure (or numerical noise). Especially, a severe instability appears on the dawn side near the outflow boundary at 400 time steps ($\tau = 1.96$). It is

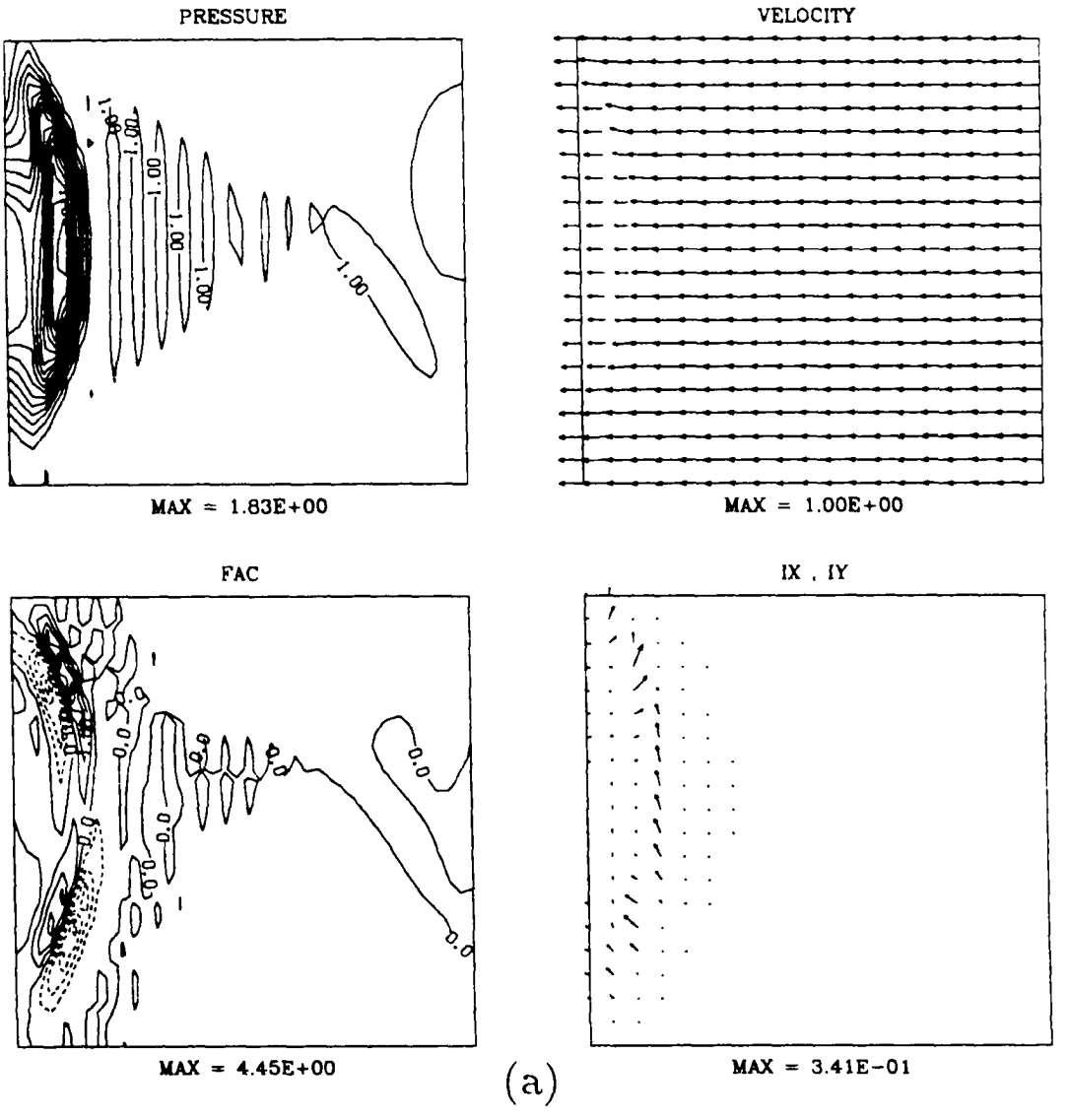

Figure 6–2. Numerical results when $M_A^2 = 0.4$ instead of 0.2. All the other parameters are the same as in the previous case except the same β value implies $M_S^2 = 1.0$ instead of the 0.5 of FIgure 6–1. Results at (a) 200 time steps and (b) 400 time steps are listed.

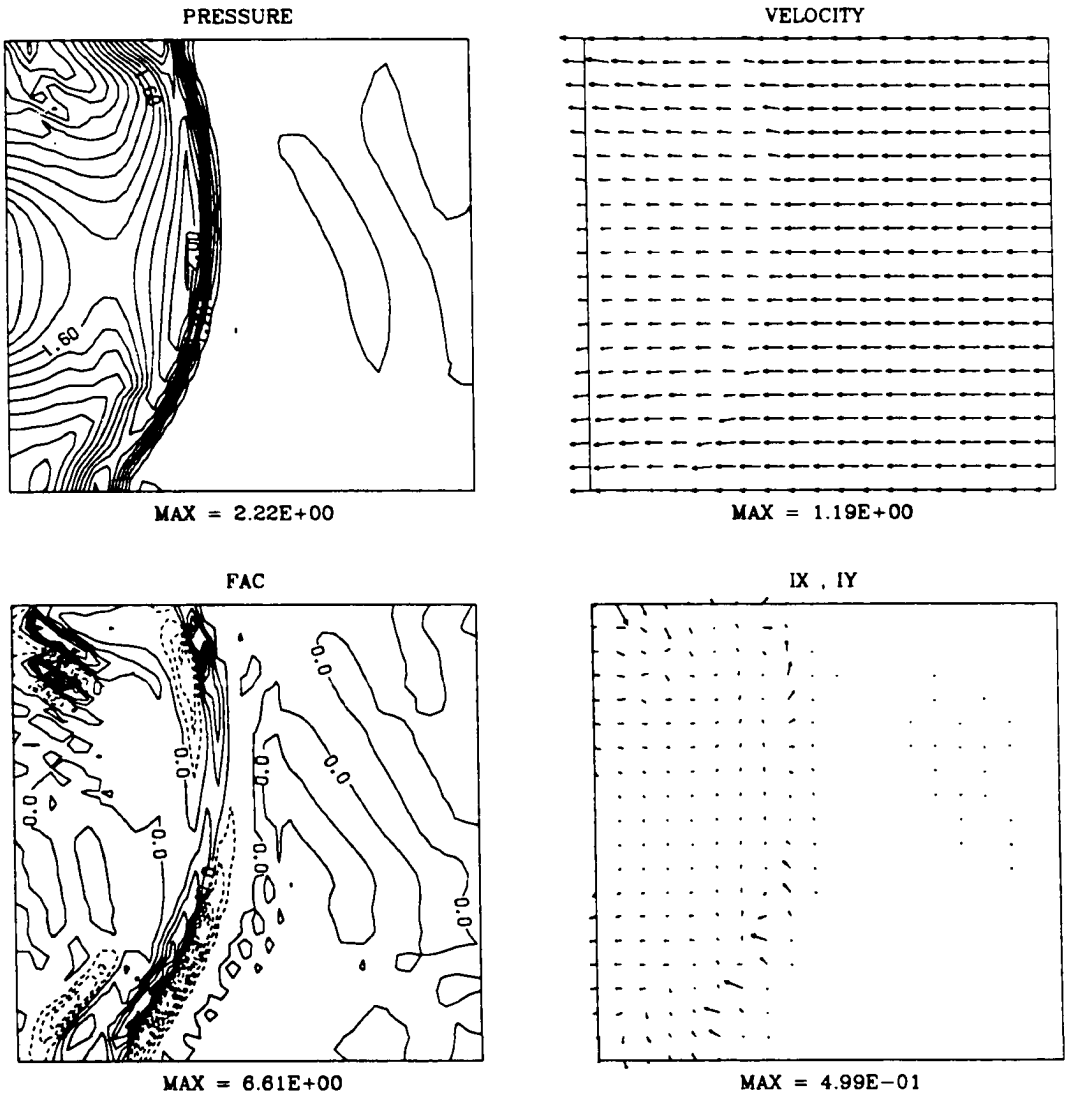

Figure 6–2 (b) 400 time steps ($\tau = 1.96$)

a crucial one so that the simulation breaks down at 400 time steps. Even though we have the crucial instability near the boundary, the wave itself is outstanding as is clearly recognized from the figure, partly because the wave amplitude is much larger than the wake. Actually, we may not recognize any clear wakes except the one that causes the instability mentioned above. Thus, only one pair of intense field-aligned currents exists near the wave front, and we cannot recognize any other field-aligned currents associated with the wake.

These results are the same if we set $M_A^2 = 0.3$ instead of 0.4; i.e., $M_S^2 = 0.75$ instead of 1. In this case, the amplitude of the numerical instability is still large, while the amplitude of the wave is smaller. Therefore, the results are not as clear as in the above two cases.

Next, we reduce the convection velocity. Figures 6–3*a* (300 time steps) and 6–3*b* (600 time steps) show the results when we set $M_A^2 = 0.1$. All the other parameters are the same as in Figure 6–1 and Figure 6–2 except the M_S value; i.e., $M_S^2 = 0.25$ because β values are the same. Since both the sound speed and the Alfvén speed are doubled compared to the convection velocity, we can expect that the wave propagation speed is also doubled, which is the opposite case from Figure 6–2.

The information of "pressure increase" propagates upstream with the expected speed. However, according to the results at 300 time steps ($\tau = 0.99$) none of four panels shows the formation of a steepened nonlinear wave: the pressure change

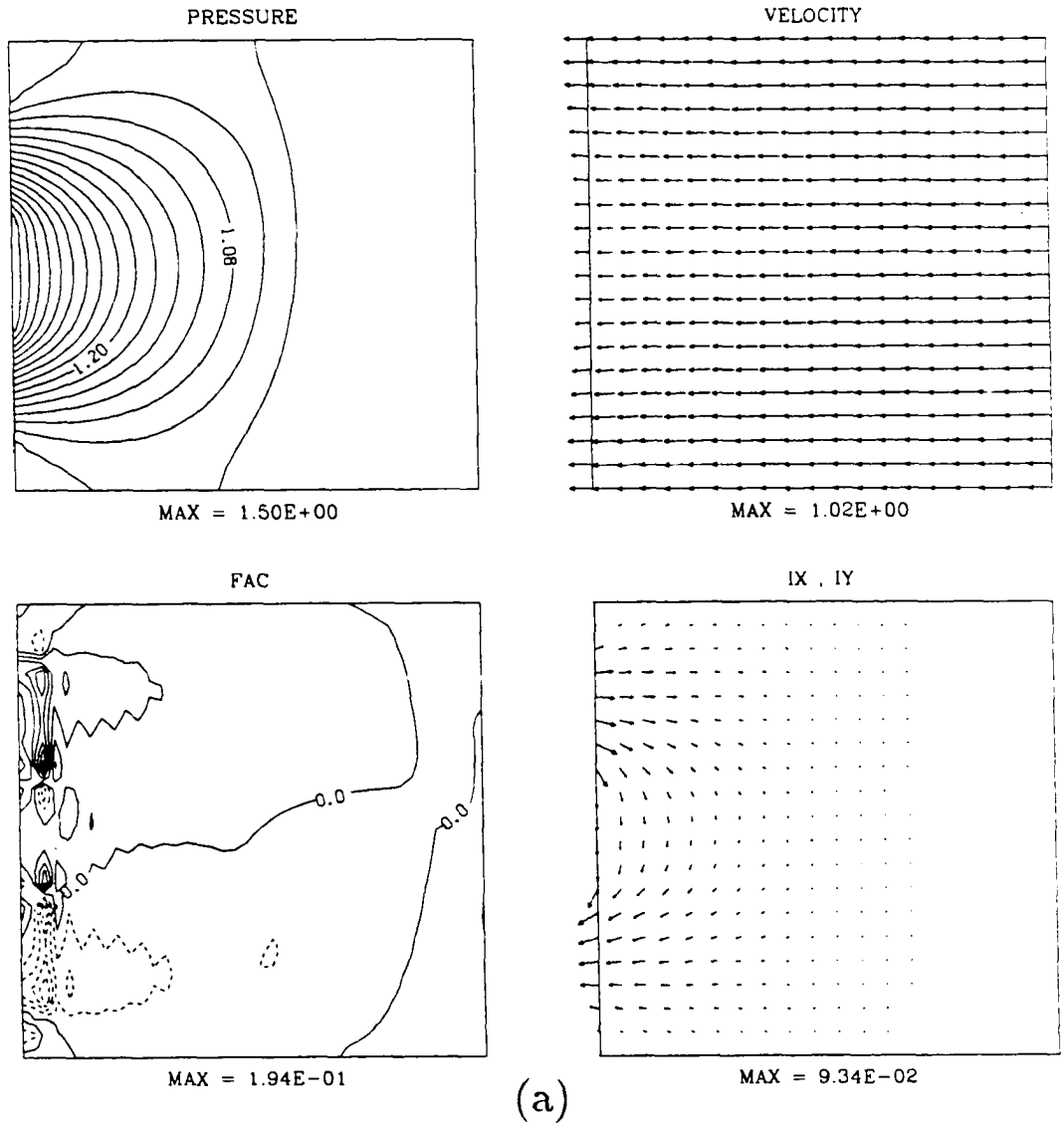

Figure 6–3. Numerical results when $M_A^2 = 0.1$. All the other parameters are the same as in Figure 6–1 and Figure 6–2 except the M_S value; i.e., $M_S^2 = 0.25$ because β values are the same. Results at (a)300 time steps and (b) 600 time steps are listed.

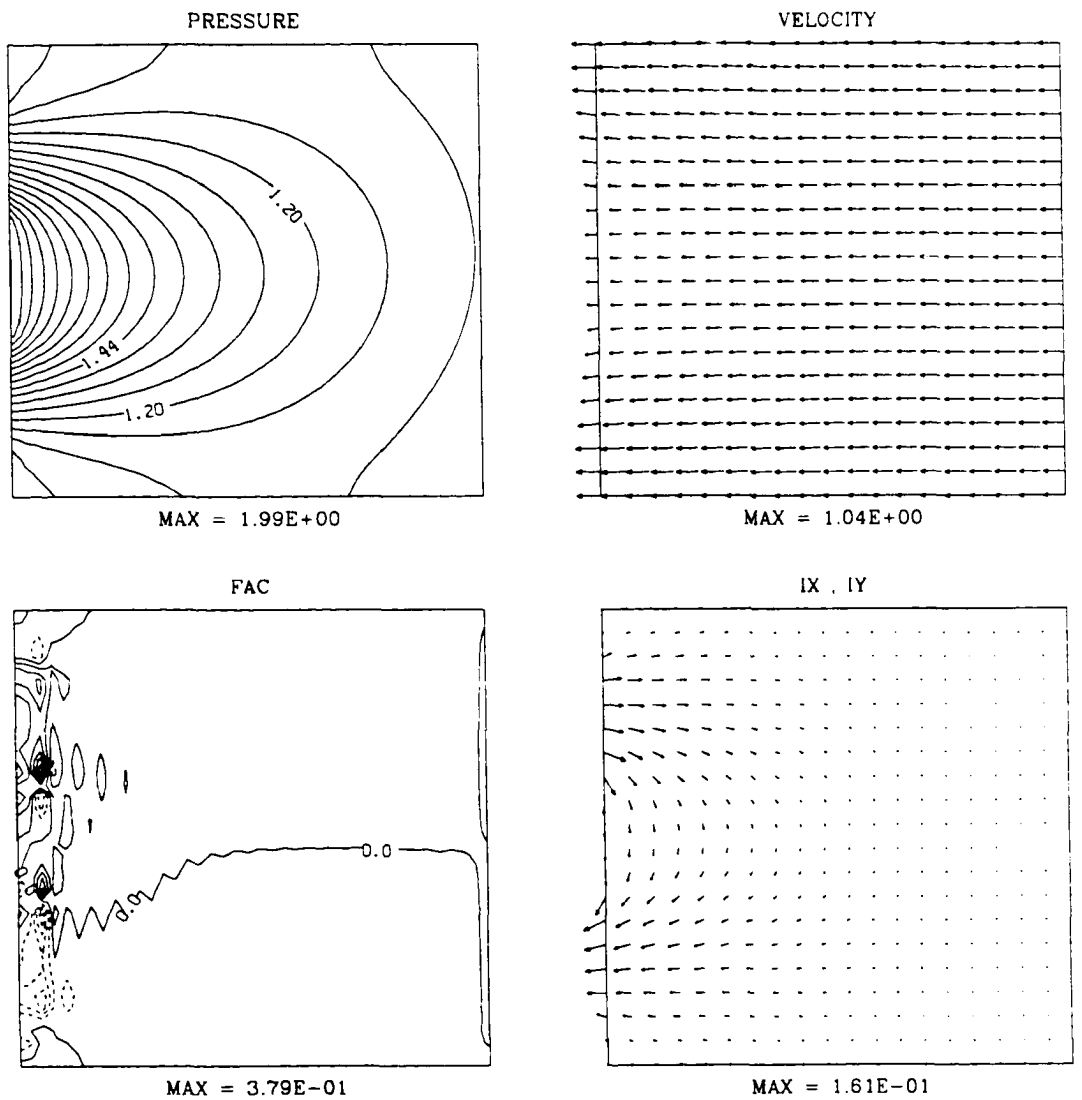

Figure 6–3 (b) 600 time steps ($\tau = 1.97$)

is smooth; the dusk to dawn current does not exist clearly; and there is no field-aligned current system traveling upstream. This is the outstanding difference from the previous cases. After the faint wave propagates outside of the boundary, we have an asymptotic state. The distributions after 600 time steps ($\tau = 1.97$) are very similar to each other, and to Figure 6–1*d*.

The difference of the parameters between Figure 6–1 and Figure 6–3 is only by a factor of 2 in the convection velocity. This small change causes a critical difference in the resultant field-aligned current distribution. If the convection velocity is slower than a certain value, the wave is no longer steepened. The field-aligned currents associated with the wave are very weak (much less than half of Figure 6–1) for both the region 1 type and the region 2 type. Let us consider the enhancement of the plasma sheet convection. The above result implies that the field-aligned current system appears suddenly if the convection exceeds some critical velocity. In other words, the onset of the field-aligned current generation during the substorm depends on how much the convection is enhanced. This critical value is determined in terms of the other physical conditions such as the background pressure, magnetic field, ionospheric conductivity, dawn-dusk extent of the enhanced convection, etc..

The slower convection velocity suppresses the instabilities: we may expect more stable results (as we can expect from the comparison between Figure 6–1 and

Figure 6–2). This is true for the dawn and dusk boundaries.

6–3–3. Effect of Background Magnetic Field

Figures 6–4*a* to 6–4*c* (250, 500 and 1500 time steps, respectively) show the results when the magnetic pressure is halved; i.e., we set $M_A^2 = 0.4$ and $\beta = 1.6$. All the other parameters, including M_S, are the same as in Figure 6–1. The morphological results at 250 time steps ($\tau = 1.03$) are similar to the results of Figure 6–1, e.g., the dawn-dusk asymmetry, existence of the similar wave, and the similar pattern of the field-aligned current distribution. Since the wave is the MHD fast mode, the difference in the magnetic pressure does not affect the propagation speed, which is essentially determined by M_S^2.

However, we can point out some minor difference from Figure 6–1 if we compare at 500 time steps ($\tau = 2.05$). The simulated wave propagates slightly slower in the present case. Since only the Alfvén velocity is different (C_S is the same), the MHD fast mode wave simulated here is slightly coupled to the Alfvén mode. This coupling is already implied from that fact that the wave is accompanied by the strong field-aligned currents. The lower Alfvén velocity suppresses the wave propagation velocity. Another difference is found in the wake like structure. They are much weaker in the present case, and hence, the simulation is numerically stable near the boundaries.

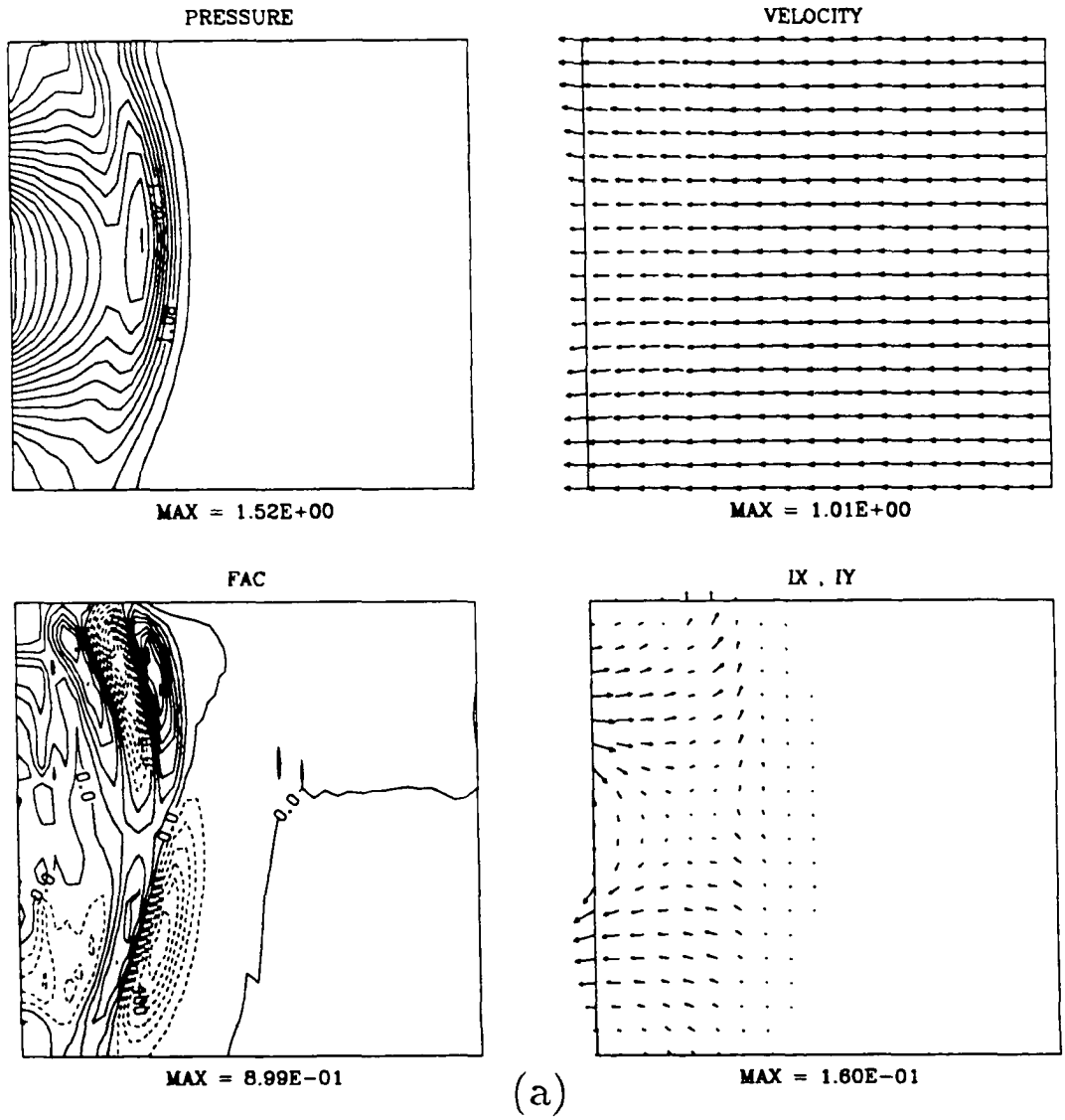

Figure 6–4. Numerical results when $M_A^2 = 0.4$ and $\beta = 1.6$. The magnetic pressure is halved. All the other parameters, including M_S, are the same as in Figure 6–1. Results at (a) 250 time steps, (b) 500 time steps, and (c) 1500 time steps are listed.

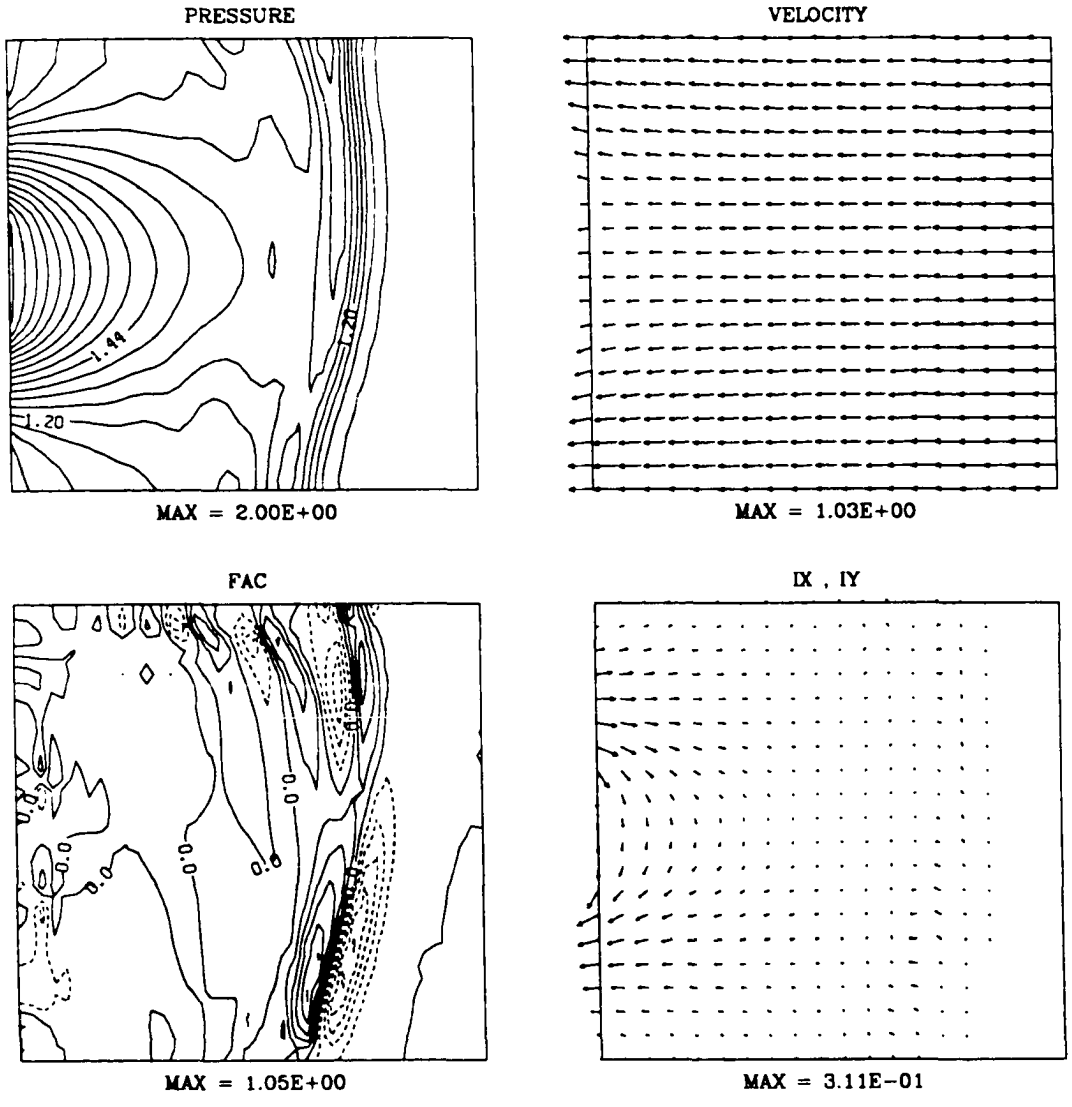

Figure 6–4 (b) 500 time steps ($\tau = 2.05$)

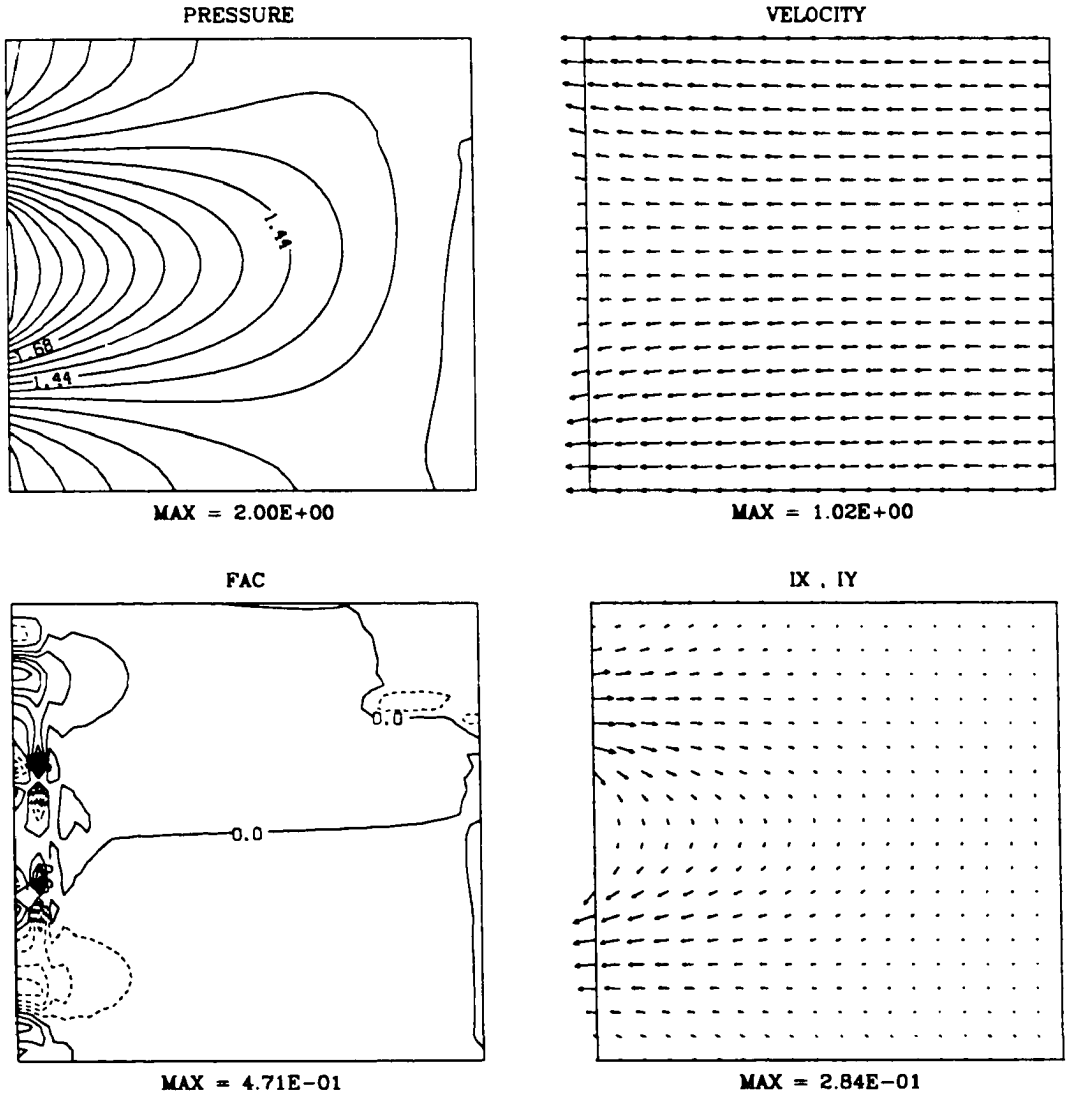

Figure 6–4 (c) 1500 time steps ($\tau = 6.08$)

Even though the morphologies are similar between Figure 6–1 and Figure 6–4, the values of the plasma sheet currents are different. There is a factor of 2 difference for the plasma sheet current at 1500 time steps between Figure 6–1 and Figure 6–4 ($\tau = 6.08$). The field-aligned current intensity associated with the wave shows a factor of $\sqrt{2}$ difference as is obtained from result at 100 time steps ($\tau = 0.41$). Let us interpret the factor of 2 by looking at the momentum equation (6·1). In the asymptotic state, the first term and the second term on the right hand side of (6·1) have to be balanced:

$$\frac{\beta}{2}\nabla^*_{x,y}\pi^* = \frac{L_0}{h_0}\mathbf{I}^*_{x,y} \times \mathbf{B}^*_z$$

The normalized pressures in the figures are the same. Hence, the difference in β has to be the same as the difference in the $\mathbf{I} \times \mathbf{B}$ force. Since B^*_z does not change from its original value = 1, the difference in $I^*_{x,y}$ compensate the difference of β between Figure 6–1 ($\beta = 0.8$) and Figure 6–4 ($\beta = 1.6$). Therefore, the asymptotic plasma sheet current is twice as large in Figure 6–4 as in Figure 6–1.

Figures 6–5*a* and 6–5*b* (100 and 250 time steps, respectively) show the results when the magnetic pressure is doubled from Figure 6–1 instead of halved as in the previous case. We set $M_A^2 = 0.1$ and $\beta = 0.4$, and keep all other parameters the same as in Figure 6–1 and Figure 6–4. Some of the present results are consistent with what are expected from the above discussion for the previous results.

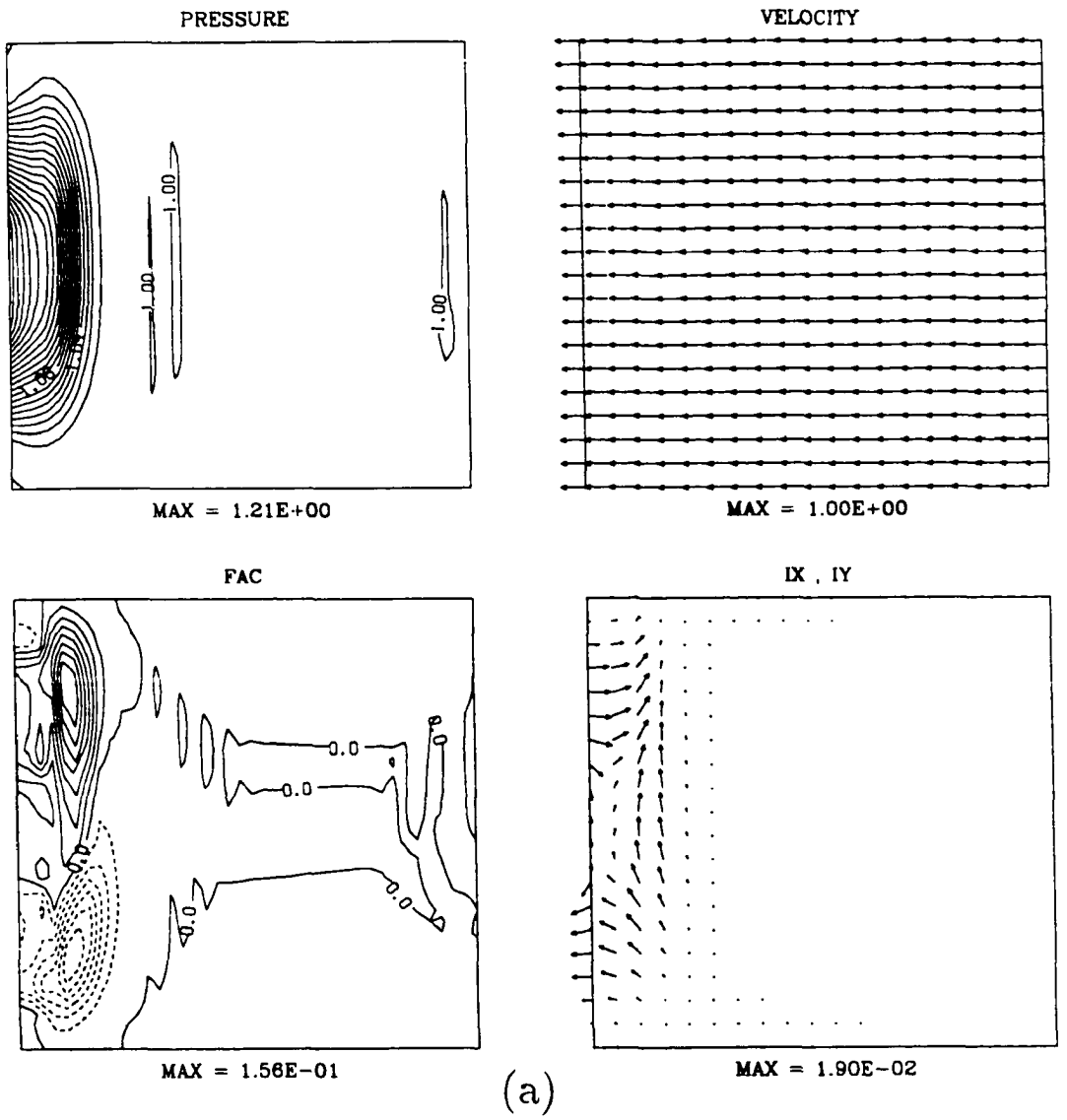

Figure 6–5. Numerical results when $M_A^2 = 0.1$ and $\beta = 0.4$. The magnetic pressure is doubled from Figure 6–1 instead of halved in the previous case. We keep all other parameters the same as in Figure 6–1 and Figure 6–4. Results at (a) 100 time steps and (b) 250 time steps are listed.

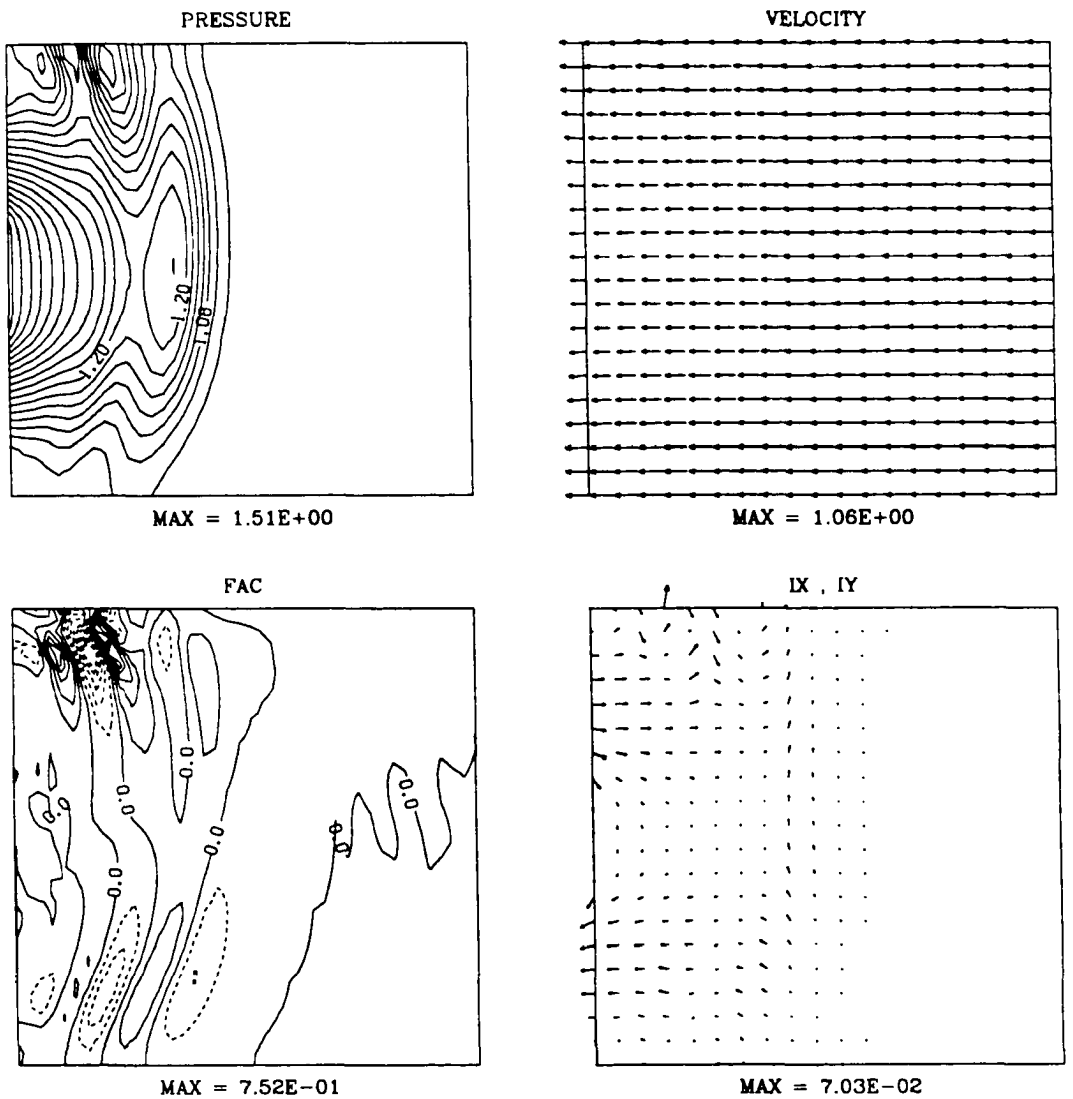

Figure 6–5 (b) 250 time steps ($\tau = 1.03$)

1. We have the MHD fast mode wave with a similar but slightly faster propagation velocity compared to Figure 6–1 because of the larger Alfvén velocity. *2.* The current intensity of the accompanied field-aligned currents at 100 time steps ($\tau = 0.41$) is smaller in Figure 6–5 than in Figure 6–1 by a factor of $\sqrt{2}$. *3.* The wake-like structure (or numerical noise) exist more clearly. *4.* The numerical instability is more severe, so that the result is not reliable after 250 time steps ($\tau = 1.03$). This severe numerical instability is introduced at the wakes of the wave, and is amplified at the dawn boundary. It breaks down the simulation itself before it reaches the asymptotic state. The wake phenomenon is numerically unstable when it hits the boundary.

Let us compare the effect of C_S (or M_S) and the effect of V_A (or M_A). The present results are similar to Figure 6–1 (the only difference is the V_A value) rather than Figure 6–3 (the only difference is C_S value) except for the wake structure. If we reduce M_S^2 to 0.25, the same as in Figure 6–3, while we keep M_A^2 the same as in Figure 6–1 (= 0.2), again the wave is not well developed as is shown in Figures 6–6*a* (300 times steps) and 6–6*b* (600 time steps).

Thus, the sound speed, not the Alfvén speed, is important for the wave generation and its propagation. On the other hand, the parameter M_A or β, not the sound speed, might be important for the formation of wake behind the wave. This

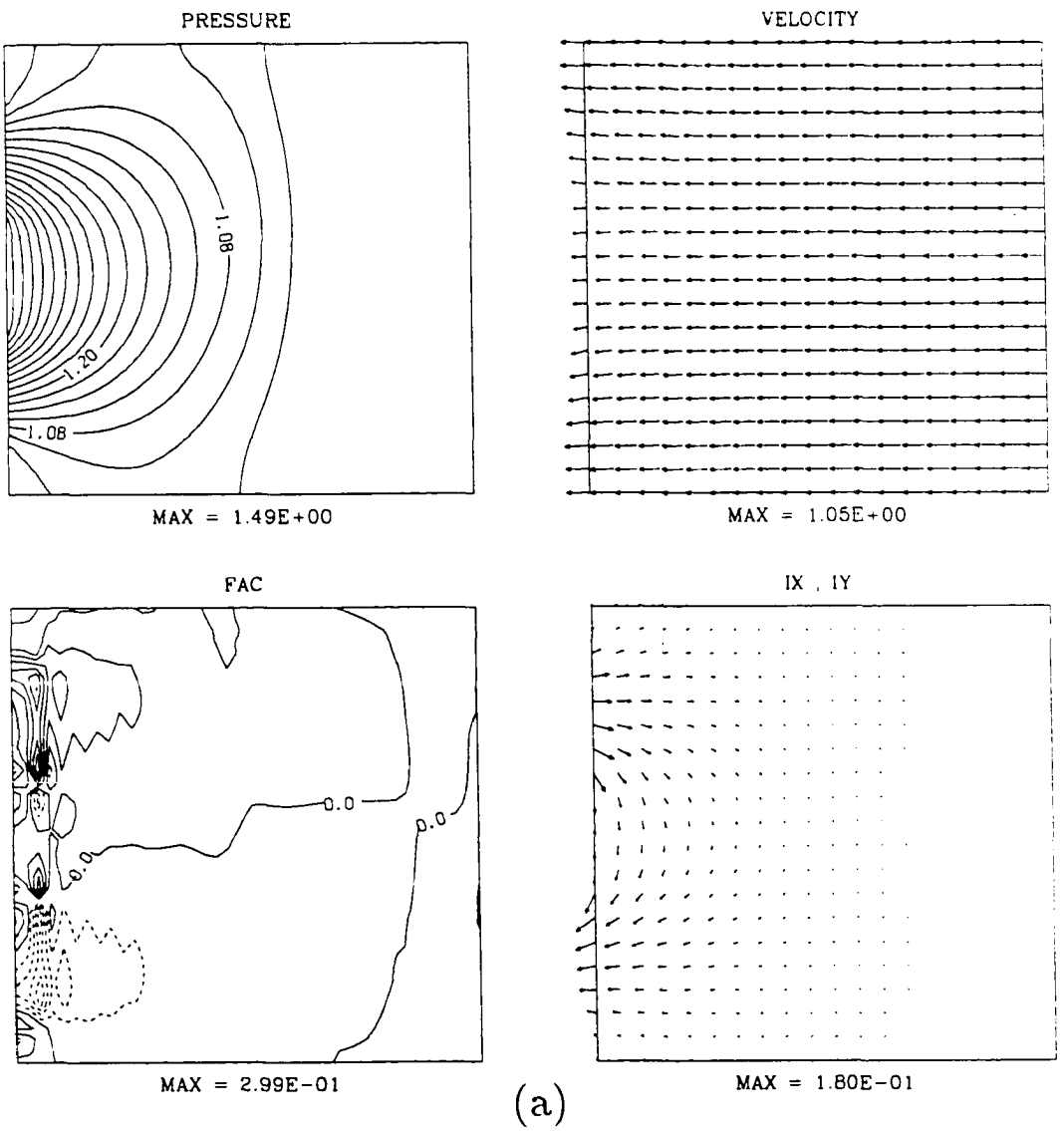

Figure 6–6. Numerical results when $M_S^2 = 0.25$ and $\beta = 1.6$. We keep all other parameters the same as in Figure 6–1. Results at (a) 300 time steps and (b) 600 time steps are listed.

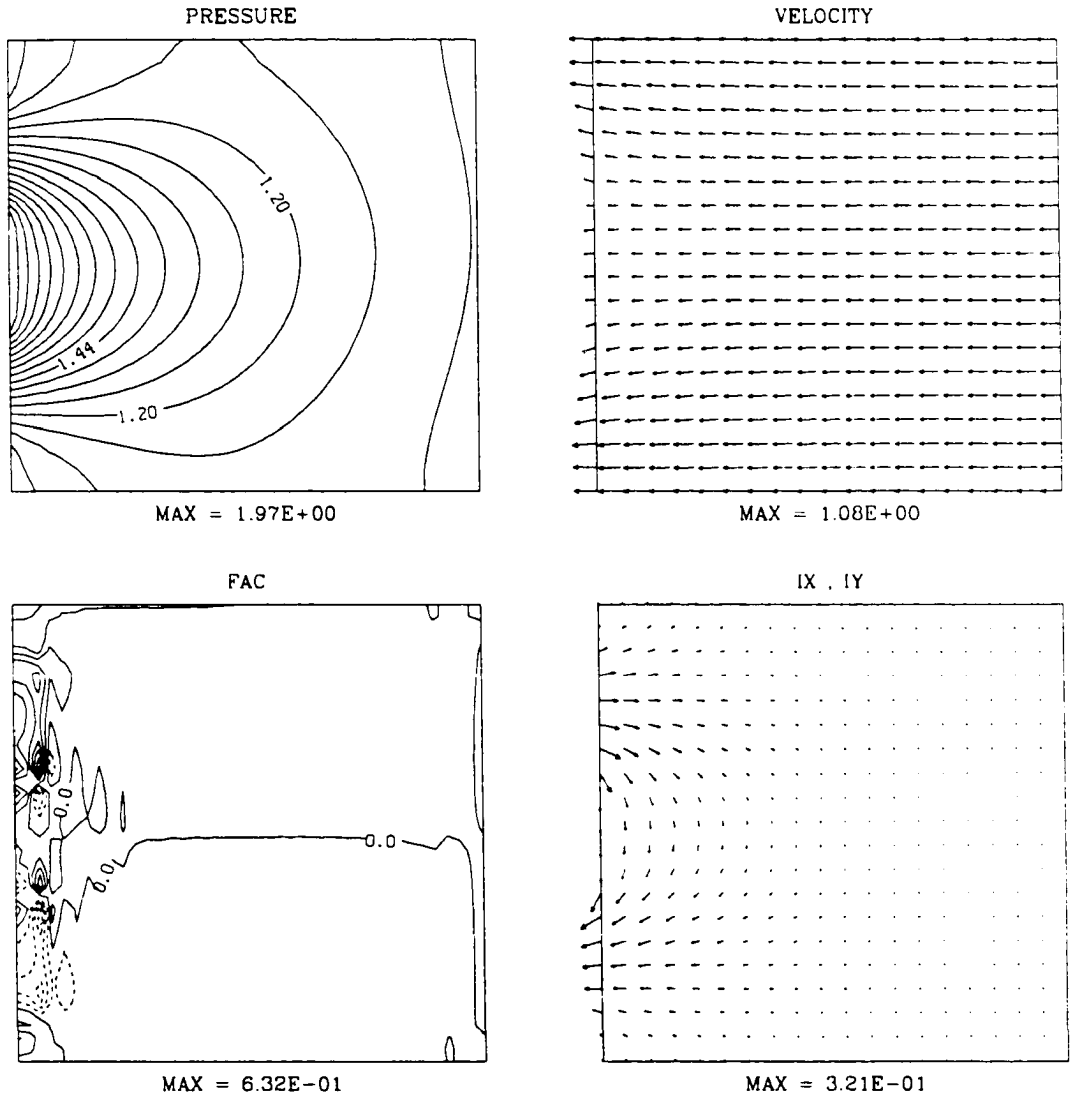

Figure 6–6 (b) 600 time steps ($\tau = 1.94$)

is also supported from the comparison between Figure 6–6*a* and Figure 6–3*a* as well as the comparison among Figures 6–1, 6–4, and 6–5.

6–3–4. Effect of Adiabatic Compression

Next, we examine the effect of γ. Figures 6–7*a* (300 time steps) and 6–7*b* (600 time steps) show the results when we set $\gamma = 2.0$ instead of unity; i.e., an adiabatic case instead of an isothermal case. All the other parameters are the same as in Figure 6–1. The morphological result is between those of Figure 6–1 and Figure 6–3.

At 300 time steps ($\tau = 0.99$), the wave is wide-spread and is barely recognizable; it is not well developed, and it smears away as it propagates. The intensity of the field-aligned currents at the front of the propagation is less than half that of Figure 6–1. The other quantities are very similar to those of Figure 6–3. The asymptotic state at 20 time steps ($\tau = 1.97$) is also similar to Figure 6–3*b*. Since Figure 6–3 demonstrates a slow convection case, the ratio of the plasma pressure to the kinetic pressure is high compared to Figure 6–1. This is also the case with Figure 6–7 because the pressure increase rate is more than doubled, which causes substantial change in M_S from its initial value. The M_S value decreases as the higher pressure moves upstream. Thus, the kinetic and the plasma pressure balance is important for the wave formation.

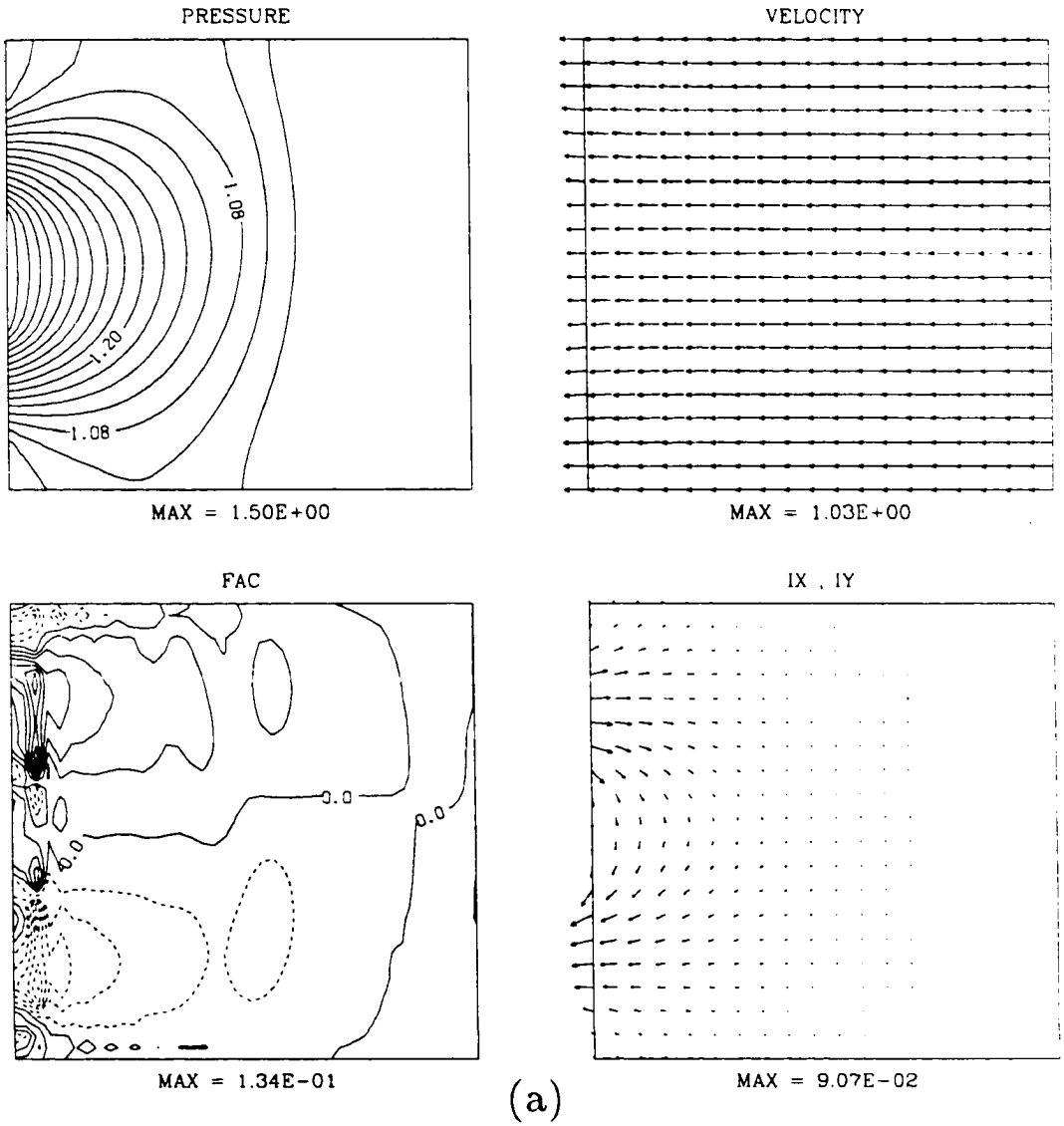

Figure 6–7. Numerical results when $\gamma = 2.0$ instead of unity. This is an adiabatic case instead of an isothermal case. All the other parameters are the same as in Figure 6–1. Results at (a) 300 time steps and (b) 600 time steps are listed.

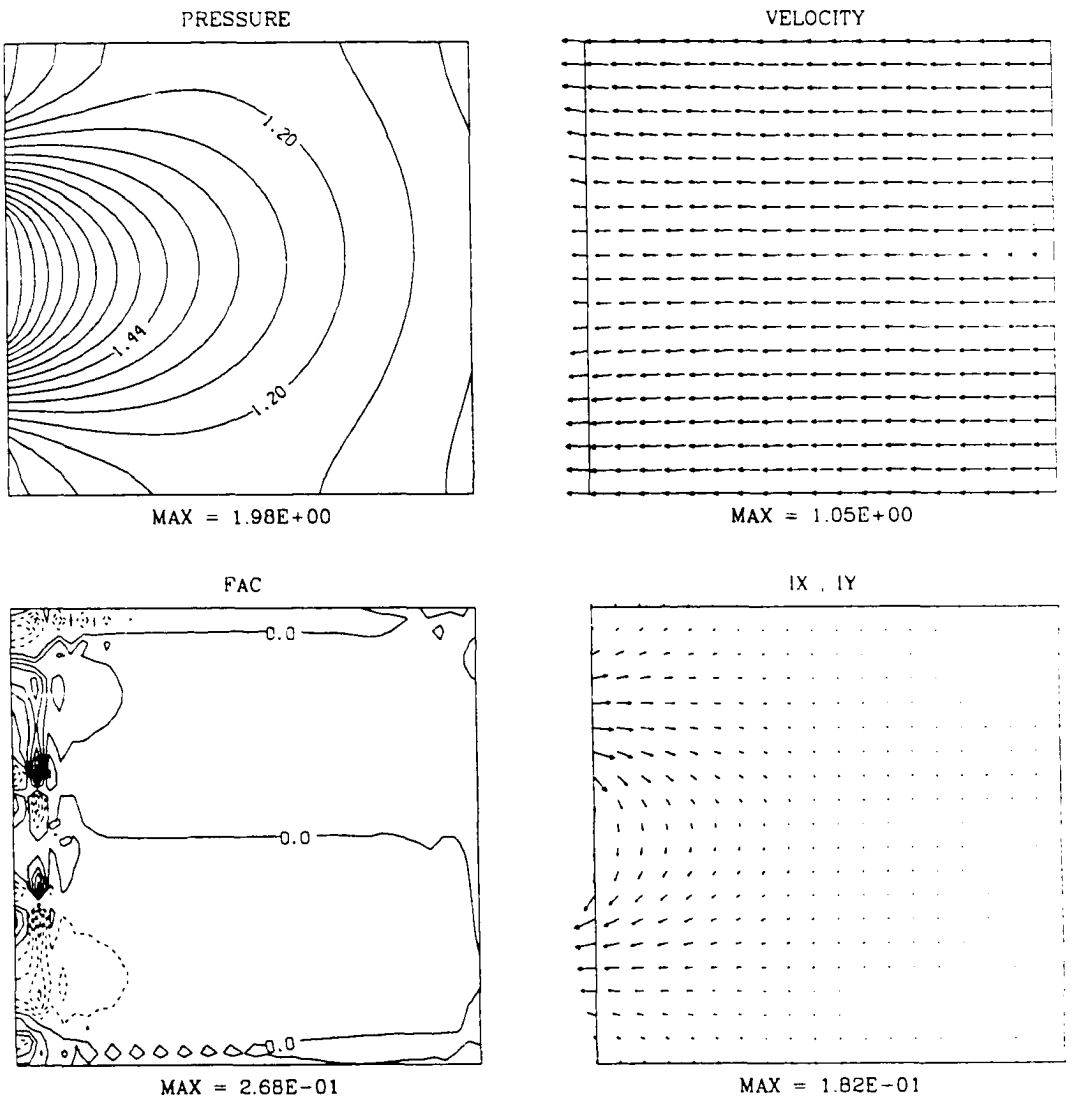

Figure 6–7 (b) 600 time steps ($\tau = 1.97$)

6–3–5. Effect of Ionospheric Conductivity

Now, we examine the effect of the ionospheric conductivity; i.e., the effect of different (but still uniform) η. Figures 6–8*a* (100 time steps) and 6–8*b* (250 time steps) show the results when the ionospheric conductivity is larger than in Figure 6–1 by a factor of 5 ($\eta = 0.2$). All the other parameters are the same as in Figure 6–1; i.e., $M_A^2 = 0.2$, $M_S^2 = 0.5$ ($\beta = 0.8$), $\gamma = 1.0$, $\Sigma_H^* = 0.5$, and $\xi_x/\xi_y = 1$.

Let us compare Figure 6–1 and Figure 6–8 for 50 times steps ($\tau = 0.41$). Even though M_S and M_A, respectively, are the same as in Figure 6–1, the wave propagation velocity is apparently faster in the present case. However, the quantities associated with the wave are similar; e.g., the dusk to dawn current intensity, and the field-aligned current density on the wave. As suggested from the previous cases (Figure 6–1 through Figure 6–7) the wave steepens less if its propagation is faster in the simulation box's reference frame. This implication also holds in the present case. This result suggests the role of ionospheric resistance: the wave propagates faster if the medium is more rigid and the wave propagates slower if the medium is more viscous. Since the conductivity is high, we do not have strong 'viscosity' in the present case.

The numerical instability originating from the wake-like structure at the outflow boundary dominates as early as 250 time steps ($\tau = 1.03$). This instability is already recognizable at 100 time steps ($\tau = 0.41$). A larger value of the ionospheric

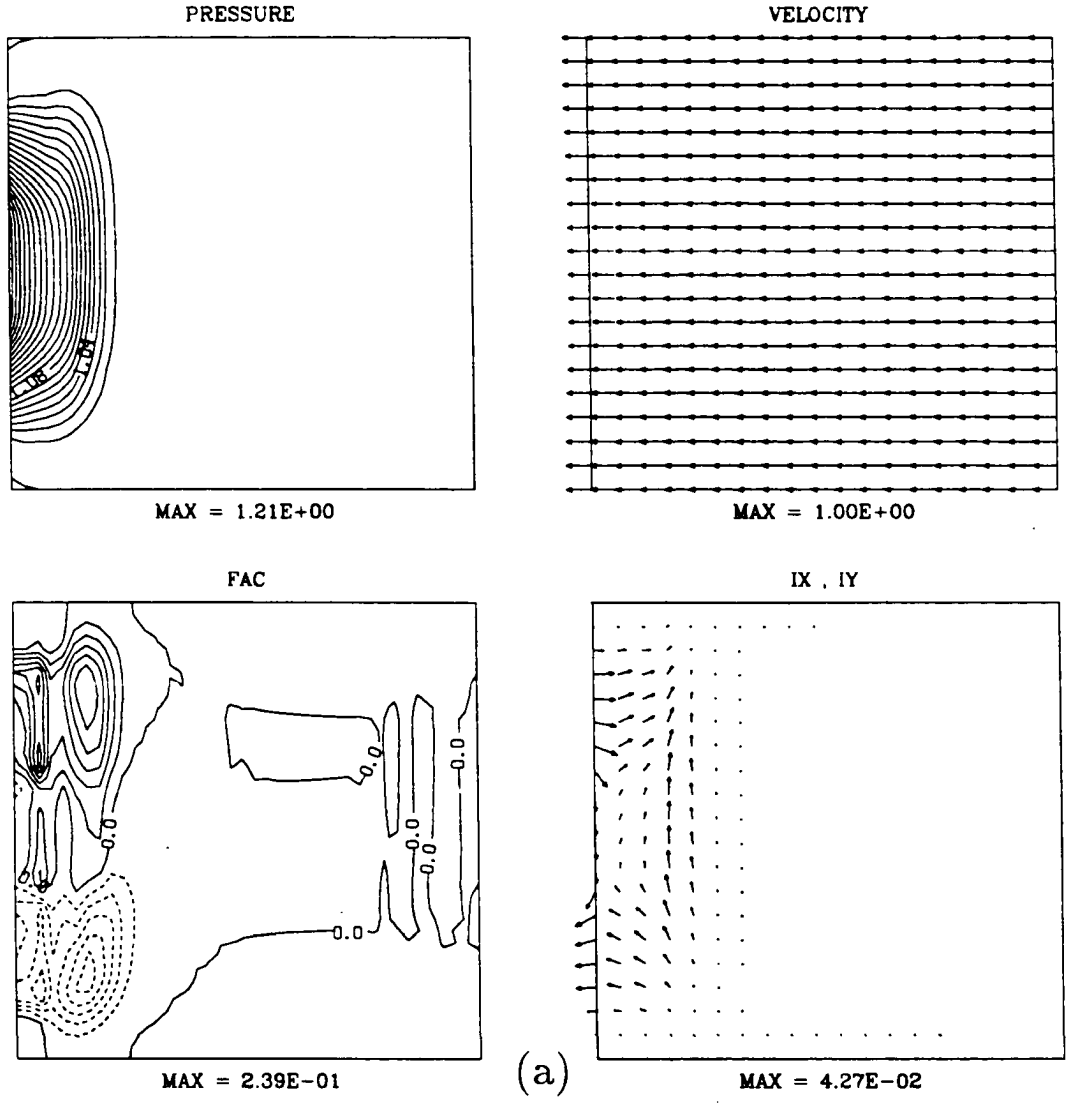

Figure 6–8. Numerical results when $\eta = 0.2$ instead of unity. The ionospheric conductivity is larger than in Figure 6–1 by a factor of 5. All the other parameters are the same as in Figure 6–1; i.e., $M_A^2 = 0.2$, $M_S^2 = 0.5$ ($\beta = 0.8$), $\gamma = 1.0$, $\Sigma_H^* = 0.5$, and $\xi_x/\xi_y = 1$. Results at (a) 100 time steps and (b) 250 time steps are listed.

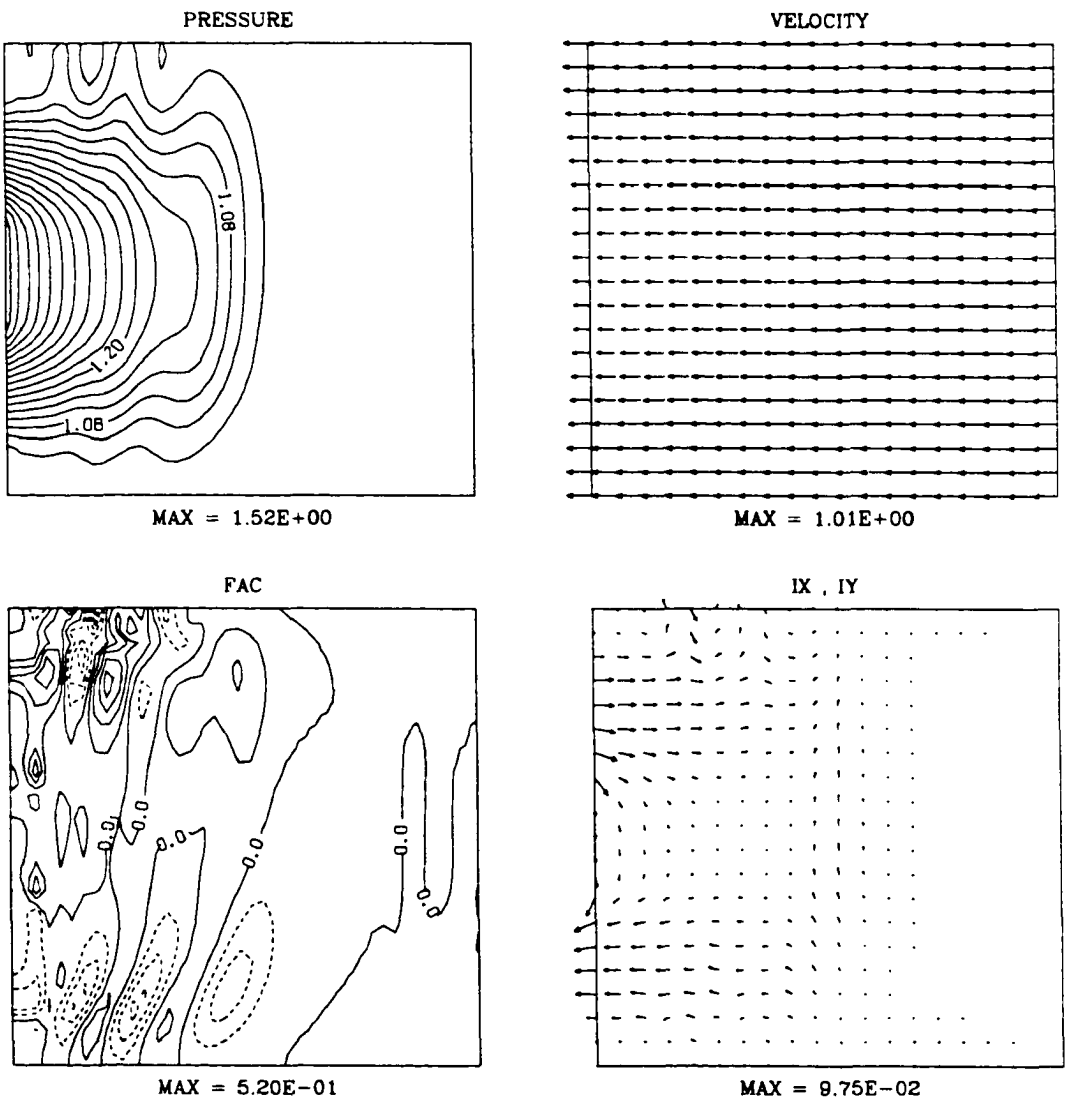

Figure 6–8 (b) 250 time steps ($\tau = 1.03$)

conductivity means smaller dissipation, which might cause the instability. This result suggests the effect of artificial resistivity in the regular MHD simulation code [e.g., *Miura*, 1985].

The opposite case is also examined. Figures 6–9*a* to 6–9*c* (100, 250, and 500 time steps, respectively) show the results when $\eta = 5.$; i.e., the ionospheric conductivity is 5 times smaller than in Figure 6–1. All the other parameters are the same as in Figure 6–1 and Figure 6–8. The wave propagation speed at 100 time steps ($\tau = 0.41$) is slightly slower than that of Figure 6–1. This difference is not as obvious as in the previous case, i.e., between Figure 6–1 and Figure 6–8, which suggests that the result of Figure 6–9 cannot easily implied from the previous results.

The wave-associated current and, especially, field-aligned currents are weaker (nearly half) than in Figure 6–1. The ratio of the field-aligned current intensity in Figure 6–9 to in Figure 6–1 is not 5, but nearly 2. Note that the field-aligned current intensities are similar between Figure 6–1 and Figure 6–8. The field-aligned current intensity at the ionosphere is not proportional to the ionospheric conductivity even though the plasma sheet conditions are the same. The plasma sheet also regulates the ionospheric current. While the plasma sheet current in Figure 6–9*a* decreases from Figure 6–1*a* by a factor of 1.8, the decrease of field-aligned current intensity near the wave is by a factor of 2.3. The wave-associated

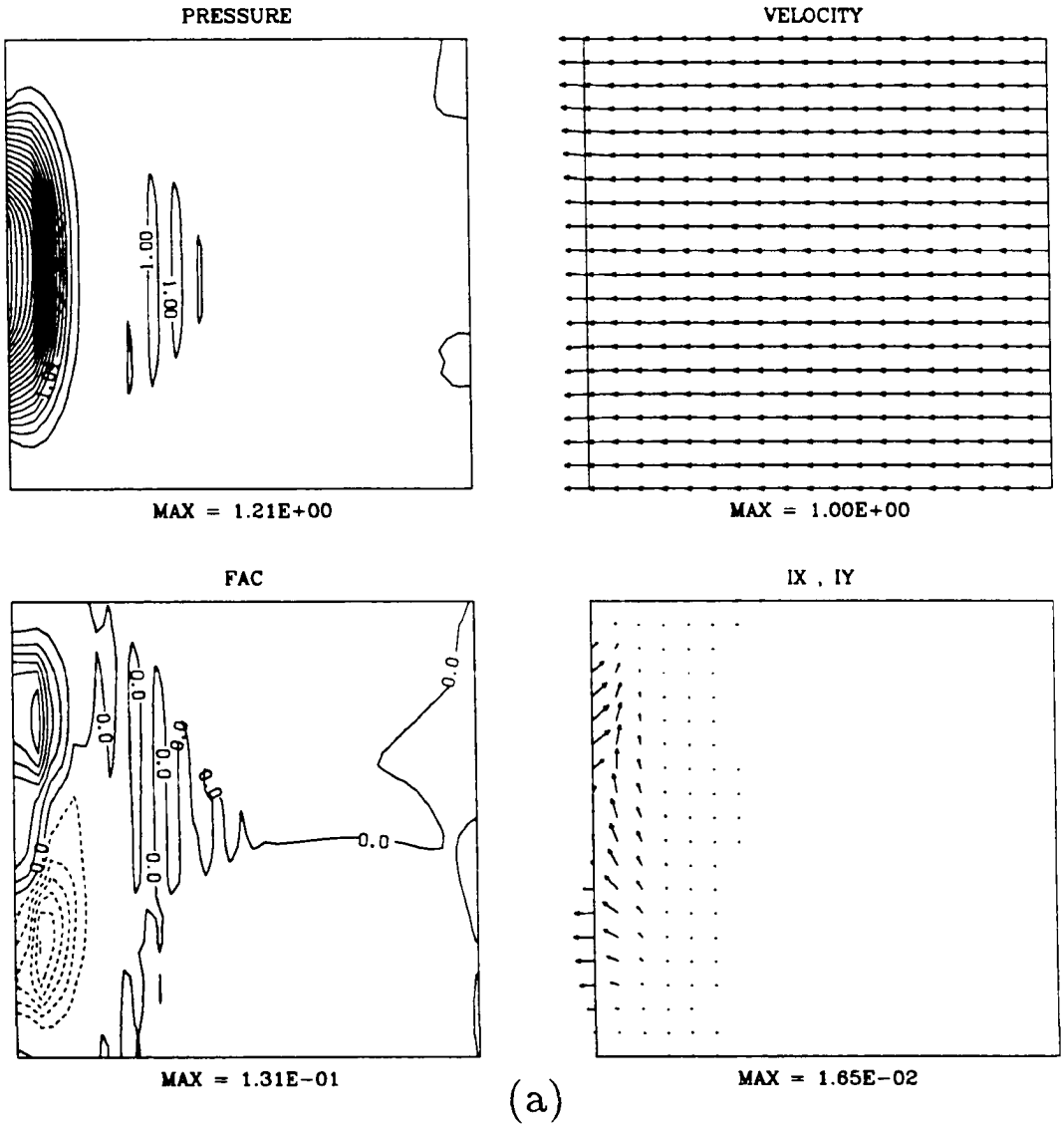

Figure 6–9. Numerical results when $\eta = 5.0$. The ionospheric conductivity is 5 times smaller than in Figure 6–1. All the other parameters are the same as in Figure 6–1 and Figure 6–8. Results at (a) 100 time steps, (b) 250 time steps, and (c) 500 time steps are listed.

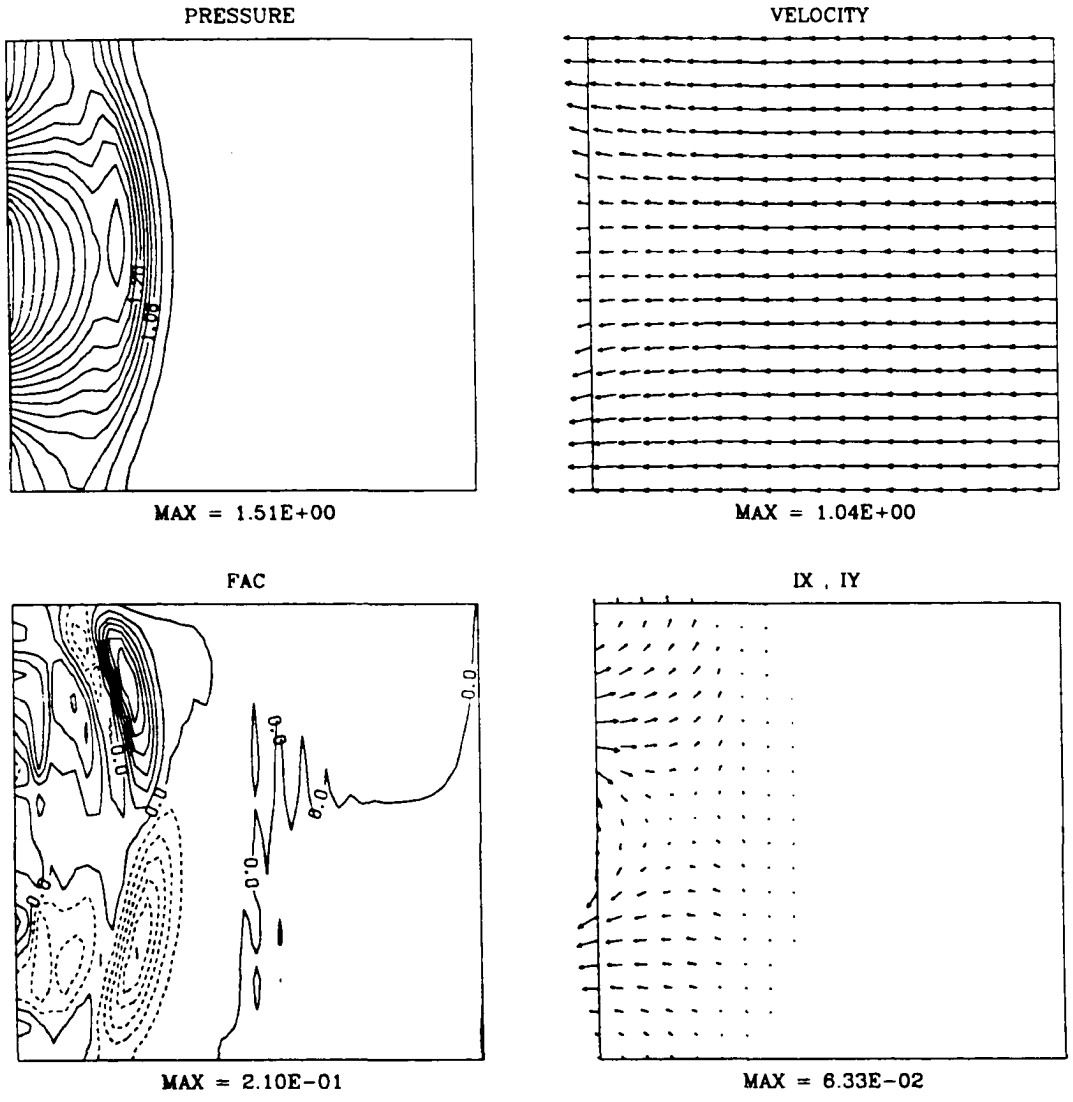

Figure 6–9 (b) 250 time steps ($\tau = 1.03$)

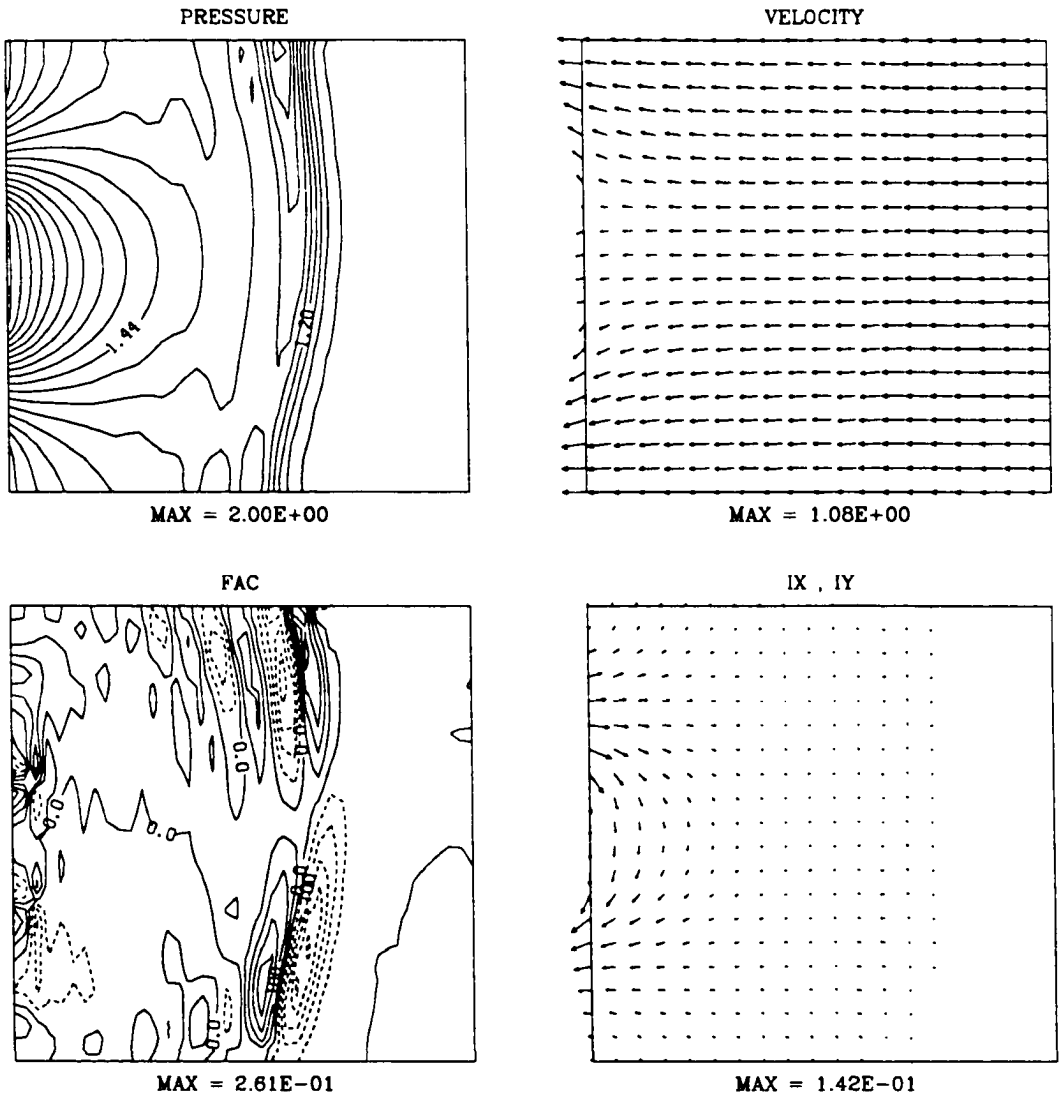

Figure 6–9 (c) 500 time steps ($\tau = 2.02$)

current decreases more than the closed part of the current in the plasma sheet. Thus, the ionosphere current decreases more in Figure 6–9.

The wave structure is also different from Figure 6–1. The second pair (region 2 type) of field-aligned currents is absent at 250 time steps ($\tau = 1.03$). It appears at 500 time steps ($\tau = 2.02$). The wave does not have many structures behind it as this result indicates. This result also holds for the wake: there is no apparent wake-like structure behind the wave.

Let us study the effect of the Hall conductivity by changing the ratio of the Hall conductivity to the Pedersen conductivity. Figures 6–10*a* (250 time steps) and 6–10*b* (1500 time steps) show the results when $\Sigma_H^* = 0$. All the other parameters are the same as in Figure 6–1. Since the ionospheric dissipation is related to the Pedersen conductivity, the main feature has to be the same.

At 250 time steps ($\tau = 1.03$), we again see the generation of the MHD fast mode wave accompanied by two pairs of field-aligned currents. The propagation speed and the field-aligned current intensities are similar to those of Figure 6–1. Both figures contain the wake structures behind the wave. The morphology and values at the asymptotic state at 1500 time steps ($\tau = 6.19$) are also very similar to the case of Figure 6–1. However, all panels are essentially dawn-dusk symmetric in Figure 6–10. Thus, the asymmetry in Figure 6–1 is caused by the ionospheric Hall current.

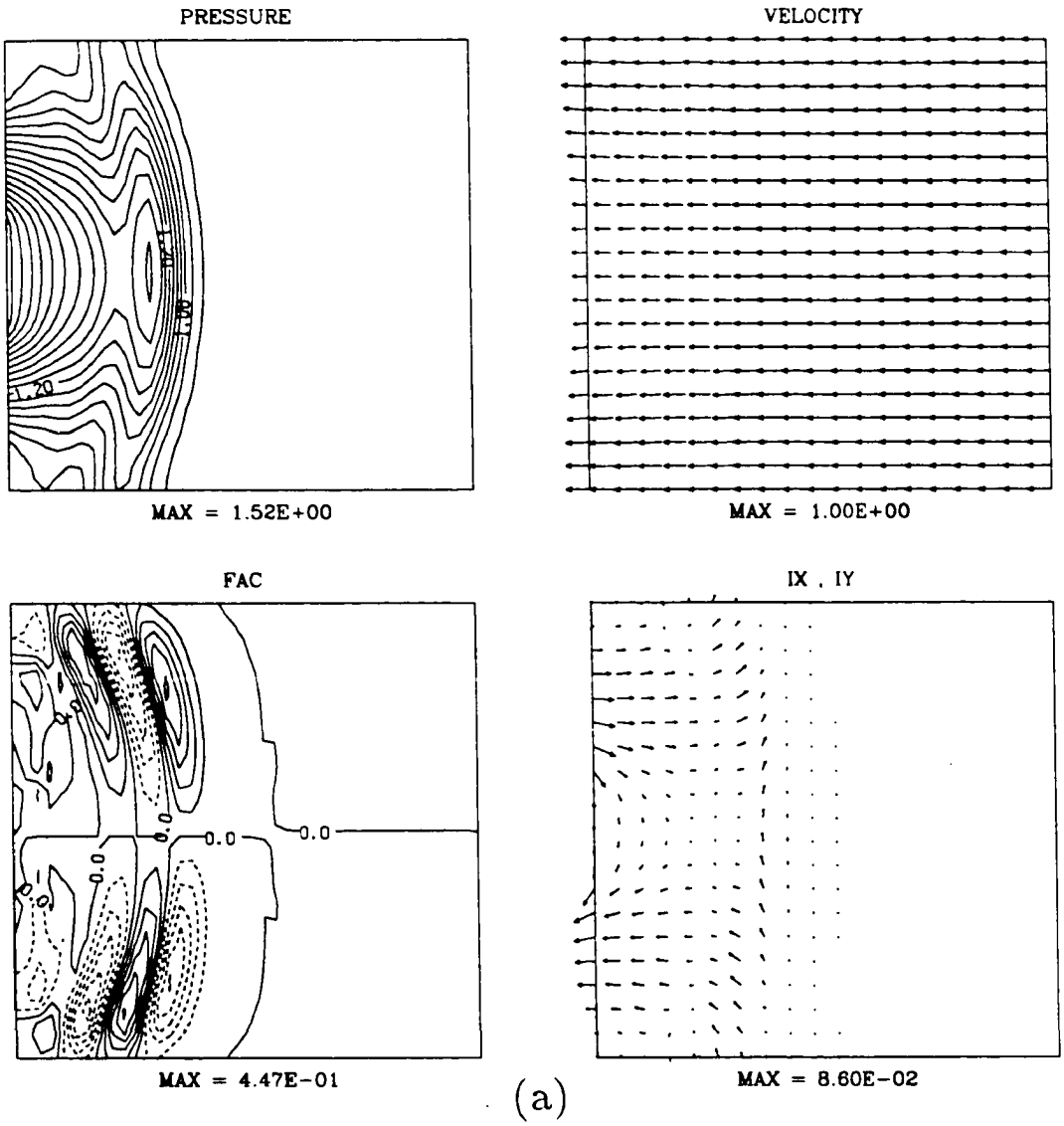

Figure 6–10. Numerical results when $\Sigma_H^* = 0$. All the other parameters are the same as in Figure 6–1. Results at (a) 250 time steps and (b) 1500 time steps are listed.

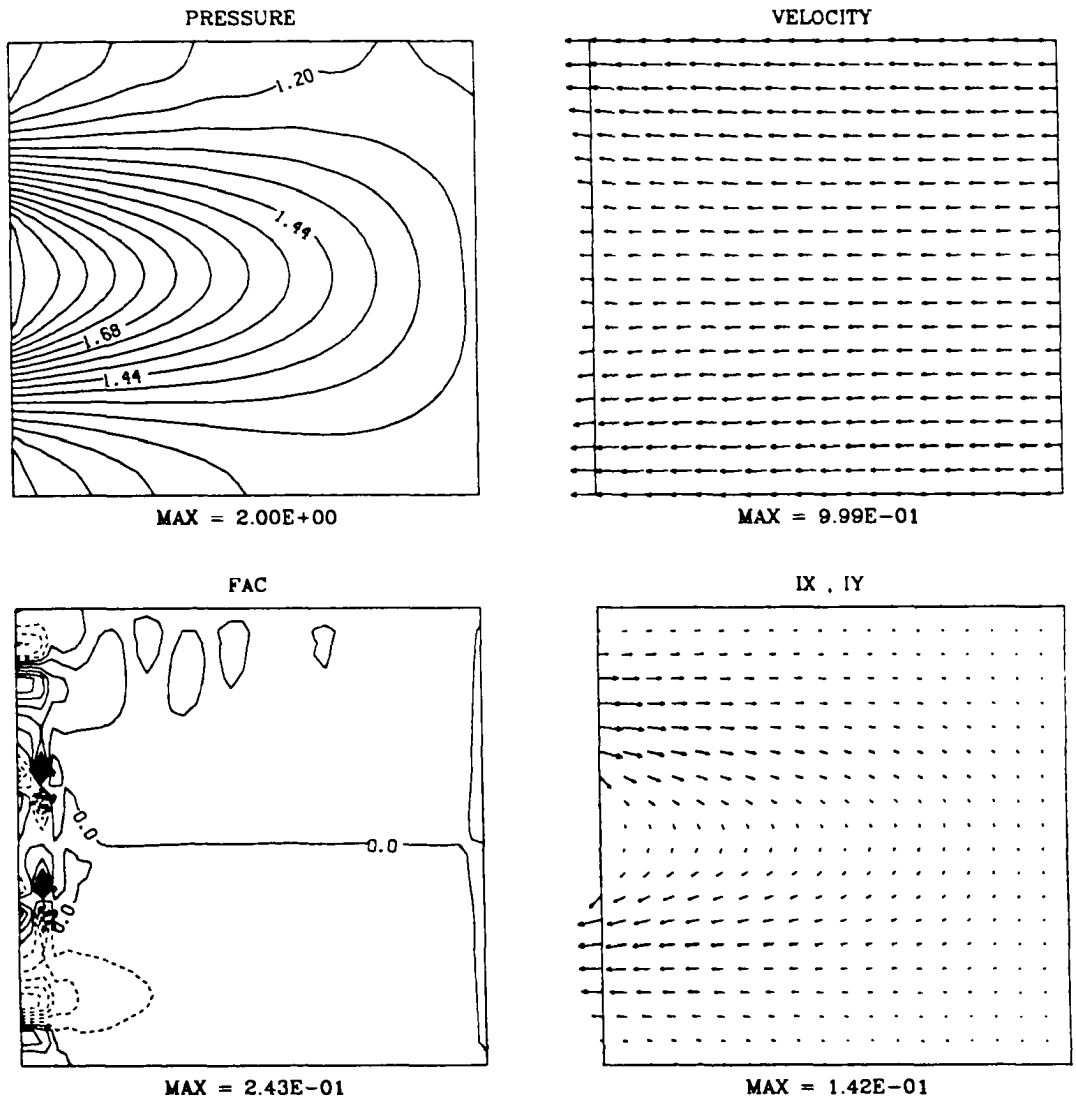

Figure 6–10 (b) 1500 time steps ($\tau = 6.19$)

The ionospheric $\mathbf{I}_H \times \mathbf{B}$ force is asymmetric in the dawn and the dusk directions if the magnetospheric convection is sunward as shown in Figure 2–3. Its reaction force is also asymmetric, and it is transmitted to the plasma sheet, causing the asymmetry. In fact, the ionospheric Hall current causes the phase shift when the incident Alfvén wave is reflected at the ionosphere. This phase shift causes the rotation of the the electric field, and hence, the rotation of the convection direction from its original symmetric direction in the plasma sheet. Since the Alfvén wave transition time is assumed zero between the ionosphere and the plasma sheet, the asymmetric reaction force is transmitted to the plasma sheet simultaneously.

For the MHD fast mode wave in Figure 6–1, the ionospheric Hall current (i.e., its closure $\mathbf{I}^{\mathbf{i}}_{x,y}$) is stronger on the wave. The direction of such a current in the plasma sheet is in the -x direction (tail to earth), enhancing the field-aligned currents on the dusk side and reducing the field-aligned currents on the dawn side. This is why we have more intense field-aligned currents on the dusk side of the wave. Note that this discussion holds where the amplitude change is the greatest, i.e., on the wave, but not the wake. If we map this result to the ionosphere, the field-aligned current intensity is greater in the premidnight sector, which is is consistent with the ionospheric observations.

6–3–6. Effect of Geomagnetic Field Configuration

Finally, we examine the geometrical effect of the mapping. Among many complicated geometric factors, we only consider the difference between $\xi_x = \partial x_i/\partial x$ and $\xi_y = \partial y_i/\partial y$; i.e., how much the geomagnetic field converges from the plasma sheet to the ionosphere. Since the plasma sheet is stretched in the day–night (x) direction, we normally have a situation that $\xi_x < \xi_y \ll 1$. However, we study both $\xi_x/\xi_y = 2$ and $\xi_x/\xi_y = 0.5$ cases.

Figures 6–11*a* (100 time steps) and 6–11*c* (250 time steps) show the results when $\xi_x/\xi_y = 2$. All the other parameters are the same as in Figure 6–1; i.e., $\eta = 1$, $\Sigma_H^* = 0.5$, $\gamma = 1.0$, $M_A^2 = 0.2$, and $M_S^2 = 0.5$ ($\beta = 0.8$). The distributions at 100 time steps ($\tau = 0.41$) are very similar to those of Figure 6–1: a similar wave with a similar propagation speed, and similar field-aligned currents.

The similarity is also found for 250 time steps ($\tau = 1.03$) with commonly existing wake-like structures even though it could be numerical noise. However, we can point out some minor differences. The intensity of the field-aligned current at 100 time steps is different from in Figure 6–1 by a factor of 1.5.

We have a more severe instability in the present case. We can attribute it to the increase of the convection velocity; the velocity is doubled if we observe it in the ionosphere. Thus, this situation might correspond to a low η case. In fact, the morphological features are similar between Figure 6–11 and Figure 6–8, even though there are still minor differences, especially for the current intensities.

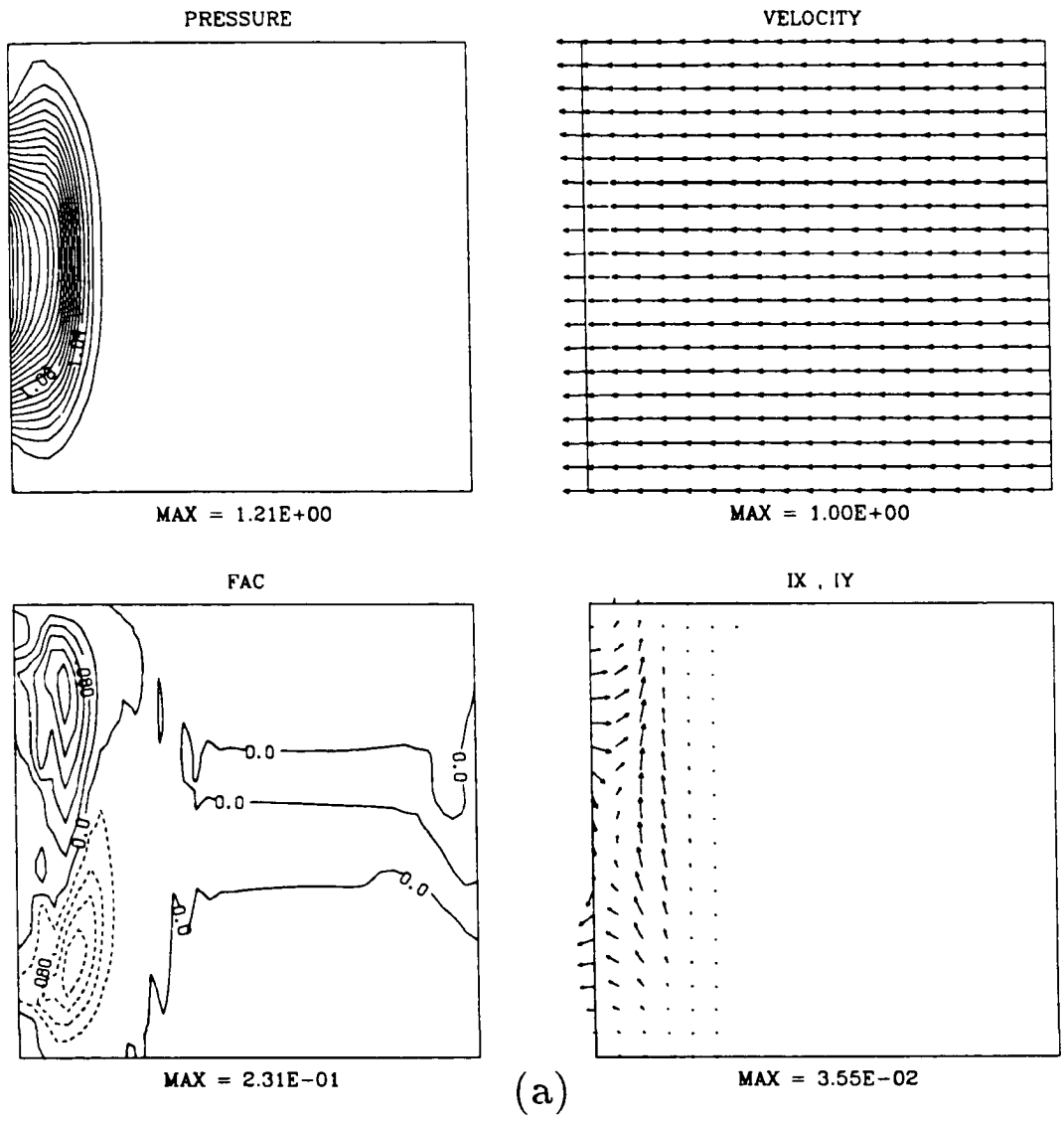

Figure 6–11. Numerical results when $\xi_x/\xi_y = 2.0$ instead of unity. All the other parameters are the same as in Figure 6–1; i.e., $\eta = 1$, $\Sigma_H^* = 0.5$, $\gamma = 1.0$, $M_A^2 = 0.2$, and $M_S^2 = 0.5$ ($\beta = 0.8$). Results at (a) 100 time steps and (b) 250 time steps are listed.

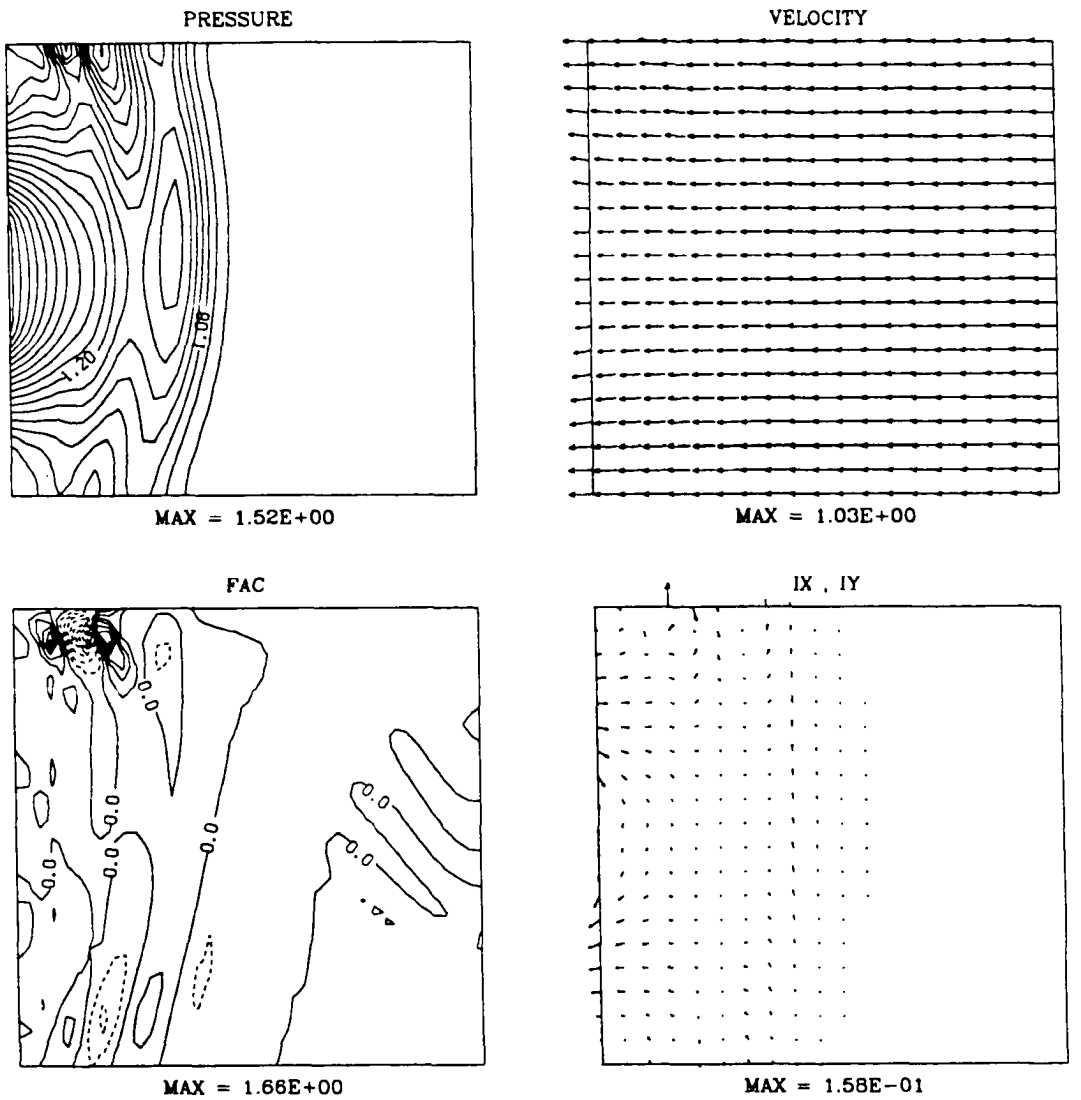

Figure 6–11 (b) 250 time steps ($\tau = 1.03$)

Contrary to the previous case, we set $\xi_x/\xi_y = 0.5$ and keep all the other parameters the same as in Figure 6–1 or Figure 6–11. The results are shown in Figures 6–12a to 6–12c (250, 500, and 1500 time steps). If we apply the above discussion of the effective ionospheric conductivity, this case corresponds to a larger η case such as in Figure 6–9. This is true only for the morphology of the wave; e.g., there is less wake-like structure behind the wave, slightly slower propagation speed, and a similar field-aligned current distribution except its intensity. These features are found at both 250 time steps ($\tau = 1.03$) and at 500 time steps ($\tau = 2.06$).

However, as also mentioned above in Figure 6–11, the quantitative details are different. This wave steepens more, and carries slightly more intense field-aligned currents than the wave of Figure 6–1, while Figure 6–9 shows a weak field-aligned current compared to Figure 6–1.

At 1500 time steps ($\tau = 6.13$), the pressure distribution is more stretched toward the night side. This is because the same mapping point of the ionosphere maps more tailward due to the larger ξ_x value. Since the pressure gradient in the x direction is different, the dawn–dusk component of the plasma sheet current is weaker in Figure 6–12 than in Figure 6–1. In this case, $\nabla P \times \mathbf{B}$ has to be smaller.

As we can expected from Figure 6–9, the wake-like structure (or numerical noise) is not well developed, and hence the simulation is numerically stable at the side boundary. Since the wave is well steepened while a wake does not exist

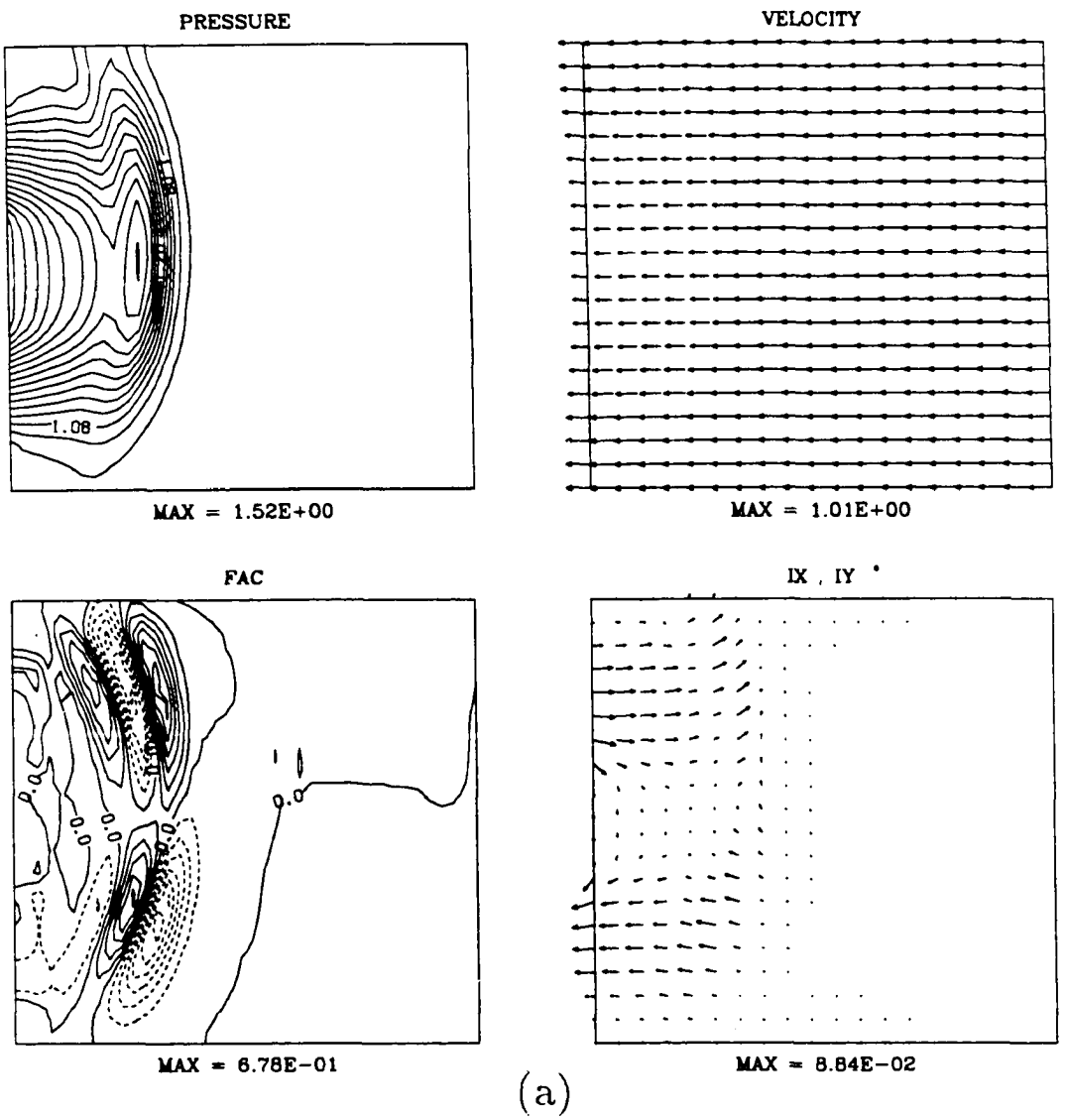

Figure 6–12. Numerical results when $\xi_x/\xi_y = 0.5$. We keep all the other parameters the same as in Figure 6–1 or Figure 6–11. Results at (a) 250 time steps, (b) 500 time steps, and (c) 1500 time steps are listed.

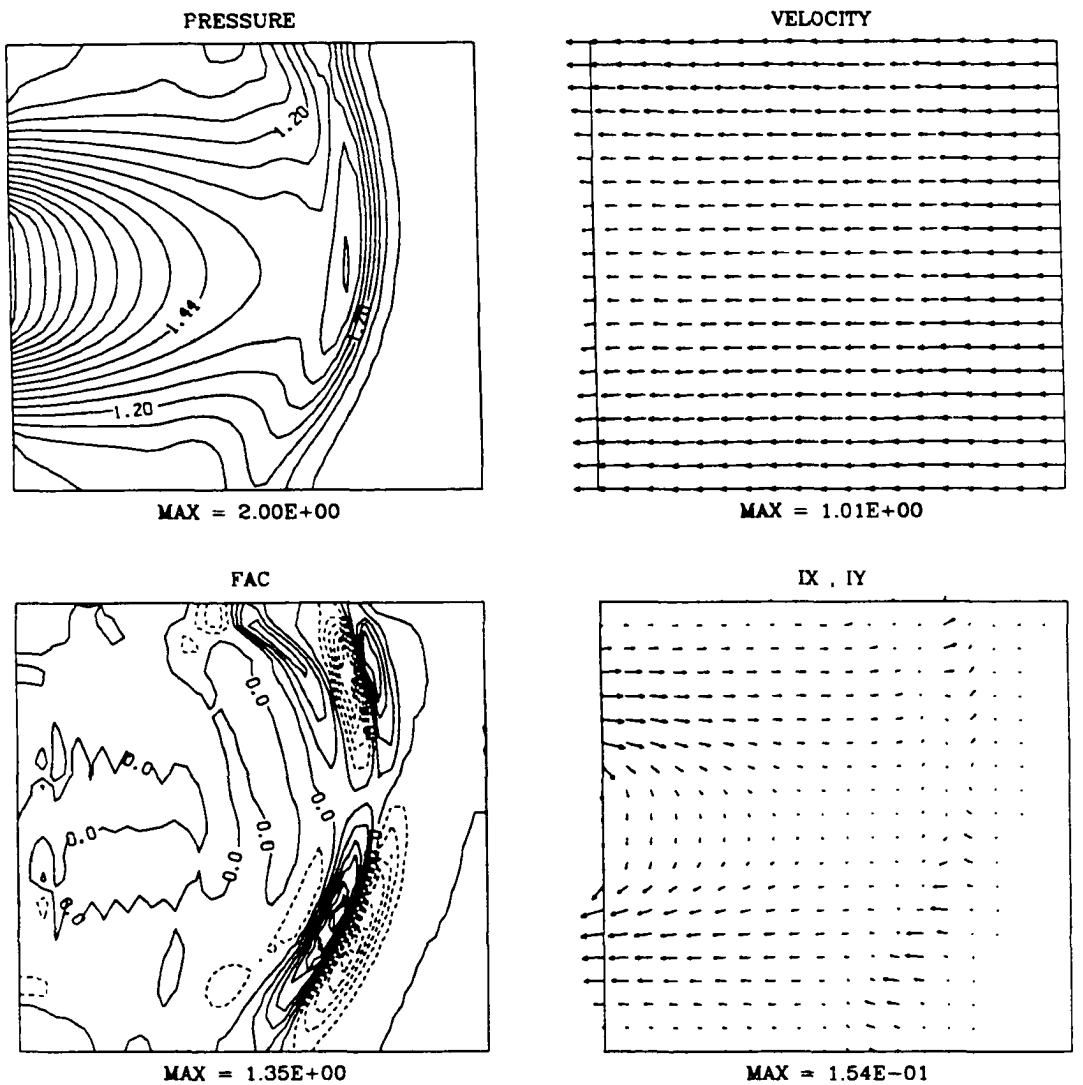

Figure 6–12 (b) 500 time steps ($\tau = 2.06$)

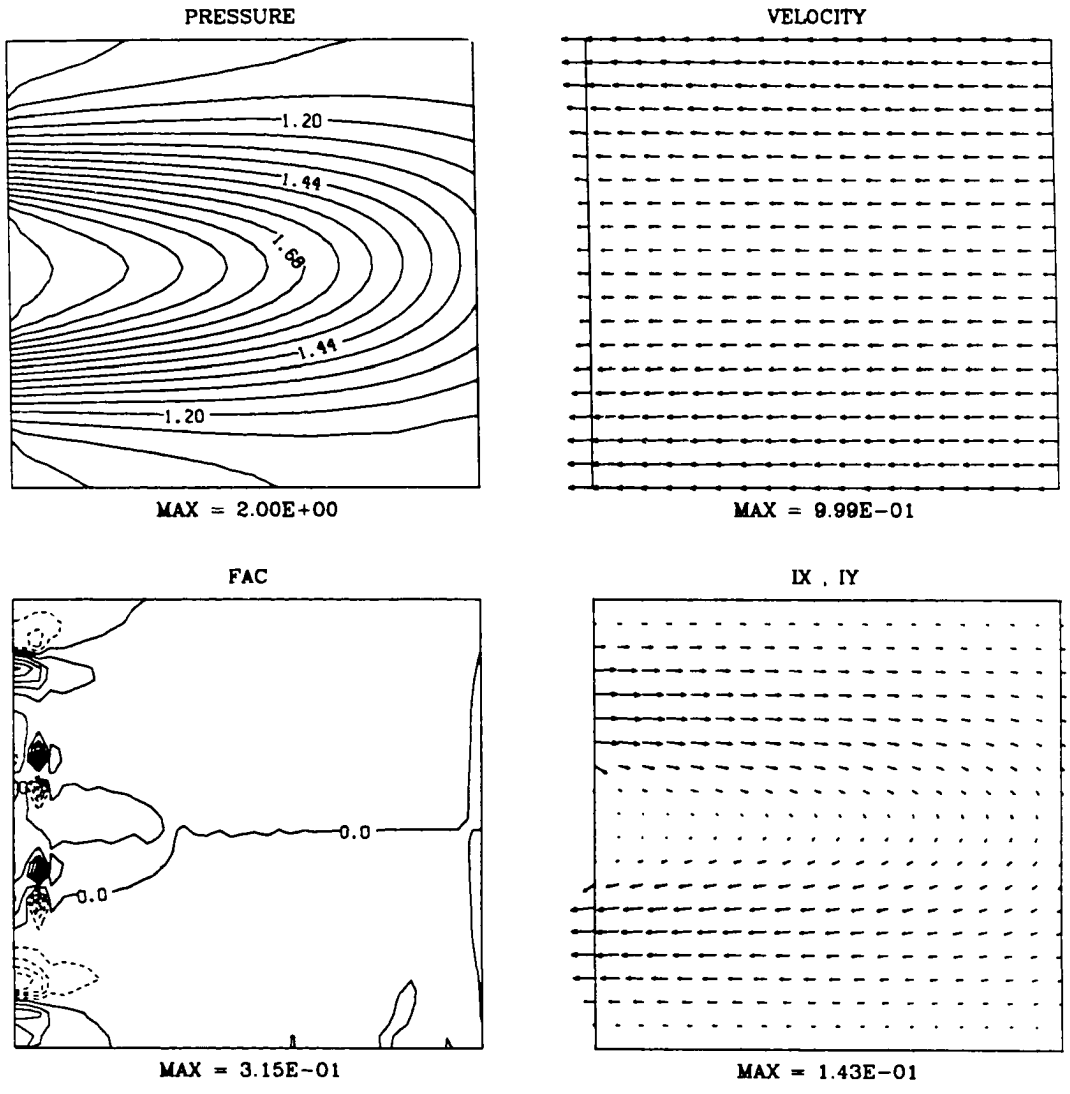

Figure 6–12 (c) 1500 time steps ($\tau = 6.13$)

clearly, the wave structure can be recognized very clearly at 200 time steps. If we increase ξ_x/ξ_y to 5.0, the numerical instability appears as early as 250 time steps ($\tau = 1.03$). Therefore, we do not show this case here.

6–4. Region 1 Field-Aligned Current Generation

Figure 6–13 shows the field-aligned current generation mechanism from the wave. If the wave is one dimensional, there is no field-aligned current as is shown in section 4–2–2. However, it is not a plane wave. In this case, the vorticity changes across the wave as shown in Figure 6–13. The ionospheric dissipation causes the change of the vorticity. Thus, the field-aligned current is generated. The vorticity is related to the divergence of the electric field. Through the wave, the kinetic energy of the convection is converted to electromagnetic energy; i.e., the current flows as a result of a dynamo mechanism. In fact, the plasma sheet current flows in the opposite direction to the convection electric field. Therefore, the direction of the field-aligned current is of the region 1 field-aligned current.

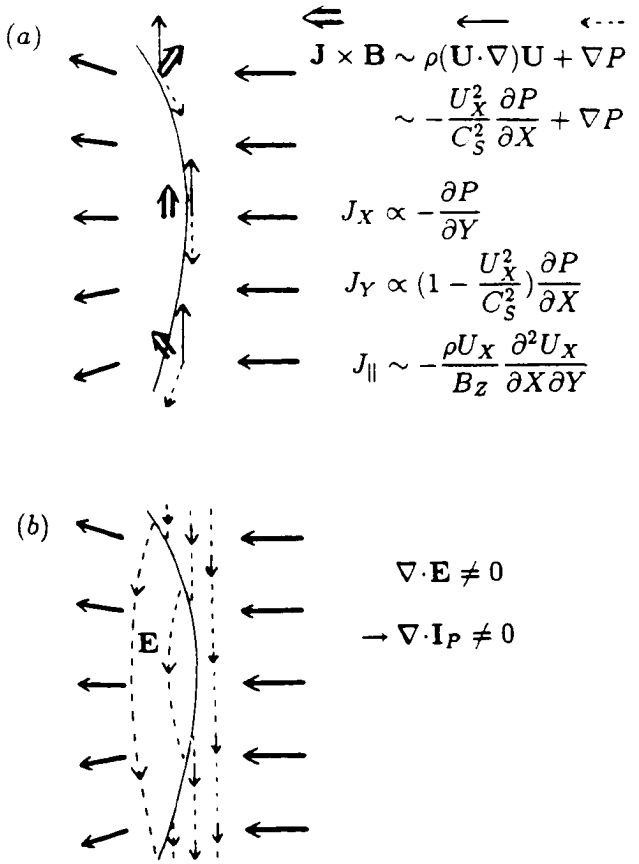

Figure 6–13. Field-aligned current generation from the plasma sheet. The field-aligned current is generated from the MHD fast mode wave. (a) Because of the curvature of the wave front, the magnetospheric current has a divergence. It is related to the change of the vorticity. Even though the inflow convection does not have vorticity, the vorticity is generated in the flow because of the ionospheric dissipation. (b) The convection velocity, and hence, the convection electric field, decrease through the wave. Since the wave has curvature, the electric field diverges. Mapping to the ionosphere, the electric field causes the divergence of the Pedersen current also. Both (a) and (b) explain the field-aligned current generation consistently.

The generation of the large-scale field-aligned currents due to plasma sheet dynamics has been studied. We first formulated the two-layer model, which is composed of a height-integrated plasma sheet, a height-integrated ionosphere, and a massless magnetosphere between them. The Alfvén wave transition time is zero in the massless magnetosphere. We may still height integrate the plasma sheet even though the geomagnetic field bends if we assume some symmetry. We introduced the reaction force of the ionospheric $\mathbf{J} \times \mathbf{B}$ force to the plasma sheet dynamics. We call it the ionospheric 'drag force'. This force is included in the magnetospheric $\mathbf{J} \times \mathbf{B}$ force. We obtained the basic equations in the plasma sheet. The ionospheric quantities and the Ohm's law are mapped to the plasma sheet. The basic equations are essentially the same as the MHD equations, while the induction equation of the MHD is replaced by the ionospheric Ohm's law.

Next, we studied the evolution of initial small perturbations in terms of linear analyses. We introduced the quantities

$$D = \nabla_{x,y} \cdot (B_z \delta \mathbf{V}_{x,y}) \tag{4 \cdot 21}$$

$$R = \nabla_{x,y} \cdot (B_z \delta \mathbf{V}_{x,y} \times \hat{z}) \tag{4 \cdot 22}$$

The $D \neq 0$ and $R \neq 0$ modes correspond to the MHD fast mode and the Alfvén mode waves (or field-aligned currents), respectively. The behavior of the D mode

and the R mode is slightly different from the ordinary MHD waves. In the uniform and static background plasma, the R mode decays with a time constant $\tau_1 = m/(\Sigma_P B_z^2)$ where m is the height-integrated mass density in the plasma sheet and Σ_P is the height-integrated ionospheric Pedersen conductivity mapped to the plasma sheet. The R mode does not propagate on the height-integrated plasma sheet, to which the geomagnetic field is perpendicular. Instead, it is transmitted back and forth between the plasma sheet and the ionosphere with zero transition time, and the ionospheric Joule dissipation causes the decay of this mode. The coupling with the ionosphere introduces substantial effect of the finite conductivity into the ordinary MHD.

If the background plasma has a pressure gradient, the Alfvén mode and the fast mode are coupled through the ionospheric 'drag' force. Thus, the fast mode wave is accompanied by the field-aligned current. This wave, if it propagates perpendicular to the zero-order pressure gradient, obeys $(\partial^2/\partial t^2 - C_S^2 \partial^2/\partial y^2)D = \alpha \partial D/\partial y)$, where C_S is the sound speed. The α term comes from the ionospheric 'drag' force due to the ionospheric Hall current. The ionospheric Hall current is caused by the secondary convection generated by $\mathbf{I} \times \delta \mathbf{B}_z$ where $\mathbf{I}$ is the magnetospheric zero-order current. The wave is amplified either in the $+y$ or the $-y$ direction depending on the sign of α, which contributes to the dawn-dusk asymmetry of the field-aligned current distribution.

We also numerically simulated the plasma sheet dynamics and the field-aligned current generation during the poleward expansion of auroral substorms. We considered a situation in which an enhanced magnetospheric convection hits the inner edge of the plasma sheet and increases the pressure there. The results are summarized as follows and in Table 7–1.

1. A finite amplitude MHD fast mode wave begins to propagate upstream across the geomagnetic field as illustrated in Figure 7–1. This wave might correspond to the poleward expansion of the aurora substorm. Since it is a finite amplitude wave, the propagation speed with respect to the enhanced convection is slightly faster than the local sound speed. The wave is accompanied by two pairs of intense field-aligned currents as indicated in the figure.

2. The first pair of field-aligned currents on the front side of the wave flows out of the plasma sheet on the dawn side and flows into the plasma sheet on the dusk side. The flow directions are the same as those of the region 1 field-aligned current. The field-aligned currents are connected to the dusk to dawn current, which is generated by the dynamo mechanism (deceleration of the flow) of the wave.

3. The second pair of field-aligned currents on the back side of the wave flows in the opposite direction to the first pair; i.e., the flow directions are the same as those of the region 2 field-aligned current. It is connected to another plasma

Table 7–1 Numerical Results

Figure	Time	M_a^2	M_s^2	β	γ	η	Σ_H^*	ξ_x/ξ_y	J_z	wake
Default	$>6\tau$	0.2	0.5	0.8	1.0	1.0	+0.5	1.0		
6–1	–	–	–	–	–	–	–	–	E.E+	E
6–2	2τ	0.4	1.0	–	–	–	–	–	S.S++	E
6–3	–	0.1	0.25	–	–	–	–	–	–	–
6–4	–	0.4	–	1.6	–	–	–	–	S.E+	W
6–5	1τ	0.1	–	0.4	–	–	–	–	E.E	S
6–6	–	–	0.25	1.6	–	–	–	–	–	–
6–7	–	–	–	–	2.0	–	–	–	W	–
6–8	1τ	–	–	–	–	0.2	–	–	E.W	S
6–9	–	–	–	–	–	5.0	–	–	E.E+	W
6–10	–	–	–	–	–	–	0	–	E.E+	E
6–11	–	–	–	–	–	–	–	2.0	E.E	S
6–12	–	–	–	–	–	–	–	0.5	E.E++	W

S: strong, E: exist, W: weak or not recognized
S.W: first pair is strong, second pair is weak
+: well steepened

Table 7–1. Numerical results

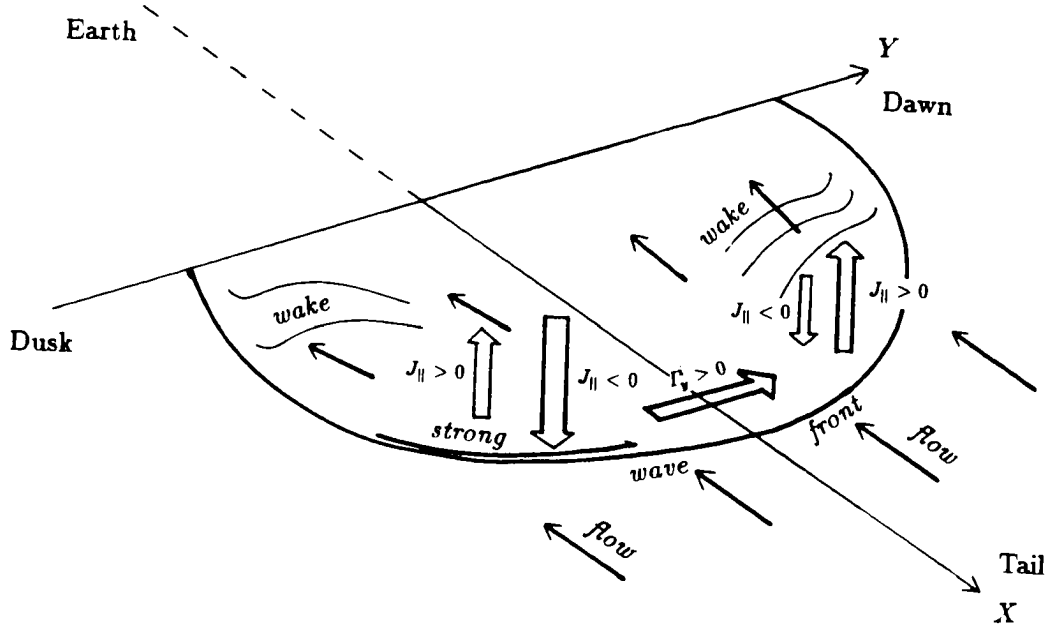

Figure 7–1. Summary of the numerical results. The MHD fast mode wave propagates tailward. This wave might correspond to the poleward expansion of the auroral substorm. The wave carries a dusk to dawn current due to the dynamo mechanism. It is connected to the region 1 field-aligned currents in both the dawn side and the dusk side. The wave is more steepened in the premidnight sector, which is also consistent with observations. In some cases, a wake-like structure appears. If it is actual (i.e., not numerical noise), it might explain the complicated field-aligned current distribution in the midnight sector during substorms.

sheet current which flows along the wave normal, i.e., in the earth-tail direction. Divergence of this current produces both pairs of the field-aligned currents as shown in the figure. In other words, the first pair of the field-aligned currents (region 1 sense) comes from both currents (dawn-dusk and earth-tail directions) on the plasma sheet, and hence, it is stronger than the second pair. Note that we excluded the inner edge of the plasma sheet where the main part of the region 2 field-aligned currents are believed to originate [*Wolf and Spiro*, 1985].

4. The wave propagation speed, and hence, the degree of the steepening are asymmetric between the dawn side and the dusk side. The wave propagates faster on the dawn side, and it expands more dawnward than duskward. On the other hand, the wave is more steepened on the dusk side, and the field-aligned current intensity is greater on the dusk side. The asymmetry comes from the ionospheric 'drag' force due to the ionospheric Hall current.

5. The wave has a wake-like structure for some cases; e.g., for larger B_z, for smaller γ, and for larger Σ_P cases. This wake-like structure, however, could be artificial caused by numerical noise. If this structure is actual, it can explain complicated field-aligned current patterns in the midnight sector. This structure has the dawn–dusk asymmetry also.

6. If the convection velocity (in terms of the sound speed) is large, the wave is more intensified and the wave propagation speed is slower. In this case, we have

a fine structure of the field-aligned current system. If the convection is slower, the wave is not well steepened. After the wave propagates out of the upstream boundary, a quasi-steady state is achieved without any outstanding field-aligned current systems. We obtain very similar asymptotic states even if we change the ionospheric Hall conductivity.

7. If the convection is very slow, we do not have a propagating wave, and the field-aligned currents do not exist.

8. A high γ (adiabatic case) causes a high pressure, and hence, a substantially slower convection. In this case, the wake-like structure (or numerical noise) is more faint, and the wave propagation is faster.

9. The ionospheric Pedersen conductivity introduces dissipation into the plasma sheet. If the conductivity is large (low η), the wave propagates faster, and hence, there is less steepening. If it is small, on the other hand, the wake-like structure is less obvious while the wave is well steepened. The field-aligned current intensity (for the region 1 type) is not very sensitive to the ionospheric conductivity.

10. The tailward stretch of the geomagnetic field contributes more steepening of the wave with less wake-like structure. The field-aligned current is slightly more intense in this case.

As we have summarized above, the poleward expansion during the substorm can be understood as the tailward propagation of the finite amplitude MHD fast mode

(D mode) wave. The region 1 field-aligned current is generated from that wave. It is connected to the dusk to dawn plasma sheet current which is generated by the dynamo mechanism of the wave. The location of this field-aligned current with respect to the poleward expansion agrees with observation. Once a small fraction of the field-aligned current is separated from the wave, it might be convected downstream as a decaying R mode. This earthward motion might account for the individual aurora arc's equatorward motion during the substorm. Because of the 'drag' force due to the ionospheric Hall current, the wave is not symmetric with respect to the noon-midnight meridian. Thus, the field-aligned currents associated with the wave are stronger on the dusk (premidnight) side. This asymmetry also matches with the observation of the westward travelling surge on the region 1 field-aligned current system.

When the basic equations were formulated, many assumptions were employed for the large-scale M–I coupling system. The model now quantitatively explains several phenomena simultaneously. That partly provides the rationale of the present model, and hence, the present assumptions.

References Cited

Akasofu, S.-I., The dynamical morphology of the aurora polaris, *Annals of the International Geophysical Year*, *20*, 311–364, Pergamon, 1962.

Akasofu, S.-I., The development of the auroral substorm, *Planet. Space Sci.*, *12*, 273, 1964.

Akasofu, S.-I., D. S. Kimball, and C.-I. Meng, The dynamics of the aurora, 2, Westward traveling surges, *J. Atmos. Terr. Phys.*, *27*, 173, 1965.

Akasofu, S.-I., A study of auroral displays photographed from the DMSP-2 satellite and from the Alaska meridian chain of stations, *Space Sci. Rev.*, 16, 617–725, 1974.

Akasofu, S.-I., Recent progress in studies of DMSP auroral photograph, *Space Sci. Rev.*, 19, 169–215, 1976.

Akasofu, S.-I., Physics of magnetospheric substorms, *Astrophysics and space science library, vol. 47*, Reidel, 1977.

Akasofu, S.-I., Y. Kamide, J. R. Kan, L. C. Lee, and B.-H. Ahn, Power transmission from the solar wind-magnetosphere dynamo to the magnetosphere and to the ionosphere: analysis of the IMS Alaska meridian chain data, *Planet. Space Sci.*, *29*, 721–730, 1981.

Alfven, H. and C. G. Falthammar, Cosmical Electrodynamics, *Fundamental Principles*, Clarendon, Oxford, 1963.

Axford, W. I., and C. O. Hines, A unifying theory of high-latitude geophysical phenomena and geomagnetic storms, *Can. J. Phys., 39*, 1422, 1961.

Birn, J., and K. Schindler, Self-consistent theory of three-dimensional convection in the geomagnetic tail, *J. Geophys. Res., 88*, 6969–6980, 1983.

Boisvert, R., A fourth order accurate fast direct method for the Helmholtz equation, in *Elliptic Problem Solvers 2*, edited by G. Birkhoff and A. Schoenstadt, pp. 35–44., Academic Press, Orlando, Florida, 1984.

Bostrom, R., Mechanisms for driving Birkeland currents, in *Physics of the Hot Plasma in the Magnetosphere*, edited by B. Hultqvist and Lennart Stenflo, pp. 341–362, Plenum, New York, 1975.

Brekke, A., J. R. Doupnik, and P. M. Banks, Incoherent scatter measurements of *E* region conductivities and currents in the auroral zone, *J. Geophys. Res., 79*, 3773–3790, 1974.

Coleman, P. J., Jr., and R. L. McPherron, Substorm observation of magnetic perturbations and ULF waves at synchronous orbit by ATS-1 and ATS-6, in *The Scientific Satellite Programme During the International Magnetospheric Study*, edited by K. Knott and B. Battrick, pp. 345, D. Reidel, Hingham, Mass., 1976.

Elphic, R. C., P. A., Mutch, and C. T. Russell, Observations of field-aligned currents at the plasma sheet boundary: An ISEE-1 and 2 survey, *Geophys. Res. Lett., 12*, 631, 1985.

Fairfield, D. H., Magnetic field signatures of substorms on high-latitude field lines in the nighttime magnetosphere, *J. Geophys. Res., 78*, 1553, 1973.

Frank, L. A., R. L. McPherron, R. J. DeCoster, B. G. Burek, K. L. Ackerson, and C. T. Russell, Field-aligned currents in the Earth's magnetotail, *J. Geophys. Res., 86*, 687, 1981.

Frank, L. A., Plasmas in the earth's magnetosphere, *Space Sci. Rev., 42*, 211, 1985.

Fridman, M., and J. Lemaire, Relationship between auroral electron fluxes and field-aligned electric potential difference, *J. Geophys. Res., 85*, 664, 1980.

Harel, M., R. A. Wolf, P. H. Reiff, R. W. Spiro, W. J., Burke, F. J. Rich, and M. Smiddy, Quantitative Simulation of a magnetospheric substorm 1. Model logic and overview, *J. Geophys. Res., 86*, 2217–2241, 1981.

Hasegawa, A., and T. Sato, Generation of field-aligned currents during substorm, in *Dynamics of the Magnetosphere*, edited by S.-I. Akasofu, pp. 529-542, D. Reidel, Hingham, Mass., 1980.

Hones. E. W. Jr., A. T. Y. Lui, S. J. Bame, and S. Singer, Prolonged tailward flow of plasma in the thinned plasma sheet observed at r $\sim$ 18 R_E during substorms, *J. Geophys. Res., 79*, 1385, 1974.

Hones, E. W. Jr., J. Birn, S. J. Bame, and C. T. Russell, New observations of plasma vortices and insights into their interpretation, *Geophys. Res. Lett., 10*,

674-677, 1983.

Huang, C. Y., Quadrennial review of the magnetotail, *Rev. Geophys., 25*, 529–540, 1987.

Iijima, T., and T. A. Potemra, The amplitude distribution of field-aligned currents at northern high latitudes observed by Triad, *J. Geophys. Res., 81*, 2165, 1976.

Jackson, J. D., *Classical electrodynamics*, second ed., J. Wiley, New York, 1975.

Jaggi, R. K., and R. A. Wolf, Self-consistent calculation of the motion of a sheet of ions in the magnetosphere, *J. Geophys. Res., 78*, 2852–2866, 1973.

Kamide, Y., and S.-I. Akasofu, The auroral electrojet and global auroral features, *J. Geophys. Res., 80*, 3585, 1975.

Kamide, Y., J. D. Craven, L. A. Frank, B.-H. Ahn, and S.-I. Akasofu, Modeling substorm current systems using conductivity distributions inferred from DE auroral images, *J. Geophys. Res., 91*, 11235–11256, 1986.

Kan, J. R., and Y. Kamide, Electrodynamics of the westward traveling surge, *J. Geophys. Res., 90*, 7615, 1985.

Kan, J. R., and W. Sun, Simulation of the westward traveling surge and Pi 2 pulsations during substorms, *J. Geophys. Res., 90*, 10911–10922, 1985.

Kan, J. R., Generation of field-aligned current in magnetosphere-ionosphere coupling in a MHD plasma, *Planet. Space Sci., 35*, 903-912, 1987.

Kan, J. R., L. Zhu, and S.-I. Akasofu, A theory of substorms: onset and subsidence, *J. Geophys. Res., 93*, 5624–5640, 1988.

Knight, S., Parallel electric fields, *Planet. Space Sci., 21*, 741, 1973.

Leith, C. E., Numerical simulation of the earth's atmosphere, *Methods in computational phys.*, 4, 1–28, 1965.

Lotko, W., B. U. O. Sonnerup, and R. L. Lysak, Nonsteady boundary layer flow including ionospheric drag and parallel electric fields, *J. Geophys. Res., 92*, 8635–8648, 1987.

MacCormack, R. W., The effect of viscosity in hypervelocity impact cratering, AIAA paper No. 69–354, 1969.

Miura, A., and T. Sato, Numerical simulation of global formation of auroral arcs, *J. Geophys. Res., 85*, 73–91, 1980.

Miura, A., Anomalous transport by Kelvin-Helmholts instabilities, in *Computer Simulation of Space Plasma*, edited by H. Matsumoto and T. Sato, pp. 203–224, D. Reidel, Hingham, Mass., 1985.

Nagai, T., Field-aligned currents associated with substorms in the vicinity of synchronous orbit 2. GOES 2 and GOES 3 observations, *J. Geophys. Res., 92*, 2432–2446, 1987.

Nicholson, D. R., *Introduction to plasma theory*, John Wiley, New York, 1983.

Ogino, T., A three-dimensional MHD simulation of the interaction of the solar wind with the earth's magnetosphere: The generation of field-aligned currents, *J. Geophys. Res., 91*, 6791, 1986.

Ohtani, S., S. Kokubun, R. C. Elphic, and C. T. Russell, Field-aligned current signatures in the near-tail region 1. ISEE observations in the plasma sheet boundary layer, *J. Geophys. Res., 93*, 9709–9720, 1988.

Opgenoorth, H. J., R. J. Pellinen, W. Baumjohann, E. Neilsen, G. Marklund, and L. Eliasson, The three dimensional current flow and particle precipitation in a westward traveling surge (observed during the Barium-GEOS rocket experiment), *J. Geophys. Res., 88*, 5505, 1983.

Parks, G. K., C. S. Lin, K. A. Anderson, R. P. Lin, and H. Reme, ISEE 1 and 2 particle observation of outer plasma sheet boundary, *J. Geophys. Res., 84*, 6471–6476, 1979.

Parks, G. K., M. McCarthy, R. J. Fitzenreiter, J. Etcheto, K. A. Anderson, T. E. Eastman, L. A. Frank, D. A. Gurnett, C. Huang, R. P. Lin, A. T. Y. Lui, K. W. Ogilvie, A. Pedersen, H. Reme, and D. J. Williams, Particle and field characteristics of the high-latitude plasma sheet boundary layer, *J. Geophys. Res., 89*, 8885, 1984.

Rostoker, G., The polarization characteristic of Pi 2 micropulsations and their relation to the determination of possible source mechanisms for the production

of nighttime impulsive micropulsation activity, *Can. J. Phys., 45*, 1319, 1967.

Rostoker, G., and R. Bostrom, A mechanism for driving the gross Birkeland current configuration in the auroral oval, *J. Geophys. Res., 81*, 235–244, 1976.

Rostoker, G., and E. T. Eastman, A boundary layer model for magnetosheric substorms, *J. Geophys. Res., 92*, 12187, 1987.

Sato, T., A theory of quiet auroral arcs, *J. geophys. Res., 83*, 1042-1048, 1978.

Sato, T., and T. Iijima, Primary sources of large-scale Birkeland current, *Space Sci. Rev., 24*, 347–366, 1979.

Sonnerup, B. U. O., Theory of the low-latitude boundary layer, *J. Geophys. Res., 85*, 2017–2026, 1980.

Southwood, D. J., and W. F. Stuart, Pulsations at the substorm onset in *Dynamics of the magnetosphere*, edited by S.-I. Akasofu, D. Reidel, Hingham, Mass., 1980.

Sugiura, M., and T. A. Potemra, Net field-aligned currents observed by Triad, *J. Geophys. Res., 81*, 2155–2164, 1976.

Vasyliunas, V. M., Mathematical models of magnetospheric convection and its coupling to the ionosphere, in *Particles and Fields in the Magnetosphere*, edited by B. McCormac, pp. 60, D. Reidel, Hingham, Mass, 1970.

Vasyliunas, V. M., The interrelationship of magnetospheric processes, in *Earth's Magnetospheric Processes*, edited by B. McCormac, pp. 29, D. Reidel, Hingham, Mass, 1972.

Vasyliunas, V. M., Fundamentals of current description, in *Magnetospheric Currents*, edited by T. A. Potemra, pp. 63–66, Geophys. Monograph 28, AGU, Washington, DC, 1984.

Watanabe, K., M. Ashour-Abdalla, and T. Sato, A numerical model of magnetosphere ionosphere coupling: preliminary results, *J. Geophys. Res., 91*, 6973–6978, 1986.

Watanabe, K., and T. Sato, Self-excitation of auroral arcs in a three-dimensionally coupled magnetosphere ionosphere system, *Geophys. Res. Lett., 7*, 717–720, 1988.

Walker, R. J., and T. Ogino, Field-aligned current and magnetospheric convection: A comparison between MHD simulations and observations, *PPG-1043*, Center for Plasma Physics and Fusion Engineering, University of CA., Los Angeles, 1987.

Wolf, R. A., and R. W. Spiro, Particle behavior in the magnetosphere, in *Computer Simulation of Space Plasma*, edited by H. Matsumoto and T. Sato, pp. 227–254, D. Reidel, Hingham, Mass., 1985.

Zmuda, A. J., and J. C. Armstrong, The diurnal flow pattern of field-aligned currents, *J. Geophys. Res., 79*, 4611–4619, 1974.